DISSERTATION

LOW RESISTANCE VISIBLE WAVELENGTH DISTRIBUTED BRAGG REFLECTORS

Submitted by

Joel Mark Fastenau

Department of Electrical and Computer Engineering

In partial fulfillment of the requirements

for the Degree of Doctor of Philosophy

Colorado State University

Ft. Collins, Colorado

Spring 1999

COLORADO STATE UNIVERSITY

February 9, 1999

WE HEREBY RECOMMEND THAT THE DISSERTATION PREPARED UNDER OUR SUPERVISION BY JOEL MARK FASTENAU ENTITLED LOW RESISTANCE VISIBLE WAVELENGTH DISTRIBUTED BRAGG REFLECTORS BE ACCEPTED AS FULFILLING IN PART REQUIREMENTS FOR THE DEGREE OF DOCTOR OF PHILOSOPHY.

Committee on Graduate Work

Adviser

Department Head

ABSTRACT OF DISSERTATION

LOW RESISTANCE VISIBLE WAVELENGTH

DISTRIBUTED BRAGG REFLECTORS

This dissertation reports the first application of semiconductor heterojunctions with naturally occurring small energy band offsets to distributed Bragg reflector (DBR) structures for the purpose of lowering their series resistance. Selecting DBR layer pairs with small valence or conduction band offsets eliminates the need for complicated structural grading schemes typically used to smooth out the interface energy barriers, and thus achieves low resistance DBRs using simple stacks of quarter wavelength thick layers. Low resistance, highly reflective DBRs are used in vertical cavity surface emitting lasers, which are attractive light sources for many visible wavelength applications. The target wavelength for this work is 650 nm.

From theoretical band offset calculations using the Van de Walle model solid theory, heterojunctions of mixed arsenide and phosphide III-V semiconductor single crystal alloys were selected for the low band offset DBRs: $Al_{0.90}Ga_{0.10}As/Al_{0.14}Ga_{0.38}In_{0.48}P$ for p-type and $AlAs/Al_{0.10}Ga_{0.42}In_{0.48}P$ for n-type. Theoretical specific contact resistance calculations showed that the low offset structures have smaller resistances than AlInP/AlGaInP DBRs which previously have been investigated for visible VCSELs.

The epitaxial films for this work were grown on GaAs substrates by gas source molecular beam epitaxy. Bulk AlGaAs and AlGaInP layers were grown to qualify their structural and electrical characteristics, and this knowledge was applied to grow the DBR samples. Double crystal x-ray diffraction measurements showed the DBRs were high quality, single crystal structures. Reflectance measurements on 40 period DBRs determined each had a peak of 99% at locations within 4% of the target wavelength.

The low band offset DBRs were processed and their specific contact resistances determined using the transmission line model. The measured values of $2.75\times10^{-4}\ \Omega\cdot cm^2$ for the p-type DBR and $2.58\times10^{-5}\ \Omega\cdot cm^2$ for the n-type DBR were within experimental uncertainty of their theoretical values. These results compare very favorably with numbers reported in the literature for AlGaAs DBRs that employ complicated structural grading schemes. On a per period basis, the low valence band offset p-type DBR resistance is comparable to or lower than previous reports, while the low conduction band offset n-type DBR is an order of magnitude lower than the best previously reported result.

Joel Mark Fastenau
Electrical and Computer Engineering Department
Colorado State University
Ft. Collins, CO 80523
Spring 1999

ACKNOWLEDGMENTS

The successful completion of this research project was not the accomplishment of one person alone, but rather was achieved with the help and guidance of many people, from the faculty and staff of the Electrical and Computer Engineering Department to my fellow graduate students, friends, and family. All of those people deserve a special thank you for the support they provided.

At the top of the list within the department is my advisor, Dr. Gary Robinson, whose support allowed me to attend graduate school at Colorado State University. I thank him for the resources he provided which made this work possible. His guidance and patience were very much appreciated. I want to thank my graduate committee members, Dr. Derek Lile, Dr. Carmen Menoni, and Dr. Robert Leisure, for their time and assistance with my project. I would also like to thank the rest of the faculty, especially Dr. Carl Wilmsen and Dr. John Mahan, who have contributed to this work through the use of their equipment and through their instruction and advice. Special thanks go to the staff in the department office, past and present, for all of their assistance and advice in dealing with the omnipresent bureaucracy of the university as well as other problems.

No graduate student would be able to survive and graduate without the help and support of those who share in the rights and privileges granted to that position. Thank you

to Gary Patrizi and Dr. Prabhu Thiagarajan for instructing me in the ways of MBE and for maintaining the system and laboratory. Thanks to Dr. Tim Vogt and Larry Woods for their expertise and advice, and for teaching me how to use the various characterization equipment. Also, thanks go to Dr. Stu Feld and Daryl Pulver for training in the use of and maintaining the equipment in the cleanroom. I very much appreciate the help and friendship of all of the above people, as well as of everyone else with whom I have shared my time at CSU.

Very special mention must go to my parents and family, and especially to my wife, Jean. They were always there for me, no matter what the circumstances, and this project could not have been completed without their support and help. I deeply appreciate and reciprocate the love and encouragement they have always shown to me.

TABLE OF CONTENTS

CHAPTER I

INTRODUCTION

In recent years there has been a push in optoelectronic devices toward the visible wavelengths. Semiconductor lasers in this wavelength region, 400 to 800 nm, have applications in optical displays, data storage, scanners and printers, and optical interconnects using plastic fibers. The desire to move into these wavelengths for displays and optical sources is obviously due to the necessary interaction with the device users. In optical data storage and retrieval, the shorter wavelengths mean smaller spot sizes and thus larger storage densities. Optical communication using plastic fibers provides a lower cost alternative to glass fibers in short haul, rugged environment applications such as aerospace, automotive, and local area computer networks.

Edge emitting red AlGaInP semiconductor lasers have taken the lead in providing reliable, high performance devices for the above visible wavelength applications, mainly due to the maturity of the edge emitting design and the transfer of structural enhancement concepts from longer wavelength AlGaAs devices [1]. The vertical cavity surface emitting laser (VCSEL) is a much younger technology, especially in the visible wavelengths, but the structure boasts several advantages over its edge emitting counterpart [2]. The advantages come from the main structural difference in a VCSEL: having the light emitted normal to the

surface of the device. This gives the ability to obtain symmetrical beam cross sections with small divergence and to do on-wafer laser testing before any costly post-growth fabrication and packaging. It also means a relative ease of fabrication into two dimensional arrays and integration with other optoelectronic devices. In addition, the short laser cavity length results in lower thresholds and single longitudinal mode operation.

So, taking the plastic optical fiber communication application as an example, the visible VCSEL is an attractive device to use as an active light source. The beam shape can be lithographically defined to match the circular cross section of the fiber, making the coupling of light into the fiber easier and less expensive than with the elliptical output of an edge emitting device. Using the same AlGaInP semiconductor alloys, the wavelength of the optical beam can be tailored to the 650 nm attenuation minimum of polymethylmethacrylate (PMMA), the most commonly used type of plastic optical fiber [3]. The array processing potential of the VCSEL should enable high volume and low cost manufacturing.

One downside to the VCSEL structure is that the small length of the active region means the resonator mirrors must be very highly reflective. The most commonly applied solution is the use of semiconductor distributed Bragg reflectors (DBRs), which consist of alternating layers of high and low index of refraction semiconductor alloys, each with thicknesses equal to one quarter of the wavelength of the targeted optical output. The DBR structure obtains a high reflectance due to the constructive interference of the reflections from each interface. The design goal of the two DBR material layers is to maximize their index difference while both remain transparent to the output of the laser. In order to obtain high enough total reflection, twenty or more DBR periods are required. This means the

thickness of the VCSEL is dominated by the two DBRs, each of which can be several micrometers high.

One consequence of the thick DBR structures is their high series resistance, which is one of the biggest limitations on VCSEL device performance. The high resistance increases laser thresholds and increases thermal heating which lowers output power. Much of the DBR resistance is due to the large energy band offsets at the heterojunctions between the individual semiconductor material layers. The large band offsets form barriers to carrier transport, requiring a larger applied bias voltage to achieve a given current. Many different schemes have been employed to reduce these barriers and lower DBR resistances [4-8]. Most of the schemes involve grading the alloy composition and/or modulating the carrier doping profile in the regions near the interfaces between DBR layers. These schemes have been successful in lowering the contact resistance of DBRs by several orders of magnitude, thus making practical devices attainable. However, the cost is the increased complexity of the DBR design and growth, including the need for highly accurate control of the thicknesses and of the changing alloy compositions during epitaxial growth.

One method of lowering the DBR series resistance which has not been investigated is the selection of semiconductor DBR material pairs with naturally occurring small energy band offsets. This would eliminate the need for complex alloy composition grading schemes at the DBR interfaces, since the band offsets would be inherently small. Thus the design and growth of the DBR structures would be simplified. The naturally low band offsets would also allow the overall doping level in the DBRs to be lowered. DBRs are typically doped in the low to mid 10^{18} cm^{-3} range. The purpose of this high doping is to lower the DBR

resistance by increasing the tunneling current through the energy barriers at the layer interfaces. Unfortunately the high carrier concentrations also increase free carrier optical absorption due to impurities, thus increasing the threshold gain of a VCSEL. So the ability to lower the overall doping levels through the use of DBRs with inherently low band offsets would assist in lowering the threshold currents of a VCSEL.

The objective of this research project is to use semiconductor material pairs with naturally occurring small energy band offsets in DBR structures in order to lower the series resistance of the DBRs. This is possible by selecting appropriate material pairs from among the various III-V semiconducting arsenide and phosphide alloys available for growth via gas source molecular beam epitaxy (GSMBE). In order to achieve both small valence band offsets for p-type DBRs and small conduction band offsets for n-type DBRs, different but compatible material pairs are necessary. This dissertation reports the successful realization of the project objective, from the selection of the appropriate material pairs, to the growth and characterization of the low resistance, small energy band offset DBR structures.

Chapters II and III of this dissertation provide a general background on topics relevant to this project and describe theoretical calculations, respectively. Chapter II covers the fundamental structure and operation of both VCSELs and DBRs. Special attention is given to the requirements of the DBRs, from the high reflectance to the low resistance. This includes examining various techniques used to lower the series resistance in the DBR structures. The theoretical studies in Chapter III present energy band offset and DBR resistance calculations. The Van de Walle model solid theory [9] is used to determine the theoretical valence and conduction band offsets for the various III-V semiconductors

available for growth. This provides a basis for selecting suitable material pairs. The choices for the low band offset DBRs are $Al_{0.90}Ga_{0.10}As/Al_{0.14}Ga_{0.38}In_{0.48}P$ for p-type and $AlAs/Al_{0.10}Ga_{0.42}In_{0.48}P$ for n-type. In addition, large band offset material pairs were selected to serve as a comparison with the low offset DBRs. These control samples, which should have a larger DBR stack resistance due to their larger band offsets, are $Al_{0.44}Ga_{0.08}In_{0.48}P/Al_{0.14}Ga_{0.38}In_{0.48}P$ and $Al_{0.52}In_{0.48}P/Al_{0.10}Ga_{0.42}In_{0.48}P$ for p-type and n-type, respectively. The second half of the chapter determines the theoretical specific contact resistance for each of the four DBR structures under study. It shows that the effect of the interface barriers dominates the resistance, and that the low band offset material pairs result in DBRs with lower theoretical resistances than their larger band offset control samples.

Chapter IV describes the experimental equipment and procedures used in this work. Discussions of epitaxial growth via GSMBE include MBE fundamentals, system specifications, and growth procedures. The quality of the epitaxial films is characterized by double crystal x-ray diffraction, Hall-van der Pauw, and reflectance measurements. System setup and measurement procedures are covered for all three techniques. Finally, transmission line model (TLM) measurements determine the specific contact resistances. TLM discussions include theory, test structure fabrication, and resistance measurements.

The results of the experiments are discussed in Chapter V. The first sections qualify the growth and doping characteristics of the AlGaAs and AlGaInP semiconductors used in the DBRs through measurements on bulk epitaxial films for each alloy. Then the design and growth of the four DBR structures is described, and their structural quality is examined. The final section gives the specific contact resistance data from TLM measurements on all four

DBRs. Comparison with theoretical calculations shows that the low band offset DBRs perform as expected, while results for the larger band offset control samples do not. Possible structural problems with the control samples are investigated to explain the measured data.

Chapter VI summarizes the work done for this project and provides some conclusions. The measured specific contact resistance data compares favorably with DBR resistance data published in the literature. The low valence band offset resistance is in line with values for p-type AlGaAs DBRs which use complicated graded structures, while the low conduction band offset value is lower than that reported for n-type AlGaAs DBRs. Overall, the low band offset design provides an improved DBR structure for use in visible wavelength VCSELs.

REFERENCES: CHAPTER I

[1] J. Yoshida, K. Kishino, A. Kikuchi, and I. Nomura, "Continuous wave (CW) operation of GaInP-AlGaInP visible compressively strained multiple quantum wire (CS-MQWR) lasers," *IEEE J. Selected Topics in Quantum Elec.* **1**, 173 (1995).

[2] W. Chow, K. Choquette, M. Crawford, K. Lear, and G. Hadley, "Design, fabrication, and performance of infrared and visible vertical cavity surface emitting lasers," *IEEE J. Quantum Elec.* **33**, 1810 (1997).

[3] M. Kitazawa, ed., Plastic Optical Fibers Data Book; MRC Techno Research Inc.: Tokyo, Japan, 1993.

[4] E. Schubert, L. Tu, G. Zydzik, R. Kopf, A. Benvenuti, and M. Pinto, "Elimination of heterojunction band discontinuities by modulation doping," *Appl. Phys. Lett.* **60**, 466 (1992).

[5] R. Schneider, Jr. and J. Lott, "Cavity design for improved electrical injection in InAlGaP/AlGaAs visible (639-661 nm) vertical-cavity surface-emitting laser diodes," *Appl. Phys. Lett.* **63**, 917 (1993).

[6] M. Peters, B. Thibeault, D. Young, J. Scott, F. Peters, A. Gossard, and L. Coldren, "Band-gap engineered digital alloy interfaces for lower resistance vertical-cavity surface-emitting lasers," *Appl. Phys. Lett.* **63**, 3411 (1993).

[7] M. Hong, D. Vakhshoori, J. Mannaerts, and Y. Hsieh, "Low resistivity vertical-cavity surface emitting lasers grown by molecular-beam epitaxy using sinusoidal-composition grading in mirrors and *in situ* nonalloyed ohmic contacts," *J. Vac. Sci. Technol. B* **13**, 758 (1995).

[8] K. Tai, L. Yang, Y. Wang, J. Wynn, and A. Cho, "Drastic reduction of series resistance in doped semiconductor distributed Bragg reflectors for surface-emitting lasers," *Appl. Phys. Lett.* **56**, 2496 (1990).

[9] C. Van de Walle, "Band lineups and deformation potentials in the model-solid theory," *Phys. Rev. B* **39**, 1871 (1989).

CHAPTER II

BACKGROUND

The topics covered in this dissertation primarily revolve around the technology of distributed Bragg reflectors (DBRs) as used in vertical cavity surface emitting lasers (VCSELs). The intent of this chapter is to establish a basic understanding of VCSELs and DBRs. The first part describes the general structure and operation of a VCSEL. This includes discussions of the DBR structures in detail. The final part discusses the electrical properties, specifically the series resistance, of the DBR, and includes various methods used to lower that resistance.

2.1 VCSEL Structure and Operation

The device structure that has become known today as the vertical cavity surface emitting laser was first proposed in 1977 by Iga, *et al.* [1]. Figure 2.1 shows the basic VCSEL geometry. VCSELs operate on the same principles as edge emitting semiconductor lasers. Current is injected into the p-i-n junction to create a population inversion of carriers in the active region. Mirrors, R_1 and R_2, are used to create a standing wave of the spontaneous radiation in the cavity, and thus provide enough gain to achieve stimulated emission of photons. The major difference between a VCSEL and an edge emitter is

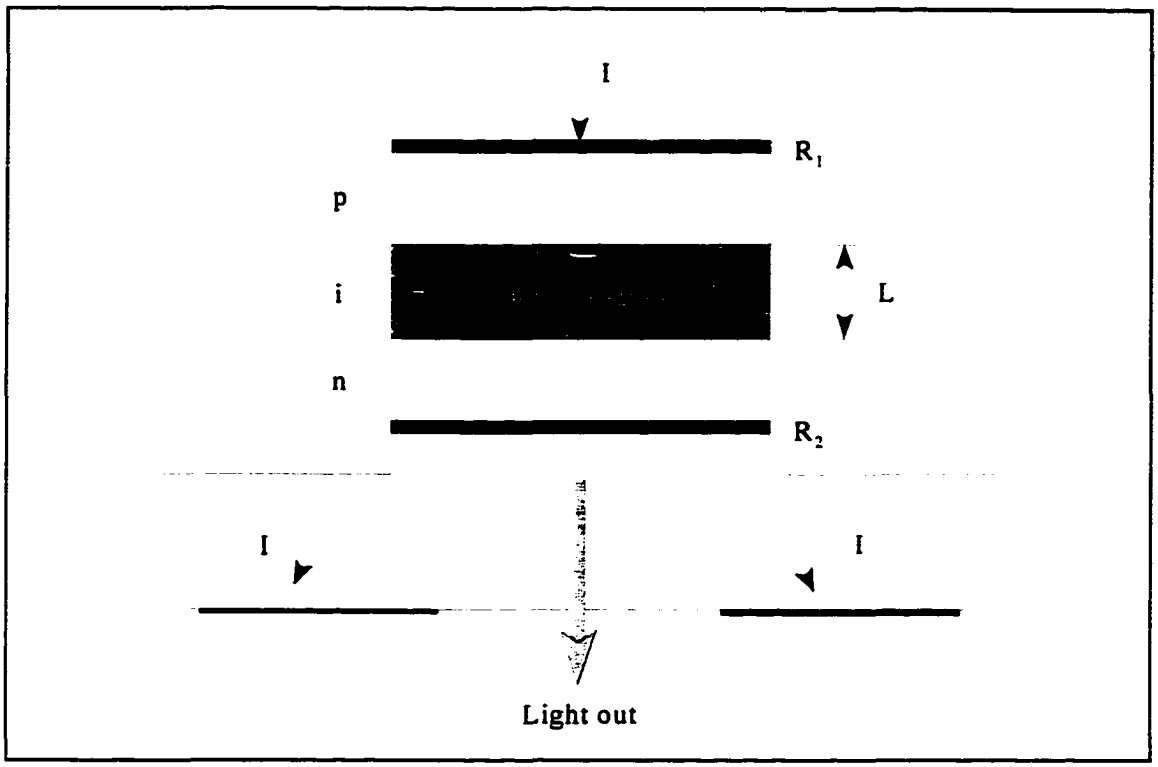

Figure 2.1 Basic VCSEL p-i-n laser geometry; L is the cavity length. R_1 and R_2 are the mirror reflectances, and I is the injected current.

reflected in their nomenclature, that is to say, in the direction of the emitted light relative to the growth direction of the semiconductor material layers. Edge emitters use cleaved facets as mirrors to create and define the optical cavity normal to the growth direction, while VCSELs employ alternate types of mirrors to create the cavity parallel to the growth direction, which is normal to the surface of the device.

The vertical orientation of the emitted light provides several advantages for the VCSEL over the edge emitter. Two-dimensional arrays of VCSELs can be fabricated easily using standard photolithography techniques. Initial device testing can be performed on the as-grown samples, without the need for cleaving into individual chips. The emitted radiation is usually in the form of a single longitudinal mode and can be tailored as a circular beam,

which eases the coupling of the light into optical fibers for communication systems. Integration with other optoelectronic devices is also easier as they can be stacked vertically on the same substrate with the VCSEL. Edge emitters have a clear advantage in output power over VCSELs, and thus different applications ensure each type of semiconductor laser a place in the diode laser market [2].

An important characteristic of the semiconductor laser is the threshold current, beyond which the output power of the laser increases almost linearly with the injected current. In order to obtain low threshold currents, it is desirable to have a very small active region in the laser. In an edge emitter, the length of the active region is defined by the cleaved facets, and is on the order of several hundred micrometers. For a VCSEL, on the other hand, the length of active region is parallel to the growth direction and can be controlled to the atomic scale by epitaxial growth. Typical VCSEL active region lengths are on the order of several hundred angstroms, or four orders of magnitude smaller than for edge emitters.

At threshold, the gain, g_{th}, in the laser cavity is equal to the loss and can be given by the familiar expression [3]

$$g_{th} = \alpha_i + \frac{1}{2L\Gamma}\ln\left(\frac{1}{R_1 R_2}\right) \tag{2.1}$$

where α_i is the absorption losses, Γ is the optical confinement factor, L is the length of the active region, and $R_{1,2}$ are the mirror reflectances. By examining the threshold gain relation, it is evident that the thin active region length in a VCSEL requires very highly reflective

mirrors, on the order of 99%. Mirrors such as specular metal reflectors were among the first applied in VCSELs, but due to optical absorption were unable to achieve high enough reflectances. Dielectric multilayers make use of small reflections due to refractive index discontinuities when moving from one material to another. By stacking enough of these layers together, very high reflectances can be obtained. Sample materials used for this dielectric mirror are alternating layers of SiO_2 and TiO_2, which are plasma deposited in several processing steps after the growth of the laser material. Semiconductors with energy band gaps larger than the photon energy of the emitted light are used as alternative dielectrics. They offer the advantage of epitaxially growing high quality mirrors in the same step and method as the active region.

Mirrors made from multilayer dielectric material stacks are called distributed Bragg reflectors (DBRs). DBRs are created by alternating layers of high and low indices of refraction, all of thicknesses equal to one-quarter of the wavelength of the laser light inside that layer. So for a DBR with a center wavelength of λ_o, the high and low index layer thicknesses, d, are given by

$$d_{H,L} = \frac{\lambda_o}{4n_{H,L}} \tag{2.2}$$

where $n_{H,L}$ is the index of refraction of the given layer. Figure 2.2(b) shows, using a horizontal orientation, the alternating refractive indices of the first few layers of a semiconductor AlAs/GaAs DBR. Note that for a given semiconductor alloy system, the energy band gap, Figure 2.2(a), is inversely proportional to the refractive index.

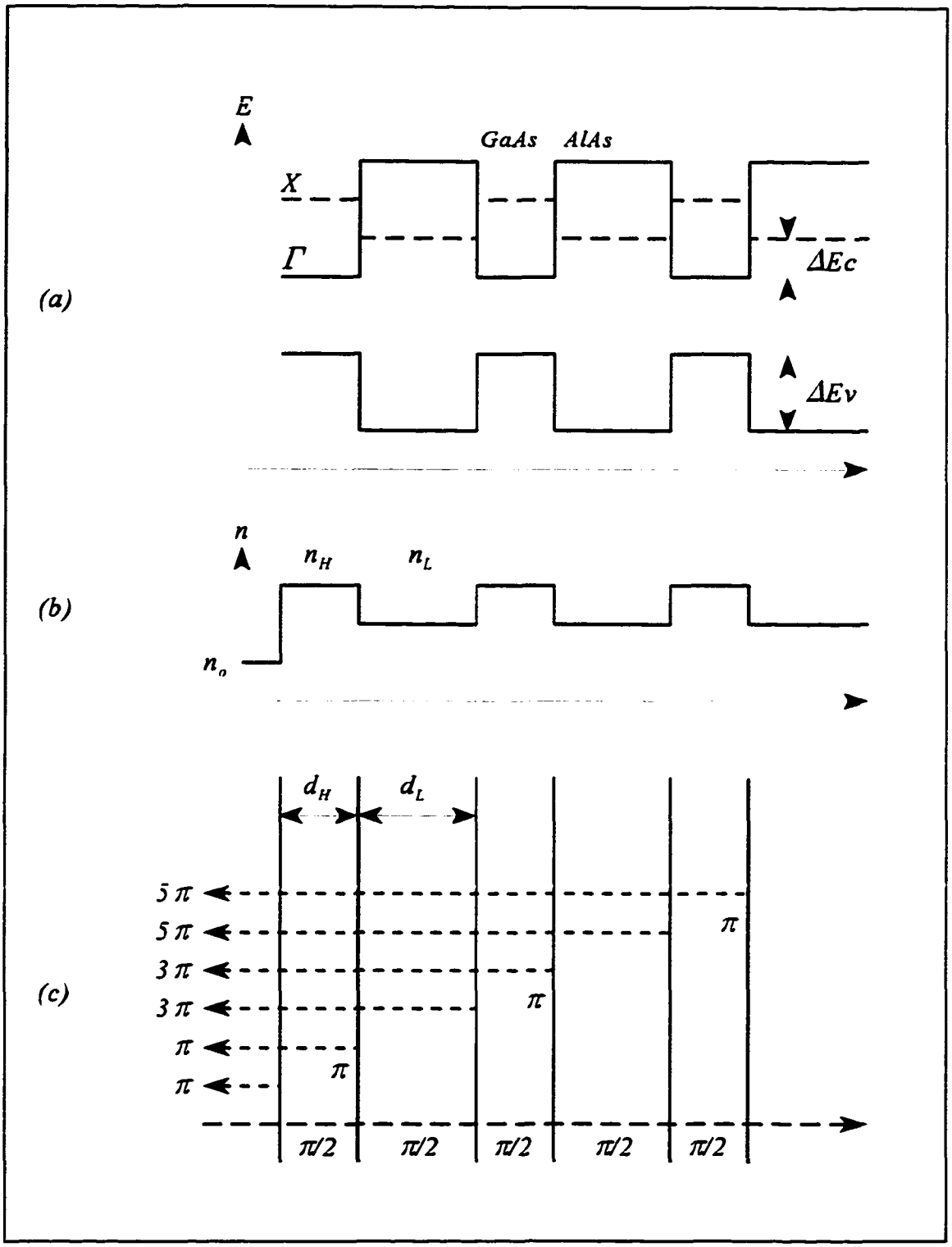

Figure 2.2 DBR layer schematic diagram demonstrating changes in (a) the energy band gap, (b) the refractive index, and (c) the phase of the reflected wave, all as a function of semiconductor layer material.

Figure 2.2(c) demonstrates the reflection of an electromagnetic wave at the dielectric interfaces due to the change in wave impedance. As mentioned above, the reflection at a given interface is small, but by stacking many such interfaces back to back the total reflection can be large. This is accomplished by using Equation (2.2) to choose the layer thicknesses to be quarter wavelength. Thus the reflected waves constructively interfere, that is they are all in phase as they leave the structure, and increase the total reflectance. The total reflectance, R, from a DBR stack is related to the refractive indices of the layer materials according to [3]

$$\sqrt{R}=\frac{1-(n_o/n_s)(n_H/n_L)^{2m}}{1+(n_o/n_s)(n_H/n_L)^{2m}} \tag{2.3}$$

where n_s and n_o are the refractive indices of the substrate and incident materials, respectively, and m is the total number of DBR periods. It follows that the number of periods required to obtain a certain total reflectance is inversely proportional to the difference in refractive index values of the two mirror layers, or

$$m(R)\propto\frac{n}{\Delta n} \tag{2.4}$$

where $\Delta n = |n_H - n_L|$. So in order to obtain 99% reflectance for a VCSEL, the larger the change in refractive index the fewer number of periods required for a given material system.

Figure 2.3 shows a typical VCSEL structure with semiconductor DBR mirrors. This structure is designed for operation at 1000 nm, which has applications as a source for

Erbium doped fiber amplifiers or as a solid state laser pump source. The DBRs are AlAs/GaAs (low/high index), and the active region is made up of three InGaAs quantum wells with GaAs barriers. The figure also shows, as the dashed line, the details of the

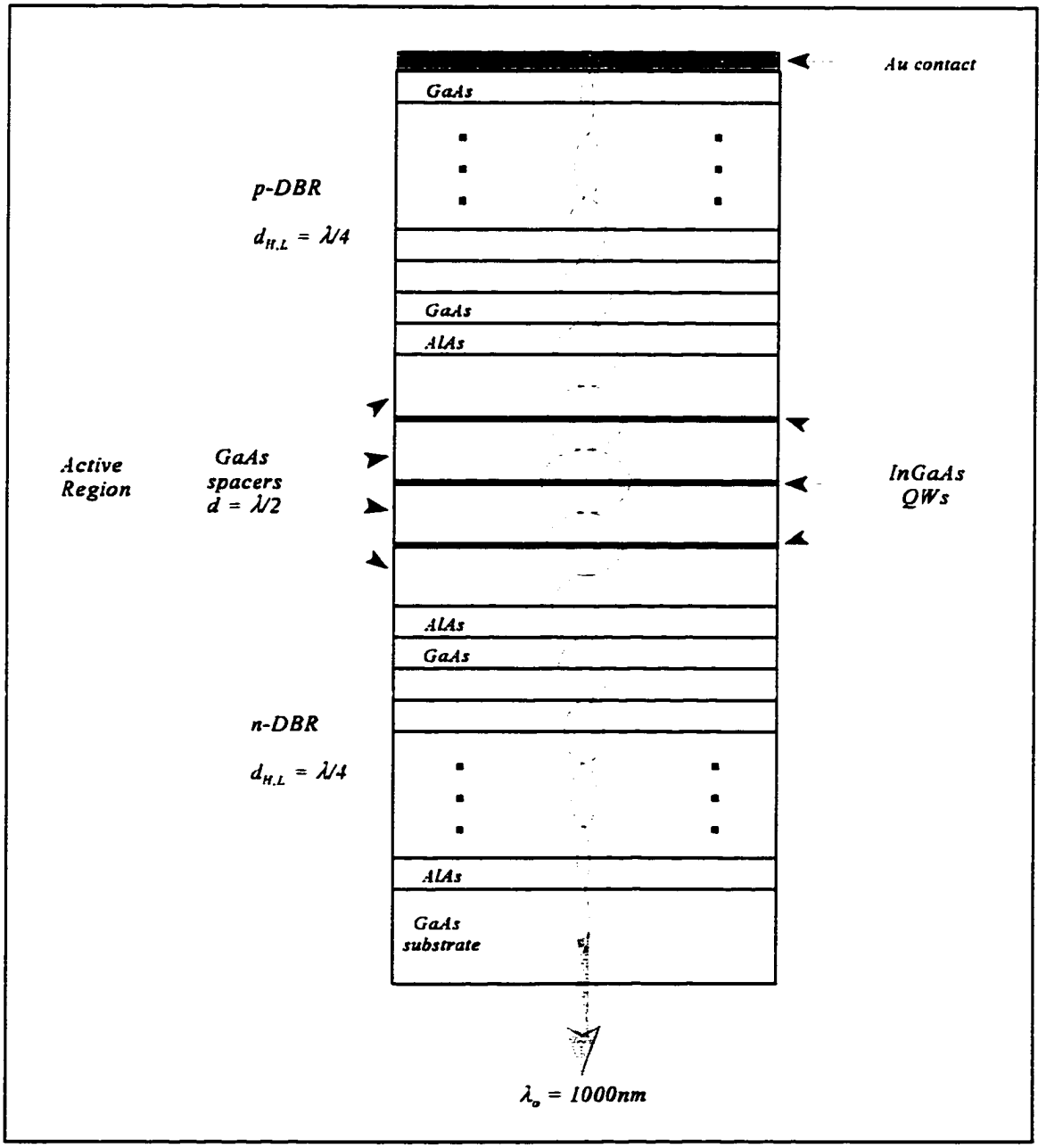

Figure 2.3 Sample VCSEL with semiconductor DBR mirrors.

electromagnetic standing wave in the cavity. The peaks of the wave in the DBRs are at the interfaces due to the quarter wavelength design, and the active region uses a resonant periodic gain design. This means that the cavity length is a multiple of half wavelengths, and the gain media (QWs) are placed at the peaks of the fields in order to maximize the gain per pass. The gold layer provides a contact and also helps to unbalance the mirror reflectances so that the generated light preferentially leaves through one mirror. The use of InGaAs, with a lower energy gap than GaAs, means that the light is not absorbed by the GaAs and can exit from the bottom.

2.2 Obtaining Low Resistance DBRs

One of the biggest limitations to any VCSEL operation is the high series resistances found in the thick structure. This causes thermal heating and detrimentally affects device thresholds and output power. Most of this resistance comes from the DBRs, where the periodic quarter wavelength stacks of high and low refractive index semiconductors are used to obtain the high reflectance needed for laser operation. Most of the DBR resistance is due to the large energy band offsets at the heterointerfaces between the individual material layers. Remember from Figure 2.2, the band gap varies inversely with refractive index in a given alloy system. This means that the large $\Delta n/n$, which is good for lowering the number of periods needed to get 99% reflectance, also results in a large band offset for semiconductor pairs such as AlAs/GaAs.

These band offsets form barriers to current flow, as Figure 2.4 demonstrates. Figure 2.4(a) shows the intrinsic conduction band line-up of AlAs/GaAs, as might be used in a

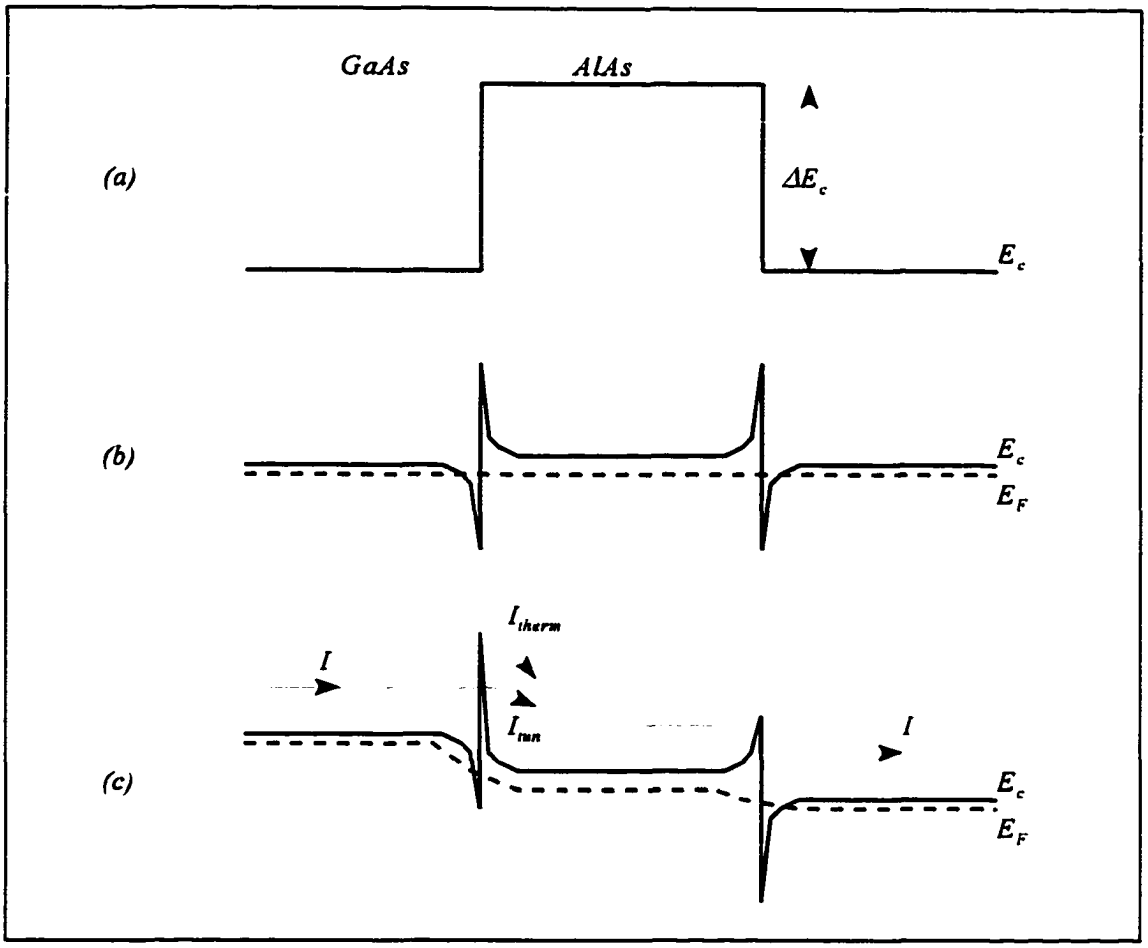

Figure 2.4 Heterojunction energy band offsets between AlAs and GaAs DBR layers. (a) Intrinsic conduction band lineup, E_c; (b) n-type conduction band and Fermi level, E_F, under zero bias; and (c) n-type conduction band and quasi-Fermi levels under a finite bias.

DBR. Figure 2.4(b) shows the same line-up for layers doped n-type and under no external bias. Here electrons have depleted from the AlAs into the GaAs in order to align the Fermi levels. This results in the band bending at the heterojunctions, and thus the barriers to carrier flow. With an applied bias across the whole structure, Figure 2.4(c), each n-n heterojunction sees a potential difference. In the case of the figure, the junction on the left is considered to be under reverse bias, indicating that this barrier presents a larger resistance to the current

flow. Here electron transport occurs either by thermionic emission over the barrier, I_{therm}, or by tunneling through the barrier, I_{tun}, if it is sufficiently thin. When the barriers are large compared to the thermal energy of the carriers, thermionic current is small and resistance is high. On the other hand, the junction on the right is considered to be under forward bias, where the barrier to electron flow is smaller and thus offers a much smaller resistance. Unfortunately, no matter which direction the bias is applied to the DBR, the structure always has these back to back junctions such that half are forward biased and half reversed biased.

It is important to note that although Figure 2.4 demonstrates this problem in the AlAs/GaAs material system for the conduction band in n-type DBRs, the effect is more pronounced in the valence band of p-type DBRs. This is due to both the larger valence band offset compared to the conduction band offset, and to the greater effective mass of the holes compared to the electrons. The thermionic current density over the barriers, J_{therm}, is dependent upon the effective mass of the carriers, m*, and the barrier height created by the band offset, ϕ_B, according to [4]

$$J_{therm} \propto (m^{*}) \exp\left(\frac{-q\phi_B}{kT}\right) \tag{2.5}$$

Here the barrier height dominates, and a larger value of ϕ_B in the valence band means a slower increase in current, which means a larger resistance value. The tunneling current density through the barriers, J_{tun}, is dependent upon the effective mass and the band offset according to [4]

$$J_{tun} \propto \exp[\frac{q}{E_{oo}}(V-\phi_B)] \quad (2.6)$$

where q is the carrier charge, V is the applied voltage, and E_{oo} is an energy parameter that is inversely proportional to the square root of the effective mass. In the tunneling current case, a small increase in either the effective mass or the barrier height, as occurs in the valence band when compared to the conduction band, means a slower increase in current with voltage and thus a larger resistance. Details of these relationships and the calculation of resistance values in DBR heterojunctions are given in Chapter III.

To achieve enough current flow through the DBRs into the active region of the VCSEL, the DBR layers must be highly doped, on the order of 10^{18} cm^{-3}. This narrows the depletion region at the heterojunction interfaces, thus narrowing the barriers to carrier transport and significantly increasing the tunneling current through the barriers. This reduces the series resistance so that enough carriers reach the active region and laser action occurs. The problem with doping the DBRs this high is that the impurities increase the free carrier absorption in the structure [3]. This absorption, which arises from optically induced band to band transitions involving band tail states, reduces the quality factor, or finesse, of the VCSEL cavity, and means more gain is required to reach threshold.

Rather than simply doping the DBRs uniformly at high levels in order to get the necessary tunneling, researchers have used various doping schemes to improve both the free carrier absorption and the series resistance. Doping modulation only uses high doping near the interfaces to help with carrier transport across the band discontinuities. In regions away

from the interfaces, say greater than roughly 200 Å, the doping is lowered by an order of magnitude. This has little effect on total stack resistance, while at the same time lowers the absorption [5]. Doping the DBR periods closest to the active regions less than the rest of the DBR also reduces free-carrier absorption losses, since more light passes through those layers than ones deeper in the stack [6]. Also, doping the top two DBR pairs much higher than the rest reduces contact resistance and lateral spreading resistance. Parabolic modulation doping at the interfaces has also been shown to result in a spatially constant electron concentration which will adjust itself in such a way that it results in a flat band edge [7].

In addition to doping schemes, several methods have been used to lower the series resistance via smoothing the heterojunction interfaces. Figure 2.5 schematically demonstrates some of these methods. The simplest method is the insertion of a barrier reduction layer between the two quarter wavelength layers of the DBR [8, 9]. For example, the AlAs/$Al_{0.5}Ga_{0.5}As$ mirrors Sandia used in their visible VCSELs contained a 10 nm $Al_{0.75}Ga_{0.25}As$ barrier reduction layer at each interface [8]. A more sophisticated approach uses some type of continuous composition grading segments. These include linear [10], piecewise linear [11], parabolic [12], sinusoidal [13], and superlattice [14] grading. These are usually incorporated right into the quarter wavelength layers, as opposed to separating them. Sandia also has used 0.15λ layers of AlAs and $Al_{0.5}Ga_{0.5}As$ separated by 0.1λ thick continuously graded segments [6]. This is not simply substituting a couple hundred angstroms of graded segment while taking away the same thickness of bulk region. The changing refractive index requires different physical thicknesses, and often complex modeling is needed to optimize the design and maximize the total reflectance.

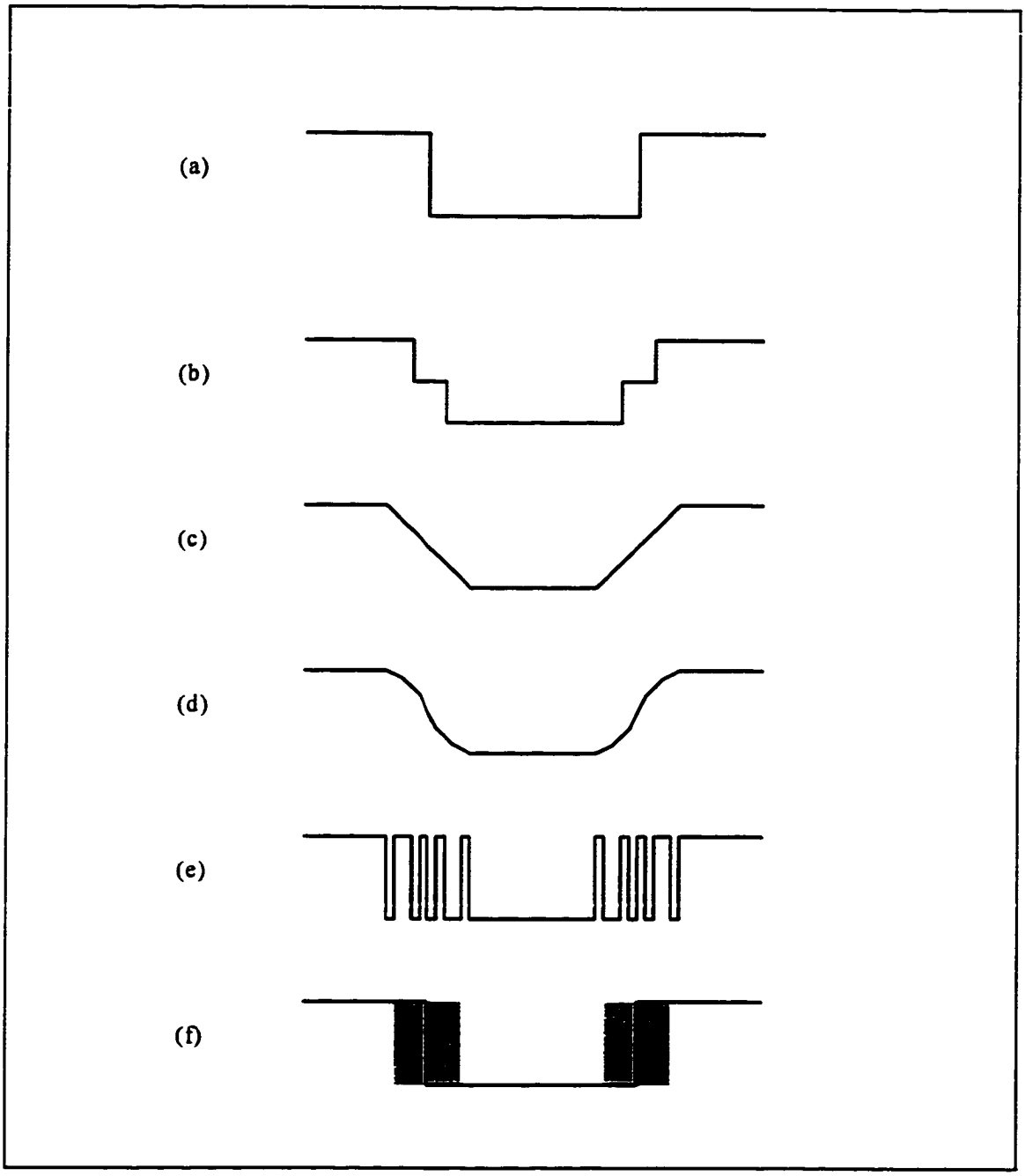

Figure 2.5 Schematic diagram representing various schemes used to reduce DBR series resistance compared to the simple quarter wavelength stack (a). Methods include (b) a single barrier reduction layer; (c) linear, (d) parabolic, and (e) superlattice composition grading, as well as (f) modulation doping, where the shaded regions are doped heavier than the unshaded regions.

In contrast to the above methods, this project lowers the series resistances of DBRs in the visible wavelengths by choosing semiconductor material pairs which have naturally small energy band offsets. This means that the dominant transport method is thermionic emission over the small barriers. The primary benefit of this novel method is that it simplifies the epitaxial growth process. Since the materials have naturally small offsets there is no need for the insertion of composition and dopant grading regions in the DBR stacks. While it may be relatively easy to design and program these graded regions in epitaxial growth, their control and reproducibility are more challenging. With the large number of periods and precise thicknesses necessary for DBRs, their growth is complicated enough, and anything that can be done to simplify it should be considered. This novel method also simplifies the design of the DBR to basic quarter wavelength layers. Complex modeling to maintain the optimum reflectance, due to the addition of barrier reduction grading which forces a change in layer thicknesses, is no longer needed. Another benefit is the lowering of the overall doping level, since the very high levels are not necessary to increase tunneling current through the interfaces. This will reduce the free carrier optical absorption caused by impurities, which will help to keep down the threshold gain of the VCSEL, without increasing the resistance.

REFERENCES: CHAPTER II

[1] K. Iga, F. Koyama, and S. Kinoshita, "Surface emitting semiconductor lasers," *IEEE J. Quantum Electron.* **24**, 1845 (1988).

[2] J. Jewell, J. Harbison, A. Scherer, Y. Lee, and L. Florez, "Vertical-cavity surface-emitting lasers: design, growth, fabrication, characterization," *IEEE J. Quantum Elec.* **27**, 1332 (1991).

[3] T. E. Sale, Vertical Cavity Surface Emitting Lasers; John Wiley & Sons, Inc.: New York, 1995.

[4] G. Robinson, "Schottky Diodes and Ohmic Contacts for the III-V Semiconductors," in Physics and Chemistry of III-V Compound Semiconductor Interfaces, edited by C. Wilmsen; Plenum Press: New York, 1985.

[5] M. Sugimoto, H. Kosaka, K. Kurihara, I Ogura, T. Numai, and K. Kasahara, "Very low threshold current density in vertical cavity surface emitting laser diodes with periodically doped distributed Bragg reflectors," *Electron. Lett.* **28**, 385 (1992).

[6] R. Schneider, Jr., K. Choquette, J. Lott, K. Lear, J. Figiel, and K. Malloy, "Efficient room-temperature continuous wave AlGaInP/AlGaAs (670 nm) vertical-cavity surface-emitting laser diodes," *IEEE Photonics Tech. Lett.* **6**, 313 (1994).

[7] E. Schubert, L. Tu, G. Zydzik, R. Kopf, A. Benvenuti, and M. Pinto, "Elimination of heterojunction band discontinuities by modulation doping," *Appl. Phys. Lett.* **60**, 466 (1992).

[8] R. Schneider, Jr. and J. Lott, "Cavity design for improved electrical injection in InAlGaP/AlGaAs visible (639-661 nm) vertical-cavity surface-emitting laser diodes," *Appl. Phys. Lett.* **63**, 917 (1993).

[9] K. Tai, K. Huang, C. Wu, and J. Wynn, "Visible InGaP/InGaAlP quantum well top surface emitting laser diodes," *Appl. Phys. Lett.* **63**, 2732 (1993).

[10] M. Hong, J. Mannaerts, J. Hong, R. Fischer, K. Tai, J. Kwo, J. Vandenberg, Y. Wang, and J. Gamelin, "A simple way to reduce series resistance in p-doped semiconductor distributed Bragg reflectors," *J. Crystal Growth* **111**, 1071 (1991).

[11] S. Chalmers, K. Lear, and K. Killeen, "Low resistance wavelength-reproducible p-type (Al,Ga)As distributed Bragg reflectors grown by molecular beam epitaxy," *Appl. Phys. Lett.* **62**, 1585 (1993).

[12] M. Peters, B. Thibeault, D. Young, J. Scott, F. Peters, A. Gossard, and L. Coldren, "Band-gap engineered digital alloy interfaces for lower resistance vertical-cavity surface-emitting lasers," *Appl. Phys. Lett.* **63**, 3411 (1993).

[13] M. Hong, D. Vakhshoori, J. Mannaerts, and Y. Hsieh, "Low resistivity vertical-cavity surface emitting lasers grown by molecular-beam epitaxy using sinusoidal-composition grading in mirrors and *in situ* nonalloyed ohmic contacts," *J. Vac. Sci. Technol. B* **13**, 758 (1995).

[14] K. Tai, L. Yang, Y. Wang, J. Wynn, and A. Cho, "Drastic reduction of series resistance in doped semiconductor distributed Bragg reflectors for surface-emitting lasers," *Appl. Phys. Lett.* **56**, 2496 (1990).

CHAPTER III

THEORETICAL CALCULATIONS

The goal of this project was to lower the series resistance in distributed Bragg reflectors (DBRs) operating in the visible wavelengths by selecting semiconductor material pairs with naturally low energy band offsets. This is a very different approach to the problem than has been previously addressed, as discussed in Chapter II. Before proceeding with experimental work, a theoretical study was undertaken to determine the best material candidates available to achieve this goal. The first section of this chapter describes that study. This includes sections discussing the semiconductor energy band offset theory and how it was applied to the available alloys, the band offset calculations, and the evaluation of theoretical results and resulting choice of optimal heterojunction materials for low band offset DBRs. The final section of this chapter describes theoretical DBR resistance calculations. These will help confirm the choice of optimal semiconductor material pairs, and provide a comparison for measured results later in this dissertation.

3.1 Energy Band Calculations

Semiconductor energy band offset calculations performed in this work closely followed a paper by M. Krijn [1], who laid out a procedure for estimating band offsets and

effective masses via interpolation of the Van de Walle "model solid theory" [2]. These original papers should be consulted for details of Van de Walle's theory and Krijn's application of it. The discussion below is intended to provide an overview of the band offset theory and the process by which it was applied in this project. The choice of optimum semiconductor material systems for low band offset DBRs is also discussed in this section.

3.1.1 Model Solid Theory for Semiconductor Band Offsets

The model solid theory has two main points. First is the generation of a self-consistent and accurate energy band structure. Second is the alignment of that structure on an absolute energy scale. Local-density-function (LDF) calculations on individual bulk semiconductors described by pseudo potentials are used to determine the valence band positions. Experimental band gap values are then used to find the conduction band positions since the LDF theory fails to correctly determine band gaps. Any errors in the LDF valence band determinations are small and similar for most semiconductors, thus when looking at differences, such as in a band lineup between two materials, the errors tend to cancel. The absolute energy scale is accomplished by modeling the material solid as a superposition of neutral atoms, each having its electrostatic energy strictly defined with respect to the vacuum level. Thus the average electrostatic potential, around which bulk calculations can be carried out, is given on an absolute energy scale. So the model solid theory uses the average potential on a definite scale as the pseudo potential in the LDF calculations, and thus obtains meaningful semiconductor energy band positions.

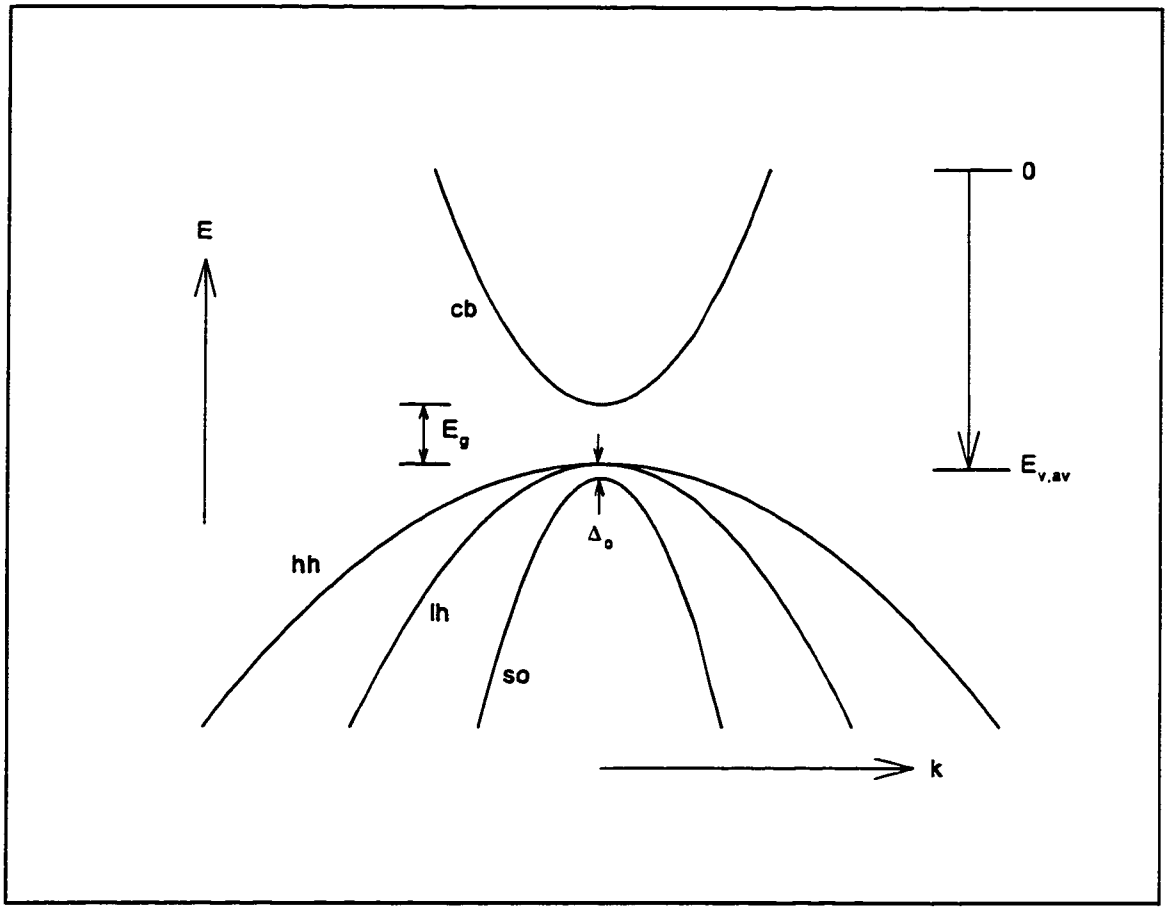

Figure 3.1 Energy band diagram in momentum (k) space as created using the Model Solid Theory.

Van de Walle used the model solid theory to determine "absolute" band position values for various binary semiconductors [2]. First, the average peak position of the three topmost Γ valence bands, $E_{v,av}$, was calculated. As demonstrated in Figure 3.1, these three bands are the heavy hole (hh), the light hole (lh), and the spin-orbital split-off (so) bands. In an unstrained semiconductor, the peak of the hh and lh valence bands are coincident, while the peak of the split off band is below the other two by an energy value Δ_o, which is called the spin-orbital splitting. From this $E_{v,av}$ base point, and knowing the experimental spin-orbital splitting (Δ_o) and direct band gap values ($E_{g,\Gamma}$), the conduction band level (cb) was

found. The calculated numbers for $E_{v,av}$ carry no physical meaning since they are just a reference to an arbitrary absolute energy level. However, when comparing two semiconductor materials, the differences in their values are meaningful. These meaningful differences allow band offsets to be accurately determined. It should be noted that the model solid theory can also be used to calculate band shifts due to hydrostatic strain, corresponding to volume changes in crystal lattices, but strain effects were not considered in calculations for this project.

Krijn took the binary semiconductor data that Van de Walle calculated with the model-solid theory, and applied an interpolation scheme to find corresponding ternary and quaternary data [1]. The interpolation used quadratic expressions with appropriate binary data and bowing parameters. For convenience the results were given in terms of a product expansion of quaternary mole fractions (x and y), and then the expansion coefficients were tabulated. To perform band offset calculations, the coefficients and the mole fractions are used to calculate the appropriate quantities $E_{v,av}$, Δ_o, and $E_{g,\Gamma}$ for both semiconductors in question. Then E_v and E_c are found for both and compared to obtain the band offsets.

3.1.2 Band Offset Calculations

Rather than performing theoretical calculations on all possible semiconductor material combinations, the choices were narrowed by other considerations. As a starting point, the Gas Source Molecular Beam Epitaxy (GSMBE) system limited the available materials to the III-V semiconducting arsenide and phosphide alloys. Figure 3.2 presents the so-called III-V semiconductor roadmap, a plot of energy band gap versus lattice constant, for

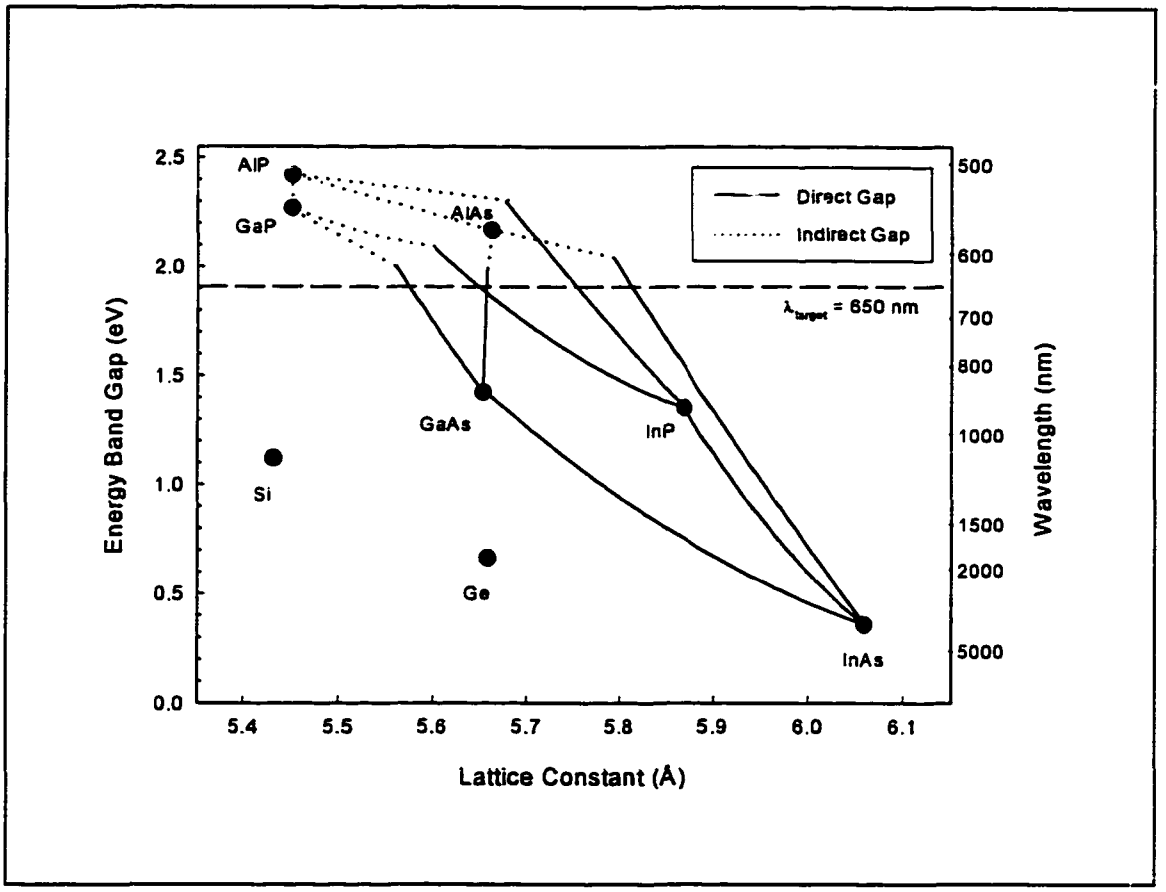

Figure 3.2 The III-V semiconductor roadmap.

these materials. Included on the figure is a dashed line representing the energy level of the 650 nm target wavelength for the DBRs in this project. In order for the DBRs to be transparent to light at this target wavelength, their alloy composition must lie above this line. GaAs substrates were used because a wider range of semiconductors above the line are lattice matched to that substrate. These material candidates included the ternary $Al_xGa_{1-x}As$, which is lattice matched for all x, and the quaternary $Al_xGa_yIn_{1-x-y}P$, which is lattice matched for all x and y such that 1-x-y=0.484. *Throughout the rest of this dissertation xT will be used to refer to the Al mole fraction in the AlGaAs ternary, and xQ will be used to indicate the Al mole fraction in the AlGaInP quaternary.* Note that by defining xQ, the Ga value, y, is also

defined by the above relation. In addition, these materials are limited by the dashed line in Figure 3.2 to xT>0.37 for the AlGaAs and to xQ>0.05 for the AlGaInP.

The band offset calculations were performed using Mathcad, a mathematical problem solving software tool. The appropriate matrices and equations were entered from Krijn's paper to calculate $E_{v,av}$, Δ_o, and $E_{g,\Gamma}$ values for the AlGaAs and AlGaInP alloy systems. From these values the positions of the top of the valence band and the bottom of the conduction band were determined and compared. In addition, when xT>0.45 so that the X-band crosses below the Γ-band, the indirect band gap of AlGaAs, $E_{g,X}$, was calculated using an equation from Adachi [3] and was then used to determine the conduction band position. A series of calculations and comparisons were performed. Each started with a single material for one layer, such as AlAs, and then varied the aluminum concentration of the other alloy, say AlGaInP. In this manner a plot was made of the band offsets at the heterojunction between the two materials as a function of the aluminum concentration.

As a guideline for determining a small band offset, only semiconductor pairs with offsets of less than 100 meV were considered potential candidates. A sample Mathcad file is given in Appendix B for the AlAs/AlGaInP heterojunction lineup. Figure 3.3 shows the plot, generated by this program, of the difference in the energy band gap (ΔE_g) and the conduction (ΔE_c) and valence (ΔE_v) band offsets as a function of the quaternary composition. Figure 3.4 summarizes the changing AlAs/AlGaInP band lineups with changing xQ values. Note that the band diagrams in Figure 3.4 are not drawn to scale. The top row of energy band diagrams demonstrates how the lineup starts as Type I for small xQ, with the AlAs band gap larger than the AlGaInP, then changes to Type II for intermediate values of xQ, and

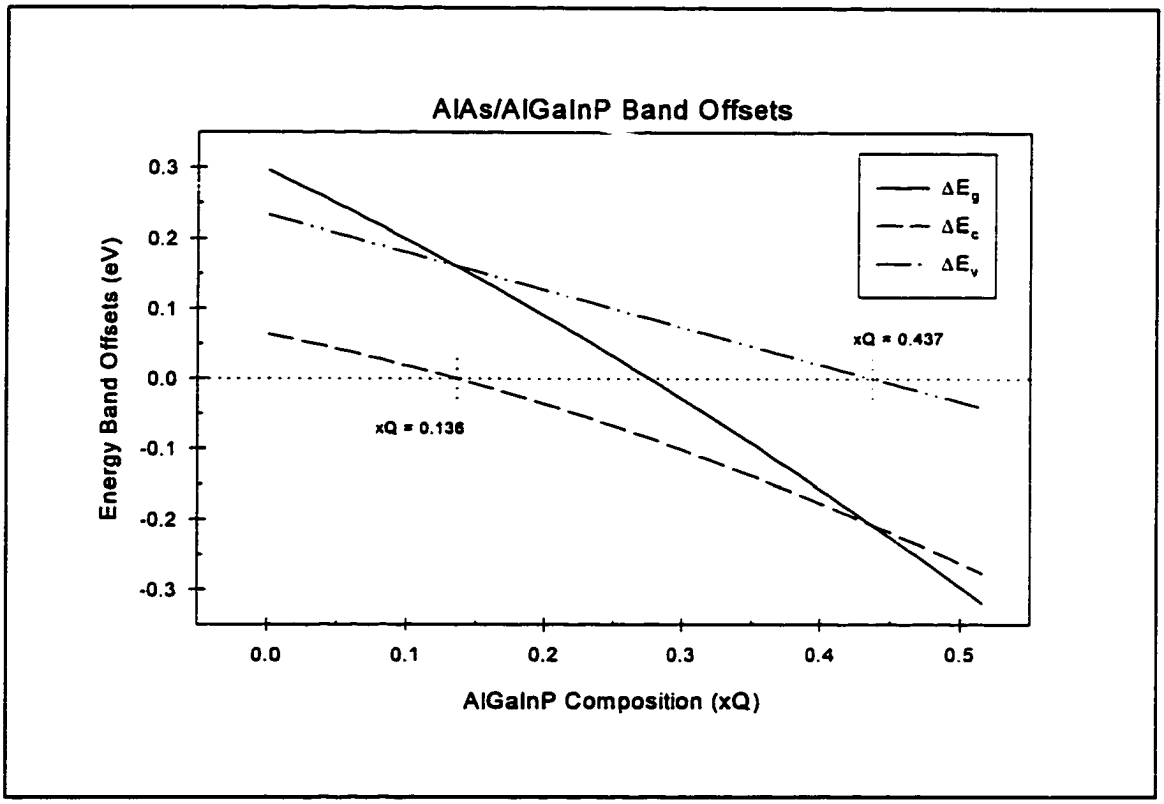

Figure 3.3 Plot of the AlAs/AlGaInP band offsets as a function of the quaternary composition. Zero conduction and valence band offsets points are marked.

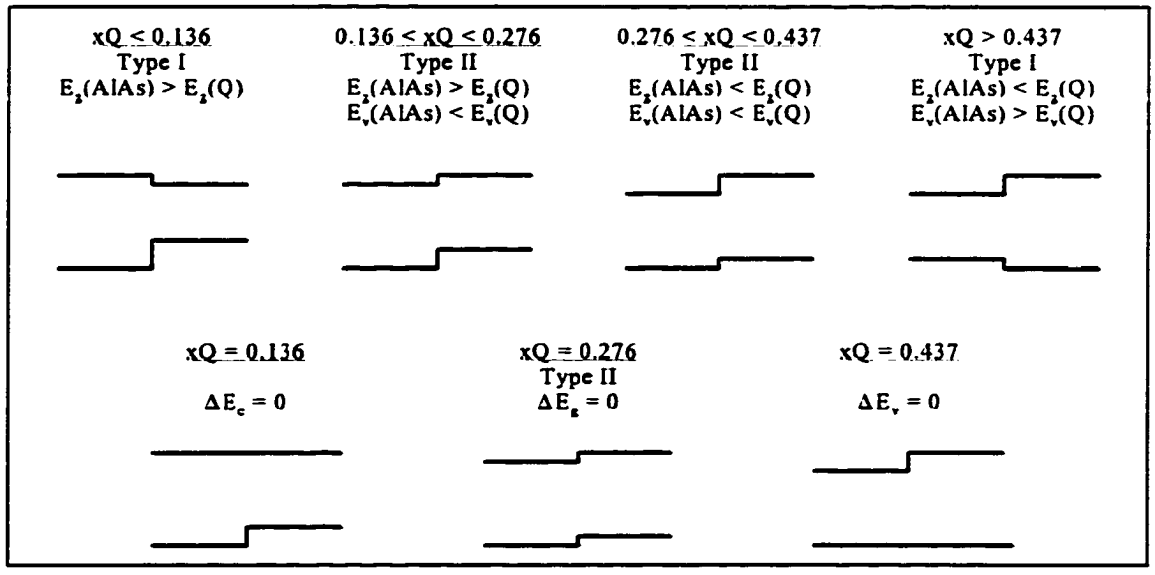

Figure 3.4 Sketches of the AlAs/AlGaInP band line ups for each significant composition region (top), and at critical values of xQ (bottom); not drawn to scale.

finally becomes Type I again for large values of xQ, except now the AlGaInP has the larger band gap. The bottom row of energy band sketches shows the three critical xQ values that give zero offsets in the band gap, conduction band, and valence band. From the dashed curve in Figure 3.3, potential candidates for low band offset n-type DBRs, where the conduction band offset is less than 100 meV, were determined to be any AlAs/AlGaInP combination with a quaternary composition of less than 0.3 ($xQ<0.30$). In addition, by examining the valence band offset curve in Figure 3.3, material combinations with composition values greater than 0.25 ($xQ>0.25$) provide potential low band offset p-type DBR candidates.

Using similar Mathcad programs, band offsets were calculated and plotted for various AlGaAs/AlGaInP alloy combinations. Figures 3.5 through 3.8 show plots of the energy band offsets as a function of aluminum composition, either xQ or xT depending upon which material was varied and which was kept constant, for the other four combinations studied. Each plot marks points where the conduction and valence band offsets are zero, when applicable. In addition, some plots contain curves with discontinuities. These discontinuities are due to the transition from performing the calculations using the direct to using the indirect band gap of the material whose composition is being varied along the x-axis. For example, the changes in the energy band gap and conduction band curves of Figure 3.7 show discontinuities at $xT=0.45$ due to the transition from the direct (Γ band) to the indirect (X-band) band gap AlGaAs. All of the curves in the five band offset figures were examined to determine which material combinations provided potential low band offset DBR candidates. Complete lists of candidates for n-type and p-type DBRs were compiled and those satisfying the target wavelength requirement have been summarized in Tables 3.1 and 3.2, respectively.

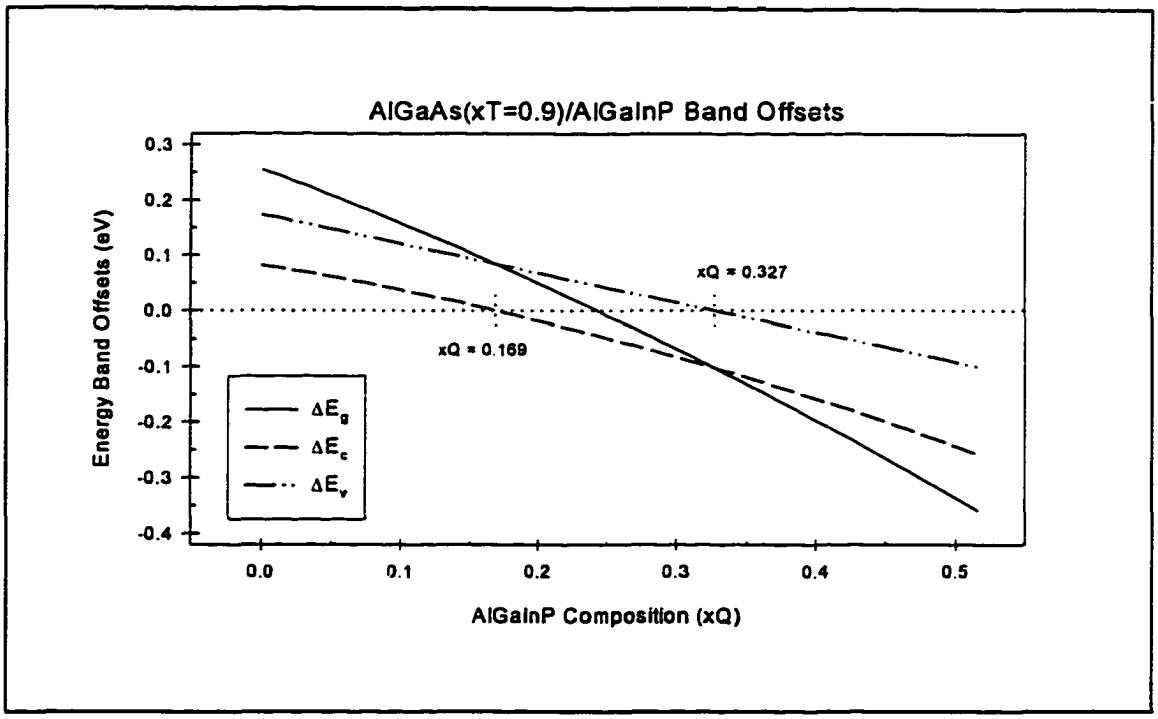

Figure 3.5 Plot of the AlGaAs(xT=0.9)/AlGaInP band offsets as a function of xQ, with zero offset intersections marked for the conduction and valence bands.

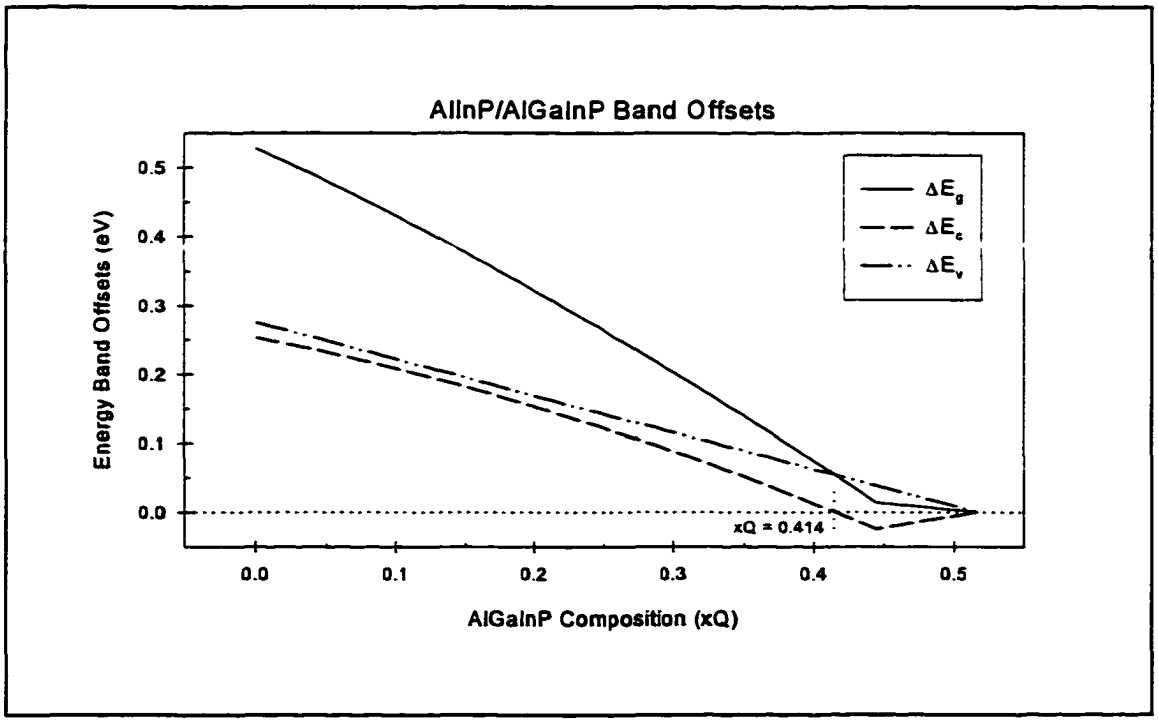

Figure 3.6 Plot of the AlInP/AlGaInP band offsets as a function of the quaternary composition, with the zero offset conduction band point indicated.

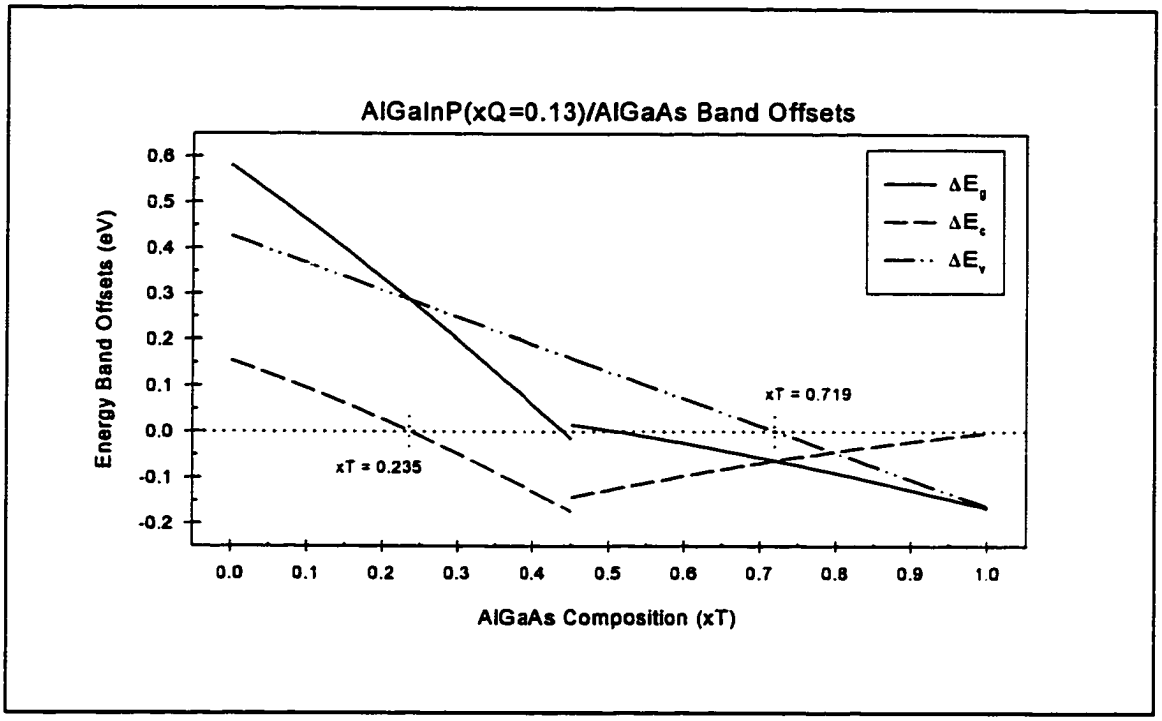

Figure 3.7 Plot of the AlGaInP(xQ=0.13)/AlGaAs band offsets as a function of xT, with zero offset points marked for the conduction and valence bands.

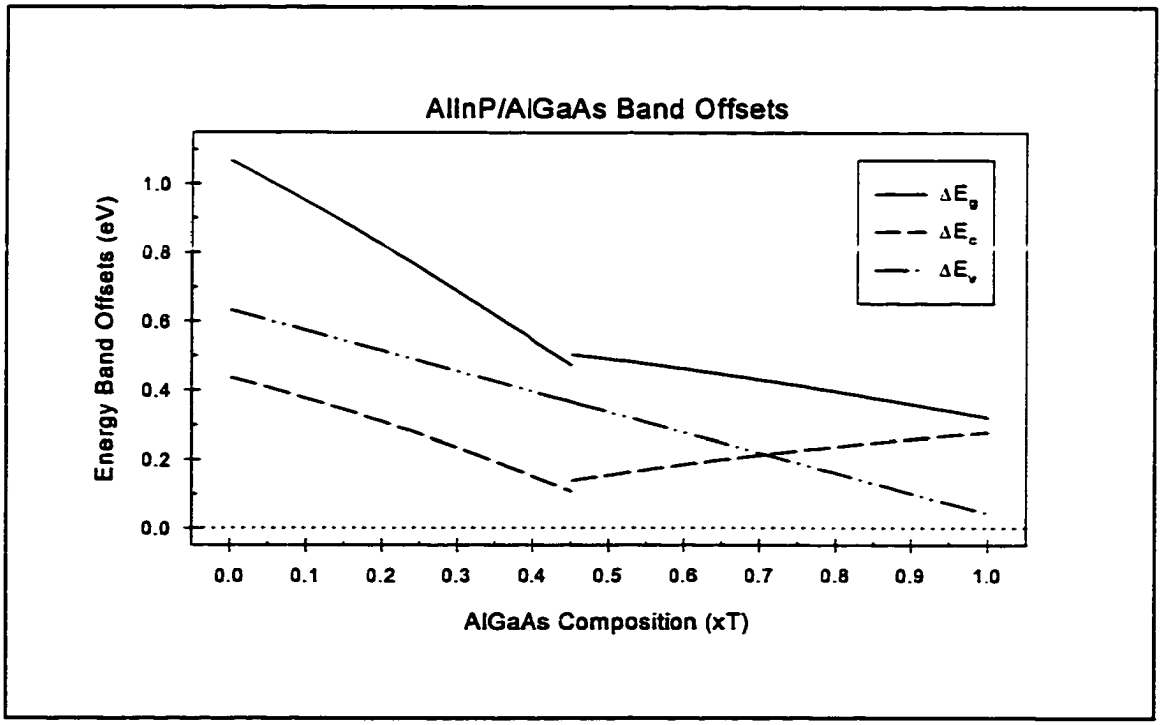

Figure 3.8 Plot of the AlInP/AlGaAs band offsets as a function of the AlGaAs ternary composition. Note that there are no points of zero band offset.

Table 3.1 Material candidates for n-type DBRs with their allowed composition ranges for low conduction band offset (ΔE_c<100 meV), and the maximum change in index of refraction ($\Delta n/n$) in that range.

Material System (fixed / variable)	Composition Range	Maximum $\Delta n/n$ (%)
AlInP / AlGaInP	xQ > 0.28	4.0
AlAs / AlGaInP	xQ < 0.30	9.5
AlGaInP / AlGaAs (xQ=0.13)	xT > 0.59	6.6

Table 3.2 Material candidates for p-type DBRs with their allowed composition ranges for low valence band offset (ΔE_v<100 meV), and the maximum change in index of refraction ($\Delta n/n$) in that range.

Material System (fixed / variable)	Composition Range	Maximum $\Delta n/n$ (%)
AlInP / AlGaInP	xQ > 0.33	3.0
AlInP / AlGaAs	xQ > 0.90	2.5
AlAs / AlGaInP	xQ > 0.25	4.2
AlGaAs / AlGaInP (xT=0.9)	xQ > 0.14	4.3
AlGaInP / AlGaAs (xQ=0.13)	0.55 < xT < 0.89	4.3

3.1.3 Evaluation and Choice of Optimum DBR Materials

As mentioned before and demonstrated in the tables above, calculations were performed for all combinations of AlGaAs and AlGaInP. Several of these alloy material combinations have conduction or valence band offsets of less than 100 meV. However, in order to be a good choice for a DBR, the change in index of refraction, $\Delta n/n$, must also be

examined. Remember that the number of mirror periods necessary for a given reflectance is inversely proportional to $\Delta n/n$. So a larger index change means a smaller number of periods needed in the DBR, and also implies a smaller stack resistance. Using theoretical values of refractive indices for these material systems [3, 4, 5], the differences were calculated and are included in Tables 3.1 and 3.2. Using this information, several systems, such as AlInP/AlGaInP, were eliminated. Also, as mentioned before, the target wavelength of 650 nm means the band gaps must be larger than 1.9 eV, which eliminates all AlGaInP for $xQ<0.05$ and all AlGaAs for $xT<0.5$. Using all of these criteria, the optimal semiconductor material systems selected to achieve low band offset DBRs were:

- For n-type: $AlAs/Al_{0.10}Ga_{0.42}In_{0.48}P$

  $\Delta E_c = 20$ meV

  $\Delta n/n = 7.2\%$

- For p-type: $Al_{0.9}Ga_{0.1}As/Al_{0.14}Ga_{0.38}In_{0.48}P$

  $\Delta E_v = 100$ meV

  $\Delta n/n = 4.3\%$

It should be noted that using the above criteria, there is virtually no difference between the AlGaAs/AlGaInP system chosen for the p-type DBR and the AlAs/AlGaInP ($xQ=0.25$) system. In fact, the latter would be simpler to grow in the CSU GSMBE system and would provide nice symmetry with the n-type choice. However, as will be discussed in detail in Chapter V, the difficulty of doping AlAs p-type with beryllium necessitated the move to the AlGaAs/AlGaInP system selected.

3.2 DBR Resistance Calculations

In order to be sure that the low band offset approach will indeed lower the DBR series resistance, theoretical resistance calculations were performed for the two DBRs made from the optimal alloy pairs chosen in the previous section. These results were then compared to similar calculations done on DBRs in the AlInP/AlGaInP material system, where an AlInP layer replaces the low index AlAs and AlGaAs layers in the n-type and p-type DBRs, respectively. DBRs in this alternative system, which previously have been studied for visible wavelength VCSELs [6, 7], have much larger conduction and valence band offsets which should result in larger DBR resistances, and thus these alternate DBRs serve as good choices for control samples. All calculations were again carried out using Mathcad programs specifically created for this purpose.

The total resistance of a DBR stack can be modeled as a series connection of individual resistances. Figure 3.9 depicts this concept using the symbols n_H and n_L to represent the quarter wavelength layers of high and low index of refraction, respectively. With the current passing down through the stack, the total resistance between points A and B, R_{AB}, is the sum of the individual resistances due to the bulk layers, R_H and R_L, plus the sum of the resistances due to the heterojunction barriers between the layers, R_{HL} and R_{LH}. In these latter resistances, the order of the subscripts indicates the barrier resistance when current flows from the first subscript layer into the second. Thus R_{HL} represents the resistance going from layer n_H into n_L. The resistance going from the bottom DBR layer into the substrate, R_{HS}, is also included in the calculations. However, the metal-semiconductor contact resistance is not calculated since the actual measurements will account for that.

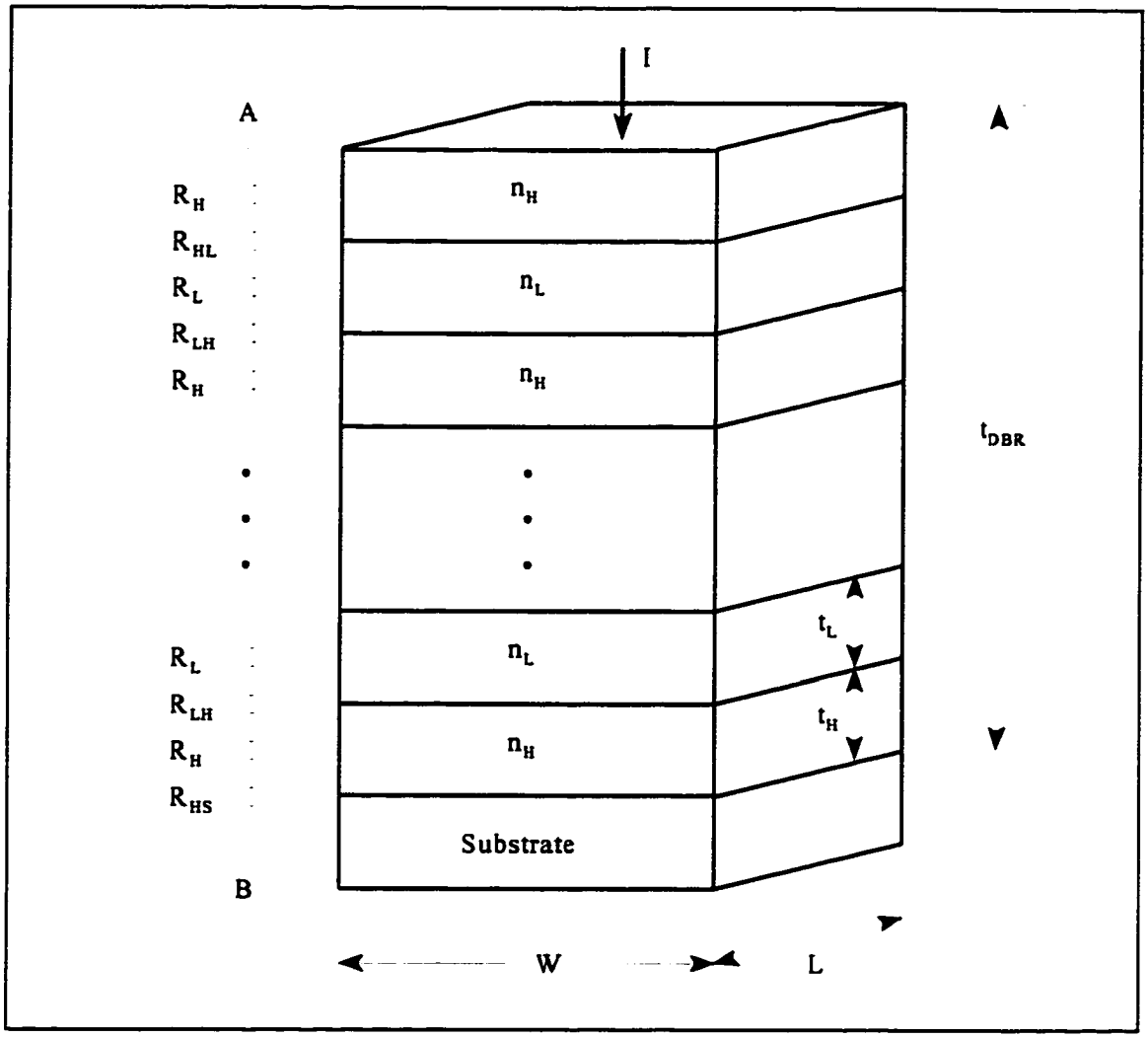

Figure 3.9 DBR geometry for determining the series resistance of the stack.

The resistance calculations of this section are separated into the determination of the bulk layer resistances and the determination of the barrier resistances. These are then summed for the given DBR stack configuration, which depends upon the total number of periods and the material of the layers. To remove any dependency upon the mesa geometry, the specific contact resistances, R_c, with units of $\Omega \cdot cm^2$, are calculated instead of the absolute resistances. The rest of this chapter presents the specific contact theory for bulk layers and barriers, and gives the results of the calculations for the four DBRs of interest.

3.2.1 Specific Contact Resistance Theory

From the DBR geometry of Figure 3.9, the vertical series resistance of the individual bulk layers in the stack, either the high or low index layers, is given by

$$R_{H(L)} = \rho \frac{t_{H(L)}}{LW} \tag{3.1}$$

where L and W define the area of the DBR mesa, and $t_{H(L)}$ is the thickness of the layer. The material resistivity, ρ, is defined for n-type and p-type semiconductors by

$$\rho = \frac{1}{q\mu_n N_D} \quad \text{and} \quad \rho = \frac{1}{q\mu_p N_A}, \tag{3.2}$$

respectively, where $\mu_{n,p}$ is the mobility of carriers in the material and $N_{D,A}$ is the doping level in the material. By normalizing to the area of the mesa, the specific contact resistance due to the individual bulk material layers, $R_{c,H(L)}$, can be defined as

$$R_{c,H(L)} = R_{H(L)} * A = \rho t_{H(L)} \tag{3.3}$$

Since the DBR consists of a multiple number of periods, m, of alternating high and low index layers, the total contact resistance due to the bulk layers, $R_{c,bulk}$, can be determined by the sum of the contribution from each quarter wavelength layer of both materials. Thus, using Equations (3.2) and (3.3), $R_{c,bulk}$ is

$$R_{c,bulk} = m[\rho_H t_H + \rho_L t_L] \tag{3.4}$$

As discussed in Chapter II, the energy band offsets at the heterojunctions in the DBRs form barriers to carrier transport. In other words, they contribute to the series resistance of the DBR stack. As demonstrated by Figure 2.4, carrier transport across the barriers occurs by thermionic emission over the barrier, by tunneling through the barrier, which is often called field emission, or by some combination of these two transport mechanisms. Thermionic emission, field emission, and thermionic-field emission are each valid only over a certain range of doping and temperature, which will be spelled out in detail below. It is assumed that the semiconductor heterojunctions in the following calculations can be modeled as metal-semiconductor Schottky contacts. Furthermore, potential energy barriers at the junctions are assumed to be triangular-shaped with height ϕ_B. Theoretical expressions from reference [8] are used below.

At very high doping levels or at low temperatures, carrier transport occurs via field emission. The current density is expressed by

$$J_F = J_{OF}\exp(qV/E_{oo}) \tag{3.5}$$

where

$$J_{OF} = \frac{\pi A^* T}{kC_1 \sin(\pi kTC_1)}\exp(-q\phi_B/E_{oo}) \tag{3.6}$$

$$C_1 = (2E_{oo})^{-1}\ln[-4(\phi_B - V)/\xi] \tag{3.7}$$

$$E_{oo} = \frac{hq}{4\pi}\sqrt{\frac{N_D}{m^* \epsilon_s}} \tag{3.8}$$

and where the Richardson constant is defined as

$$A^{*}=4\pi qm^{*}k^{2}/h^{3} \tag{3.9}$$

In the above equations, q is the electronic charge, k is the Boltzmann constant, h is the Planck constant, ϵ_s is the dielectric constant of the material, T is the temperature in Kelvin, and V is the applied voltage. Also, ξ is defined as the difference between the Fermi level and the conduction band in the neutral bulk material for an n-type semiconductor ($\xi \equiv E_c - E_F$), or the valence band in the neutral bulk material for a p-type semiconductor ($\xi \equiv E_F - E_v$).

At low doping levels or high temperatures, thermionic emission dominates and the current density is given by

$$J_T = J_{OT}[\exp(qV/kT) - 1] \tag{3.10}$$

where

$$J_{OT} = A^{*}T^{2}\exp(-q\phi_B/kT) \tag{3.11}$$

In between these two regions, at moderate temperatures and doping levels, thermionic-field emission is prevalent. In this case, the current density is given by

$$J_{TF} = J_{OTF}\exp[qV/E_{oo}\coth(E_{oo}/kT)] \tag{3.12}$$

where

$$J_{OTF}=\frac{A^{*}T\sqrt{[\pi E_{oo}q(\phi_B-V-\xi)]}}{k\cosh(E_{oo}/kT)}\exp[-\frac{q\xi}{kT}-\frac{q}{E_{oo}\coth(E_{oo}/kT)}(\phi_B-\xi)] \tag{3.13}$$

From these current density expressions, the specific contact resistance, R_c, at the barriers is defined as

$$R_c\equiv(\partial V/\partial J)_{V=0} \tag{3.14}$$

So using each of the three cases above, the following expressions can be obtained:

$$R_{c,F}=\frac{1}{\frac{A^{*}T\pi q}{k\sin(\pi kTC_1)}\exp(-q\phi_B/E_{oo})-\frac{A^{*}q}{C_1k^2}\exp[-(q\phi_B/E_{oo})+C_1q\xi]} \tag{3.15}$$

$$R_{c,T}=\frac{k}{qA^{*}T}\exp(q\phi_B/kT) \tag{3.16}$$

$$R_{c,TF}=\frac{k^2\cosh(E_{oo}/kT)}{qA^{*}\sqrt{\pi E_{oo}q(\phi_B-\xi)}}\exp[\frac{q\xi}{kT}+\frac{q(\phi_B-\xi)}{E_{oo}\coth(E_{oo}/kT)}]\sqrt{\coth(E_{oo}/kT)} \tag{3.17}$$

Here, the subscripts F, T, and TF indicate the transport mechanisms of field, thermionic, and thermionic-field emission, respectively. Due to the fact that R_c is defined at zero bias, the above equations are independent of the direction of current flow across the junction.

3.2.2 Calculation of DBR Series Resistance

Now that all of the necessary contact resistance expressions have been obtained, the theoretical series resistance of the DBRs may be calculated. Complete copies of the Mathcad programs used for these calculations are given in Appendix C. The first part of the appendix gives the straight forward bulk layer specific contact resistance calculations for both the low band offset DBRs and the control sample DBRs. The latter sections of the appendix provide calculations for the contact resistance due to the barriers in all four DBR cases. Table 3.3 summarizes the calculated specific contact resistance data.

It is important to note that the Schottky contact model was not blindly applied to the DBR junctions. Before performing the specific contact resistance calculations, the heterojunction energy band diagrams were calculated at equilibrium using a semiconductor device simulation software tool called SimWindows [9]. Using SimWindows, an optoelectronic semiconductor device or structure can be defined and simulated. The calculations solve the appropriate semiconductor electrostatic relations in one dimension. Specially formatted material data files supply SimWindows with the semiconductor parameters necessary to perform the calculations. Sections of the material data file describing the AlGaAs and AlGaInP alloys used in this project are given in Appendix D. The intrinsic band offsets calculated earlier in this chapter were incorporated into this material data file. Device files were created to describe the physical characteristics of each of the four DBRs under investigation. These characteristics included layer dimensions, materials, and doping levels, which were assumed to be $2\times10^{18}\,cm^{-3}$ for both n-type and p-type DBRs. Since one DBR period simply repeats itself through the structure, the device

files only included one period plus a GaAs layer on either side to simulate the substrate. SimWindows then calculated the thermal equilibrium carrier distribution and energy band structure of the DBRs.

Figure 3.10(a) shows the energy band diagram calculated by SimWindows for the n-type AlAs/AlGaInP system. Figure 3.10(b) shows an enlargement of the AlAs/AlGaInP heterojunction conduction band, which does not have a triangular shaped barrier as assumed in the Schottky model. Instead the barrier is a simple step, from the lower edge of the conduction band in the AlGaInP up to the conduction band in the AlAs, with a height, ϕ_B, of 51 meV. Thus for the specific contact resistance calculations for this n-type DBR, the electron transport mechanism was chosen to be thermionic emission. Due to the method by which the thermionic emission current density, J_T in Equation (3.10), is derived, the corresponding specific contact resistance, $R_{c,T}$, is valid for current flow across the junction in either direction. In addition, since the structure of the DBR starts with a quaternary layer on top and ends with a quaternary layer next to the substrate, the AlGaInP/GaAs junction resistance is important because the current must leave the bottom of the DBR through the GaAs substrate. From the enlargement of this junction in Figure 3.10(c), the barrier to electron transport from the AlGaInP to the GaAs is triangular shaped. The barrier height, ϕ_B, from the Fermi level in the GaAs to the peak of the conduction band barrier in the AlGaInP, is 130 meV. This value was used in the thermionic-field transport expression to calculate the contribution to the specific contact resistance due to the AlGaInP/GaAs barrier. The specific contact resistances at each barrier were added together to obtain the total barrier contribution to the resistance, and this total is included in Table 3.3.

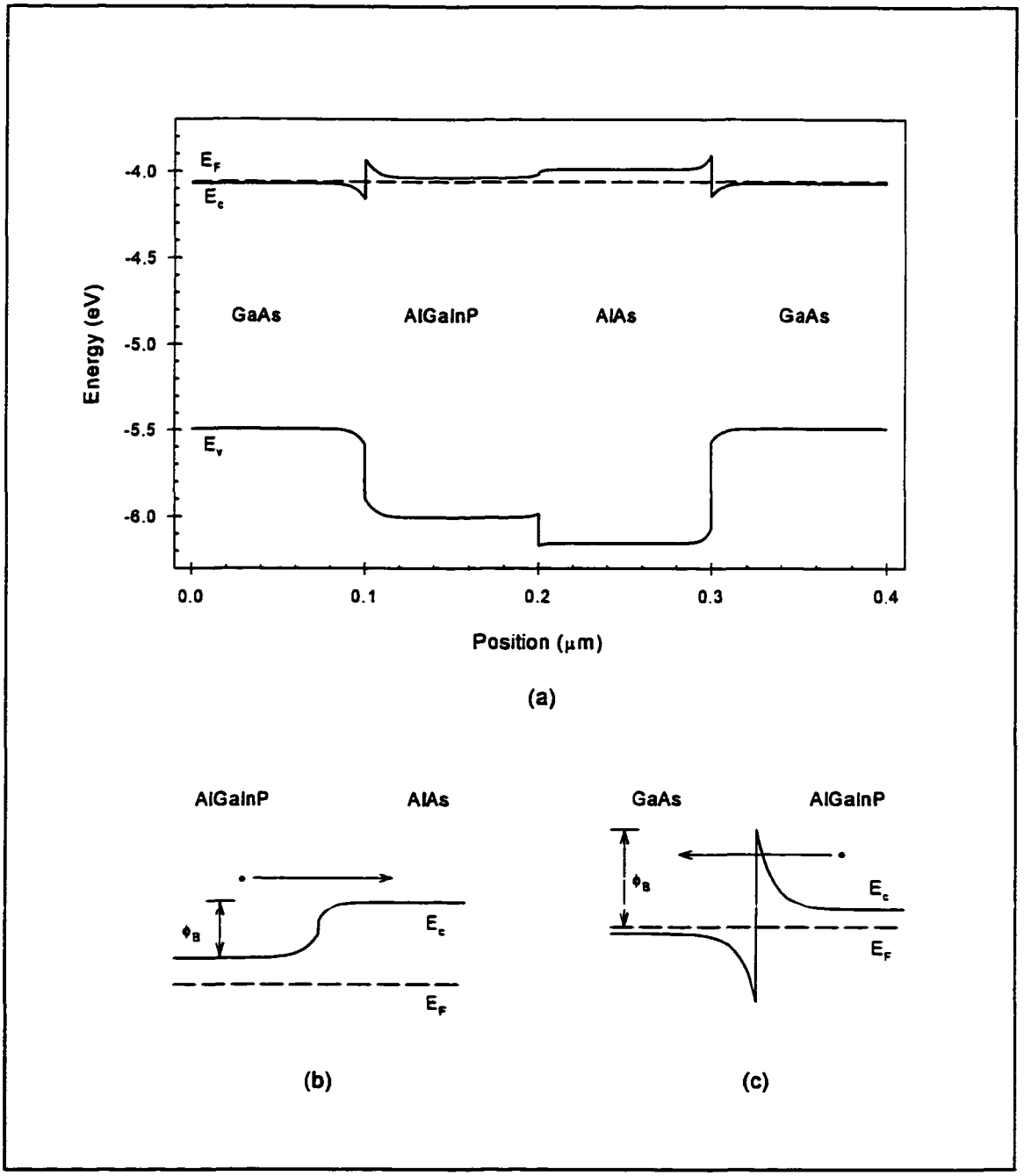

Figure 3.10 SimWindows calculation of the n-type AlAs/AlGaInP(xQ=0.10) heterojunction for the low conduction band offset DBR. (a) The complete band diagram. (b) Close up of the electron transport across the AlAs/AlGaInP junction, which has a step barrier height of ϕ_B= 51 meV. (c) Close up of the electron transport across the AlGaInP/GaAs junction, which has a triangular barrier of height ϕ_B=130 meV.

SimWindows calculations of the DBR energy bands were also carried out for each of the other three DBR structures. The complete band diagrams for the n-type AlInP/AlGaInP, p-type AlGaAs/AlGaInP, and p-type AlInP/AlGaInP heterojunctions are given in Figures 3.11, 3.12, and 3.13, respectively. From these SimWindows calculations, the transport mechanisms and barrier heights were determined for every DBR junction, and for the junctions from the DBR to the GaAs substrate. The barrier height values were used in the appropriate specific contact resistance expressions, depending upon the type of barrier, and the total barrier resistances were calculated. The details of the barrier resistance calculations are included in Appendix C, and the values are summarized in Table 3.3.

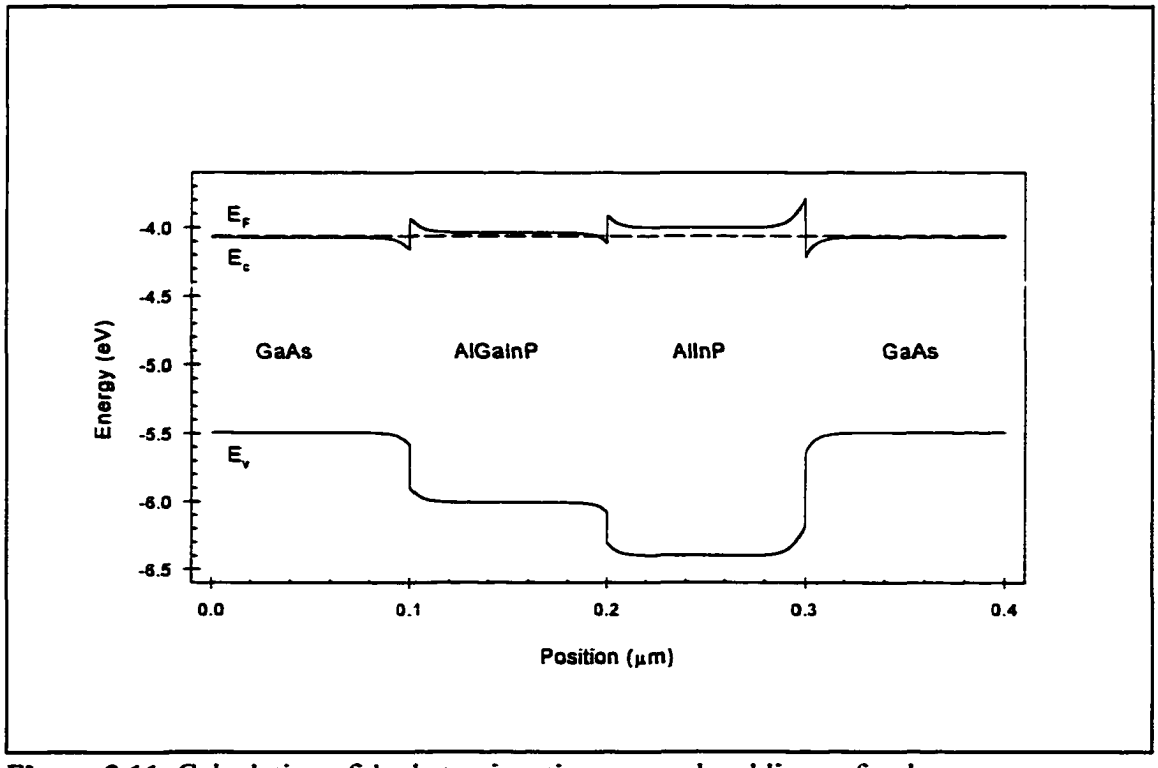

Figure 3.11 Calculation of the heterojunction energy band lineup for the n-type AlInP(xQ=0.52)/AlGaInP(xQ=0.10) control DBR sample.

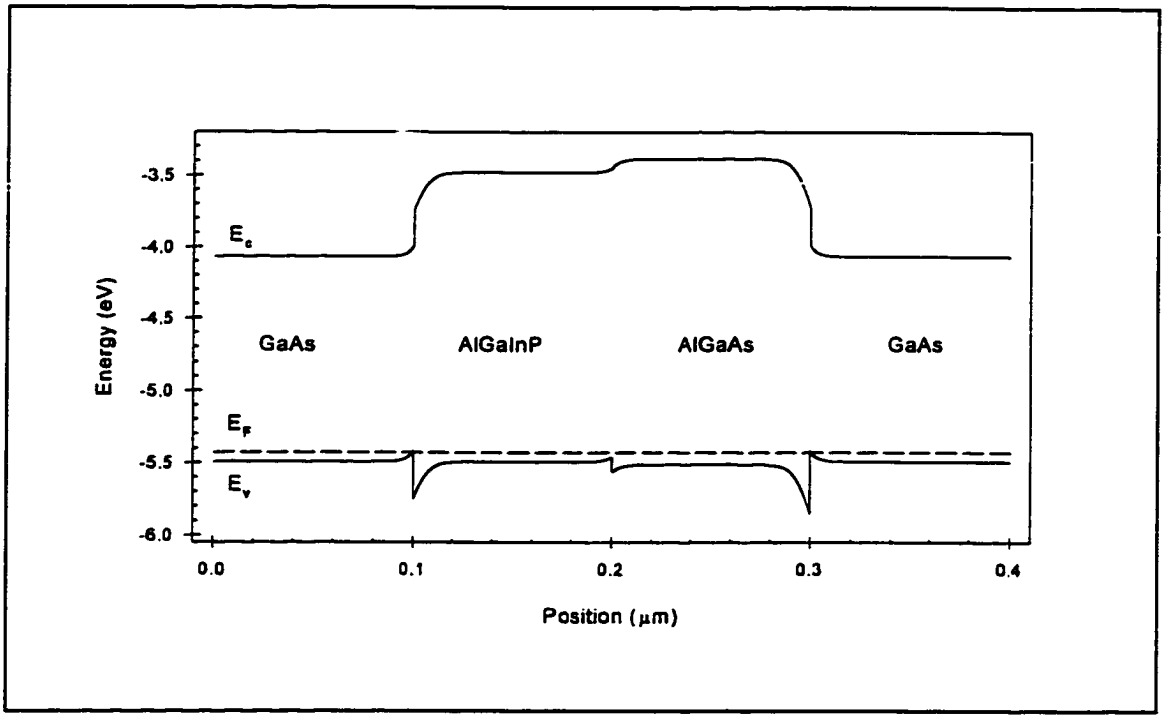

Figure 3.12 Calculation of the p-type AlGaAs(xT=0.9)/AlGaInP(xQ=0.14) heterojunction energy band lineup for the low valence band offset DBR.

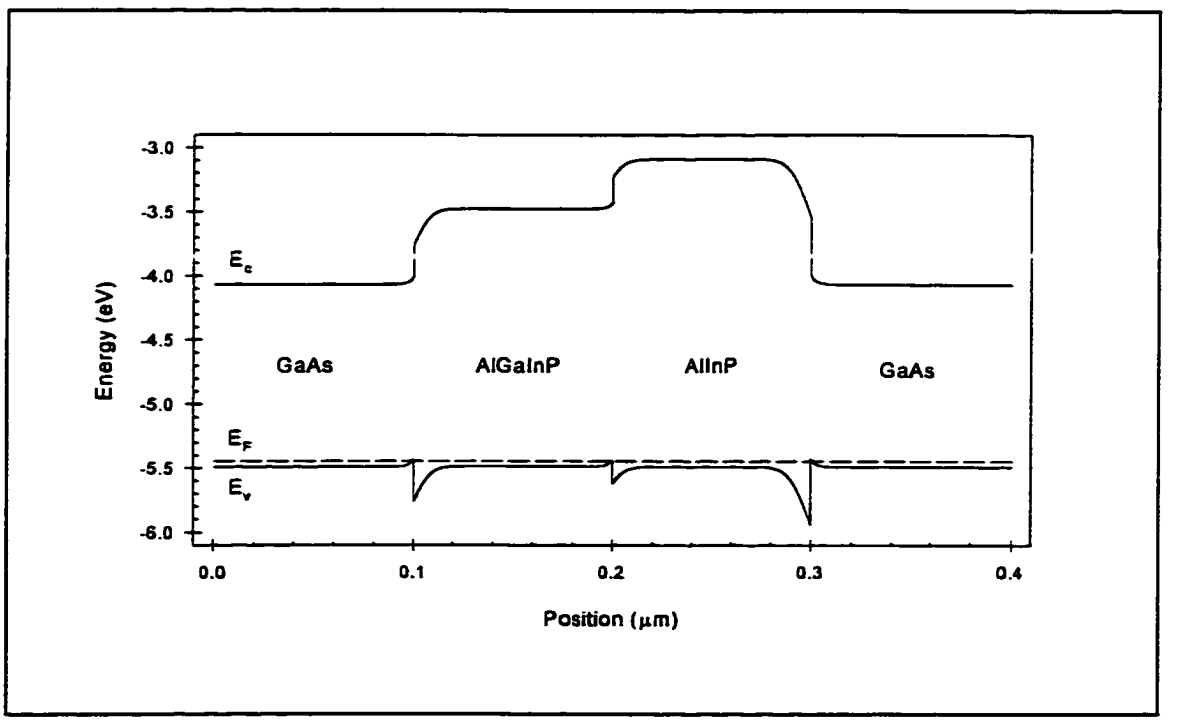

Figure 3.13 Calculation of the heterojunction energy band lineup for the p-type AlInP(xQ=0.52)/AlGaInP(xQ=0.14) control DBR.

3.2.3 Summary of DBR Resistance Calculations

Table 3.3 provides a summary of the specific contact resistance calculations for the four DBR systems. All four DBRs consisted of 40.5 mirror periods, starting at the top with a quaternary layer, alternating with the ternary layers, and ending at the bottom with a quaternary layer next to the substrate. The extra half period quarter wavelength layer at the bottom of the DBR stack helped reduce the barrier resistance from the DBR into the GaAs substrate since the AlGaInP/GaAs junction has a small barrier than the AlGaAs/GaAs or the AlInP/GaAs junctions. From the data, it is obvious that most of the series resistance in the DBRs is due to the barriers at the heterojunctions, as expected.

One thing not clear from the table is the distribution of the barrier resistances. From the band diagrams in Figures 3.10 through 3.13, the barrier height from the DBR materials into the GaAs is larger than between the DBR materials themselves. For the low band offset and control n-type DBRs, the single AlGaInP(xQ=0.10)/GaAs junction contributes only 3% and 0.5%, respectively, to the total barrier resistance. On the other hand, in the p-DBRs the mirror/substrate barrier is a significant part of the total barrier resistance. For the low valence band offset and control DBRs the AlGaInP(xQ=0.14)/GaAs barrier contributes 83% and 50%, respectively, to the total resistance. However, if the extra quaternary layers were not included at the bottom of the mirror stack, the contribution of the ternary/substrate barrier would be an even higher percentage of the total specific contact resistance. As far as a visible VCSEL application would be concerned, though, no GaAs would be present in the structure since GaAs absorbs light in the visible spectrum, and thus the large contribution from the p-type AlGaInP/GaAs interface would not exist.

Returning to Table 3.3, the Al(Ga)As/AlGaInP material systems show a lower total specific contact resistance than the AlInP/AlGaInP control DBR systems. The n-type is lowered by a factor of six, while the p-type is lowered only by a factor less than two. This is directly due to the lower band offsets in the Al(Ga)As/AlGaInP material systems. In fact, a careful examination of the data shows that the bulk resistance values of the Al(Ga)As/AlGaInP structures are actually larger than those of the AlInP/AlGaInP ones, due to the smaller mobility of carriers in the high aluminum content AlGaAs compared to the InAlP. However, the smaller AlGaAs/AlGaInP band offsets more than make up for this increased bulk resistance by lowering the resistance due to the barrier. Thus the use of the small band offset materials in the DBR structures has the desired effect of lowering the overall series resistance.

Table 3.3 Summary of specific contact resistance calculations for the four DBRs, each consisting of 40.5 mirror periods.

DBR Materials	Composition	Type	Rc ($\Omega \cdot cm^2$)		
			Bulk	Barrier	Total
AlGaAs/AlGaInP (low offset DBR)	xT=0.90/xQ=0.14	p	5.34×10^{-6}	2.30×10^{-4}	2.35×10^{-4}
AlInP/AlGaInP (control sample)	xQ=0.52/0.14	p	4.05×10^{-6}	3.81×10^{-4}	3.85×10^{-4}
AlAs/AlGaInP (low offset DBR)	xQ=0.10	n	9.50×10^{-7}	1.10×10^{-5}	1.20×10^{-5}
AlInP/AlGaInP (control sample)	xQ=0.52/0.10	n	6.30×10^{-7}	7.46×10^{-5}	7.53×10^{-5}

REFERENCES: CHAPTER III

[1] M. Krijn, "Heterojunction band offsets and effective masses in III-V quaternary alloys," *Semicond. Sci. Technol.* **6**, 27 (1991).

[2] C. Van de Walle, "Band lineups and deformation potentials in the model-solid theory," *Phys. Rev. B* **39**, 1871 (1989).

[3] S. Adachi, "GaAs, AlAs, and $Al_xGa_{1-x}As$: Material parameters for use in research and device applications," *J. Appl. Phys.* **58**, R1 (1985).

[4] D. Aspnes, S. Kelso, R. Logan, and R. Bhat, "Optical properties of $Al_xGa_{1-x}As$," *J. Appl. Phys.* **60**, 754 (1986).

[5] H. Tanaka, Y. Kawamura, and H. Asahi, "Refractive indices of $In_{0.49}Ga_{0.51-x}Al_xP$ lattice matched to GaAs," *J. Appl. Phys.* **59**, 985 (1986).

[6] R. Schneider, Jr. and J. Lott, "InAlP/InAlGaP distributed Bragg reflectors for visible vertical cavity surface emitting lasers," *Appl. Phys. Lett.* **62**, 2748 (1993).

[7] H. Sugawara, K. Itaya, H. Nozaki, and G. Hatakoshi, "High-brightness InGaAlP green light-emitting diodes," *Appl. Phys. Lett.* **61**, 1775 (1992).

[8] G. Robinson, "Schottky Diodes and Ohmic Contacts for the III-V Semiconductors," in Physics and Chemistry of III-V Compound Semiconductor Interfaces, edited by C. Wilmsen; Plenum Press: New York, 1985.

[9] SimWindows, Version 1.3.0; copyright by D. Winston, Optoelectronics Computing Systems Center, University of Colorado at Boulder, 1995.

CHAPTER IV

EXPERIMENTAL PROCEDURES

This chapter describes the experimental equipment and procedures used in this research project. The first section describes the Gas Source Molecular Beam Epitaxy growth of the semiconductors studied in this work. This includes a brief discussion of MBE fundamentals, CSU MBE system specifications, and growth procedures. The middle of the chapter describes three characterization methods used to analyze the quality of the epitaxial samples. This involves discussion of system setup and measurement procedures for double crystal x-ray diffraction, Hall-van der Pauw, and reflectance measurements. The last section of this chapter describes the transmission line model (TLM) measurements used to determine the resistances of the DBRs. This includes discussions on TLM theory, fabrication of the test structures, and the current-voltage measurements for resistance determination.

4.1 Gas Source Molecular Beam Epitaxy

All of the semiconductor alloys studied in this dissertation were grown using Gas Source Molecular Beam Epitaxy (GSMBE). Epitaxial growth in MBE occurs when thin films crystallize via the reaction between impinging molecular or atomic beams and a crystalline substrate which is maintained at an elevated temperature in an ultrahigh vacuum

(UHV) environment. The source materials arrive at the substrate via molecular flow, rather than viscous or diffusive flow, because their mean free path in the UHV environment is much larger than the size of the growth chamber. Epitaxy implies that the growing layer derives its crystal orientation from that of the substrate material. Conventional MBE for growth of III-V semiconductors uses solid sources evaporated in effusion cells to produce the molecular beams. GSMBE is a variation of MBE where the group V materials are obtained from injected gases and solid sources are used for group III materials.

A main advantage of MBE is the ability to grow complicated heterostructures with abrupt interfaces and with monolayer thickness control due to the precise control of growth conditions. Typical growth rates of 1.0 μm/hr allow for surface migration of the impinging species, resulting in layer by layer growth and very smooth surfaces. Mechanical shutters between the molecular beam sources and the substrate provide near instantaneous interruption of the beam fluxes, thus controlling layer thicknesses to the atomic scale. Composition and doping of the epitaxial films depend on the relative arrival rates of the constituent elements. Under typical growth conditions the substrate temperature is less than the vapor pressure of the group III elements, and the III/V material flux ratio is less than unity, so that the composition and growth rate of the epitaxial film is dictated by the fluxes coming from the group III effusion cells. Then, using the $Al_xGa_yIn_{1-x-y}P$ material of this work as an example and assuming unity sticking coefficients for the group III elements, the composition, that is the mole fractions x and y, is related to the fluxes F_{Al}, F_{Ga}, and F_{In} by

$$x = \frac{F_{Al}}{F_{Al} + F_{Ga} + F_{In}} \tag{4.1}$$

$$y = \frac{F_{Ga}}{F_{Al} + F_{Ga} + F_{In}} \tag{4.2}$$

The fluxes are in turn controlled by the effusion cell temperatures. In a similar manner, the doping levels are controlled by the flux levels from those effusion cells. Other advantages of MBE include the atomically clean surfaces available in the UHV environment and the availability of *in situ* surface monitoring and characterization techniques, such as reflection high energy electron diffraction (RHEED).

The above information is only intended to be a reminder of the properties of MBE. There are numerous references which provide more in-depth details on both MBE technology [1] and the materials science fundamentals that apply to MBE [2], as well as descriptions of GSMBE in particular [3]. These are only a sampling of what may be found in the literature.

A Perkin-Elmer 430 MBE system, modified for the use of hydride gas sources, was used to grow all of the samples in this dissertation. This GSMBE system consisted of the UHV growth chamber, an intro-chamber with a load lock used to introduce samples into the vacuum and transfer them into the growth chamber, and a gas cabinet for safely handling the hydride gas and delivering it into the growth chamber. The system also included a control console with power supplies and a Research Inc. Micricon 823 process controller which was remotely computer programmed. Through this the operator controlled the effusion cell

temperatures and shutters, the gas cabinet pneumatic valves and gas flow into the growth chamber, and the substrate temperature. Details of the GSMBE system can be found in [3].

Figure 4.1 shows a schematic representation of the GSMBE growth chamber. Conventional effusion cells provided the molecular beams of the group III aluminum, gallium, and indium materials. Group V molecular beams of As_2 and P_2 were obtained by flowing ultrapure arsine (AsH_3) and phosphine (PH_3) gases into the growth chamber through a tantalum gas cracker heated to 800°C. The by-product of this thermal hydride dissociation, H_2, was pumped from the system by a Cryo-Torr 8 high vacuum pump from CTI Cryogenics. Liquid nitrogen cooled cryogenic shrouds were also used for added pumping of the growth chamber. Typical chamber pressures during growth were 1×10^{-5} to 1×10^{-4} torr, depending

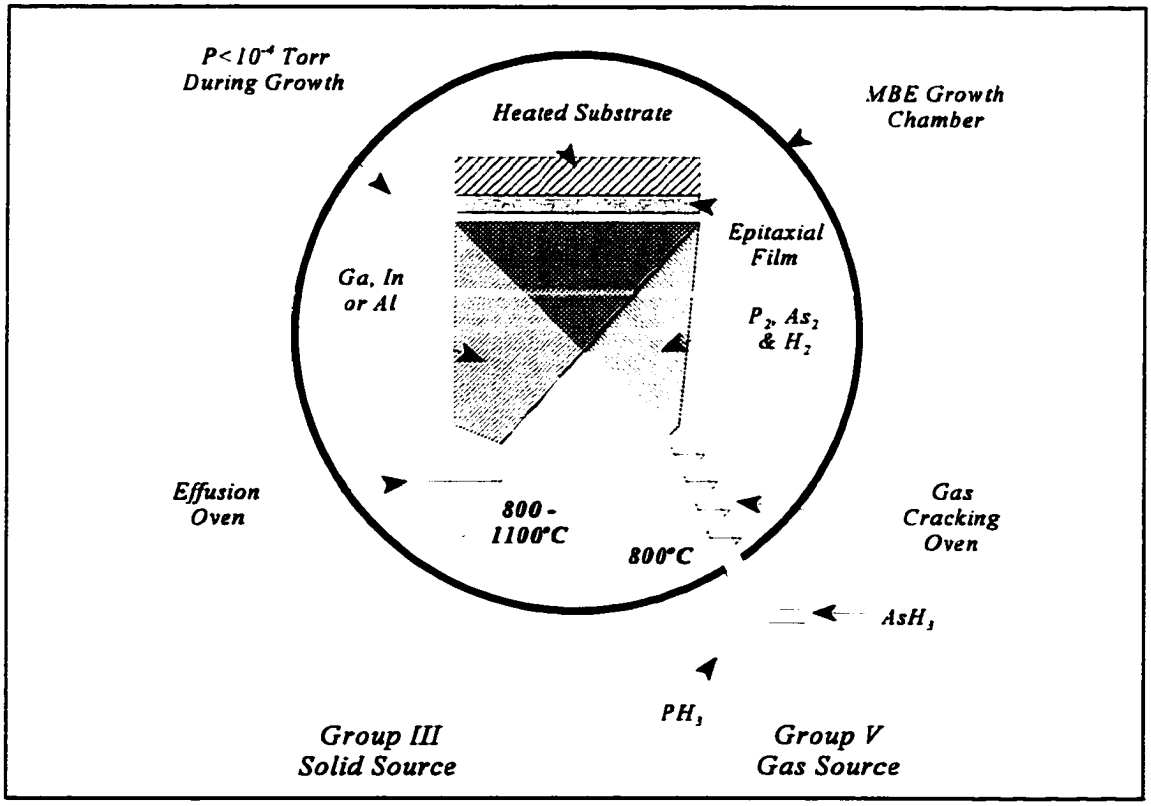

Figure 4.1 Schematic diagram of the CSU GSMBE growth chamber.

on the amount of gas flow. A tantalum coil radiative heater behind the sample was used to maintain the substrate temperature between 500°C and 650°C, as measured by a thermocouple in contact with the molybdenum block on which the substrate was mounted. Pneumatically controlled shutters were used to select which atomic fluxes reached the substrate. The source flange on the growth chamber was equipped with eight source ports, seven holding effusion cells and one for the gas cracker. Figure 4.2 shows the source flange configuration along with a description of each source cell. The small beryllium and silicon

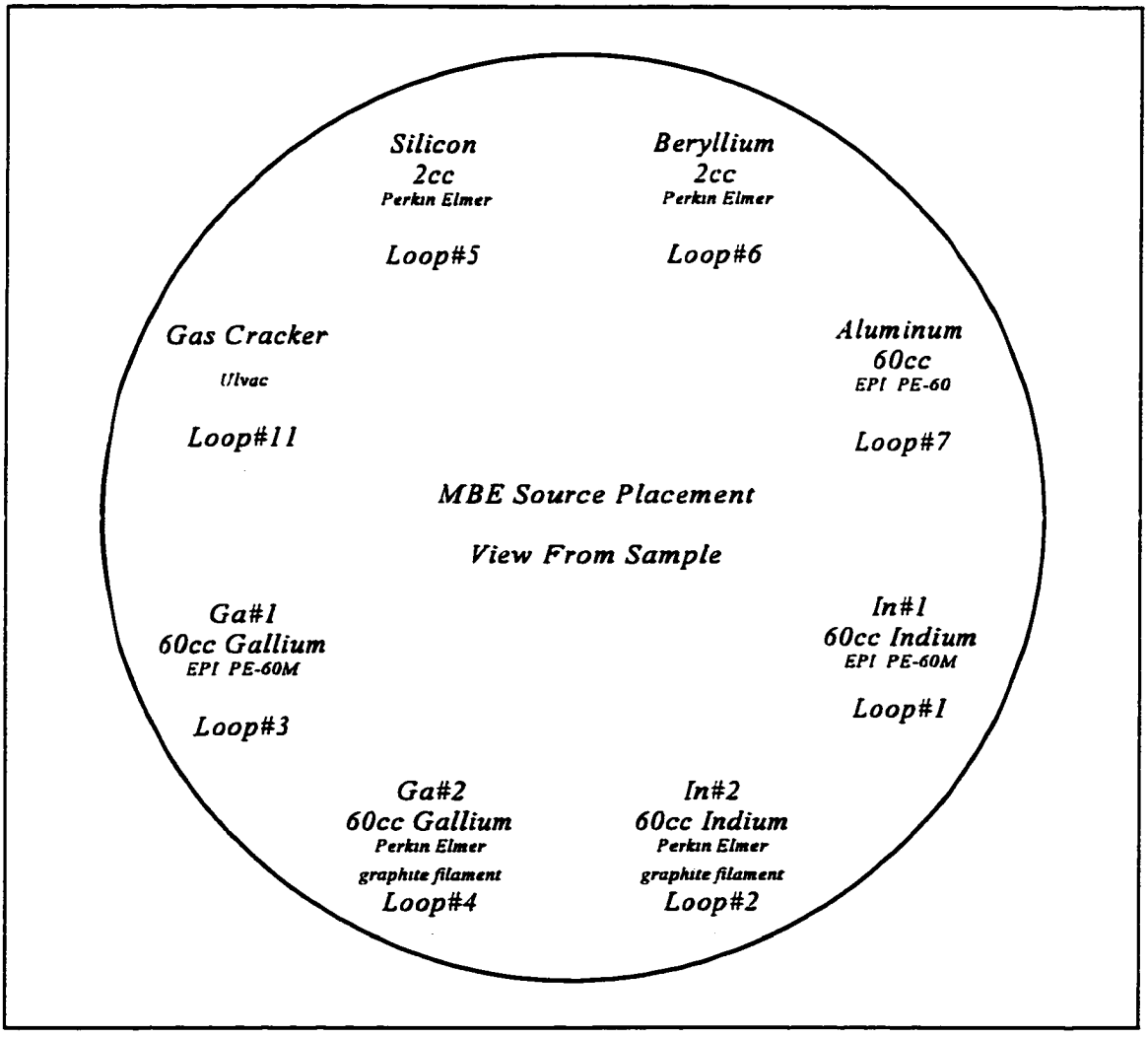

Figure 4.2 Configuration of source cells on the GSMBE growth chamber source flange.

effusion cells were used for p-type and n-type doping, respectively. The source flange was cooled by flowing water through a shroud surrounding the cells.

All of the samples in this work were grown on (100) GaAs substrates whose surfaces were prepared for growth using standard techniques. First, the surface was degreased via successive soakings in trichloroethylene, acetone, methanol, and deionized water (DI-H_2O). The sample was then etched for 2 minutes in a 2:1:10 mixture of ammonium hydroxide (NH_4OH):hydrogen peroxide (H_2O_2):DI-H_2O to expose a clean, fresh surface. A native oxide layer was then formed on this clean surface by flushing the sample with running DI-H_2O for 2 minutes and soaking the sample in DI-H_2O for 10 minutes. Finally, the sample was blown dry with nitrogen gas and mounted on a molybdenum block with indium solder. A shadow wire was stretched across the sample to allow for thickness measurements after growth, and the sample blocks were loaded into the intro chamber for storage under vacuum until growth.

Every MBE growth sequence began with the desorption of the native oxide layer formed on the substrate during sample preparation. Desorption was achieved by heating the substrate in the growth chamber under an over-pressure of arsenic. Successful desorption was determined by RHEED, where an atomically clean (i.e. no oxide layer present) GaAs surface is indicated by a specific pattern. Details for using RHEED in MBE applications can be found in most texts on MBE [1, 2] and in a good review of the subject [4]. The measured thermocouple temperature for desorption of the GaAs native oxide was found to be around 625°C. Due to the reliability and repeatability of the technique, a standard procedure was established for desorption. Before starting the desorption sequence, which is shown schematically in Figure 4.3, the effusion cells were out gassed for one hour at a temperature

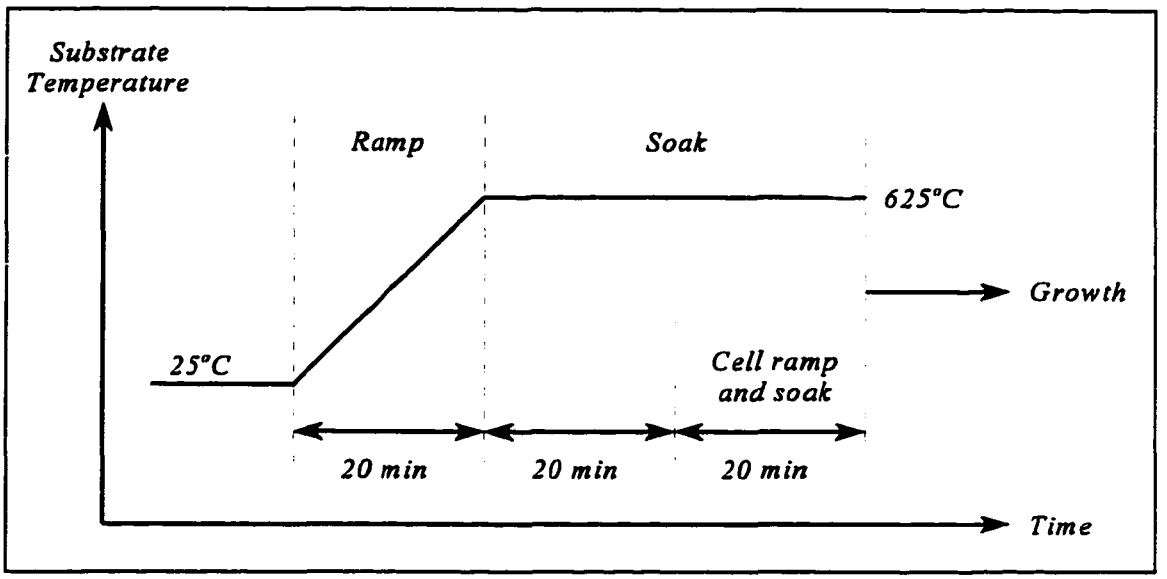

Figure 4.3 GaAs native oxide desorption sequence prior to epitaxial growth.

50°C above that used for growth, and were then left at idling temperatures of 600°C or 750°C, depending on the material. The 60 minute desorption sequence included a 20 minute substrate ramp from 25°C to 625°C, and a 40 minute soak, all under an arsenic over-pressure. During the last half of the desorption soak, the source effusion cells were ramped from their idling to their growth temperatures in 10 minutes, and then were soaked for 10 minutes to provide stable fluxes for growth. Epitaxial growth was started immediately after the desorption sequence finished.

Two basic types of samples were grown for this work, bulk epitaxial layers and distributed Bragg reflectors (DBRs). This section will conclude with a description of the growth sequences used for each type of sample.

Figure 4.4 shows a typical epitaxial layer structure for a bulk, n-type, AlGaInP quaternary (n-Q) sample. Structures of this form were used to calibrate the doping and composition, ranging from one end point ternary to the other (AlInP to GaInP), of the bulk

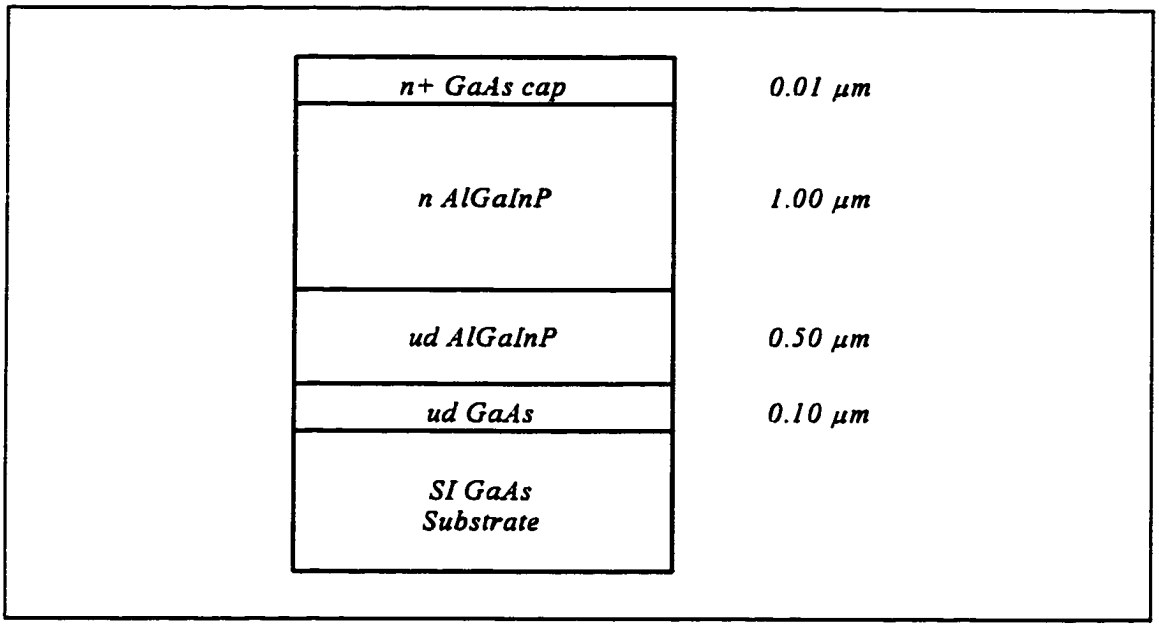

Figure 4.4 Epitaxial layer structure of a bulk, n-type AlGaInP calibration sample.

layers. All calibration samples were grown on semi-insulating GaAs (100) substrates. The first layer grown was an unintentionally doped (ud) GaAs buffer. The purpose of this buffer was to ensure a smooth epitaxial surface for the layers above it, and to provide time for the substrate temperature to ramp down from its desorption temperature to a temperature better suited for growth of high quality quaternary layers. This substrate ramp can be seen in Figure 4.5, which shows temperature changes for the substrate and each cell throughout the growth of the bulk layers. The figure starts during the desorption and goes through the cool down of the substrate. The next two layers were an ud-AlGaInP (ud-Q) layer followed by a n-type one. The purpose of the ud-Q layer was to make sure the carriers were confined in the n-type layer, so an accurate electrical measurement of the carrier concentration could be made. The final layer was a highly doped GaAs cap layer, which served as a contact layer for making metal contacts to the whole structure. The effusion cell temperature ramps for

this structure were fairly straight forward, with only the Si cell changing during the growth. Figure 4.5 also indicates which cells had their shutters open during each epitaxial layer.

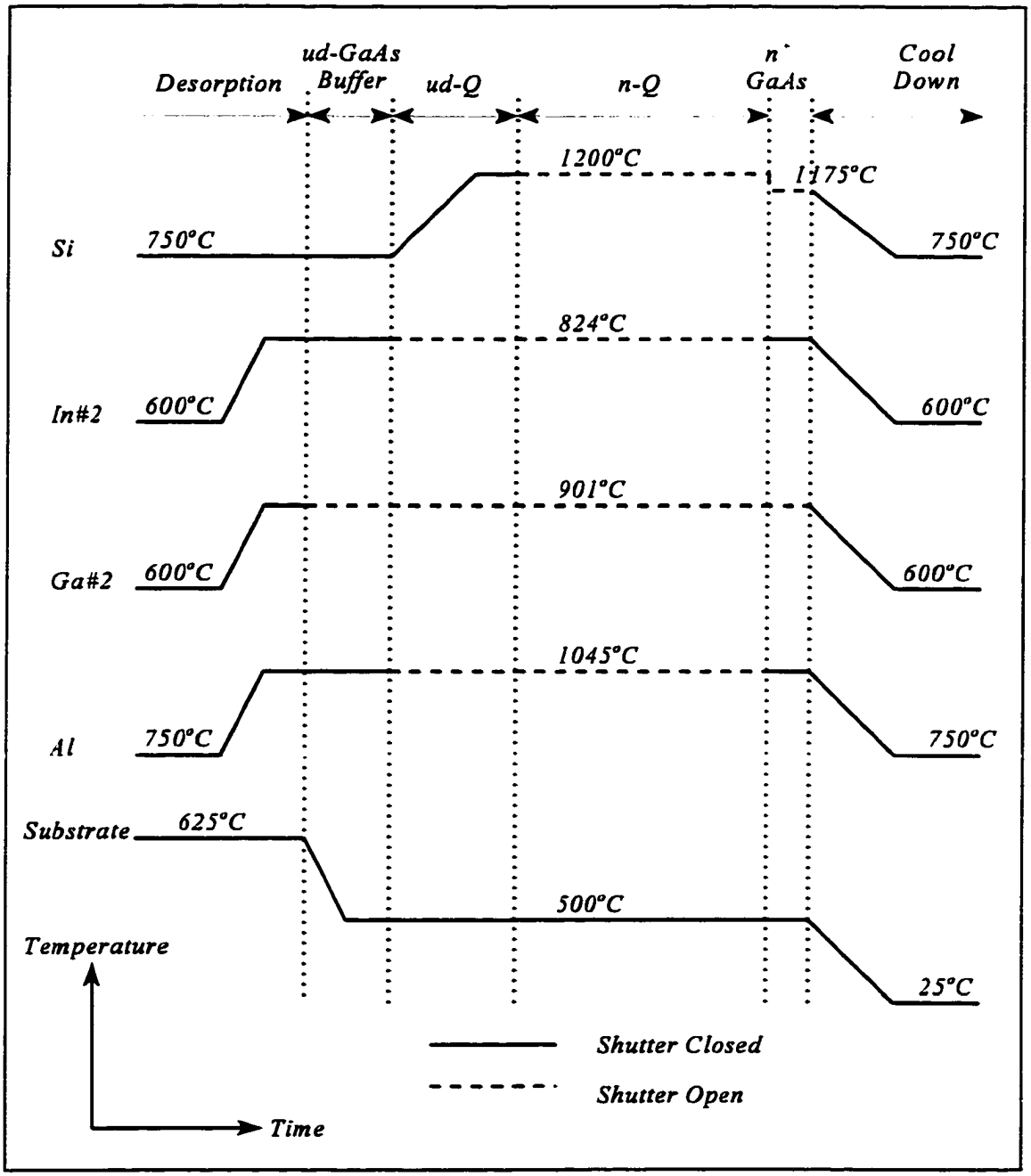

Figure 4.5 Typical substrate and effusion cell ramps used for bulk epitaxial layers.

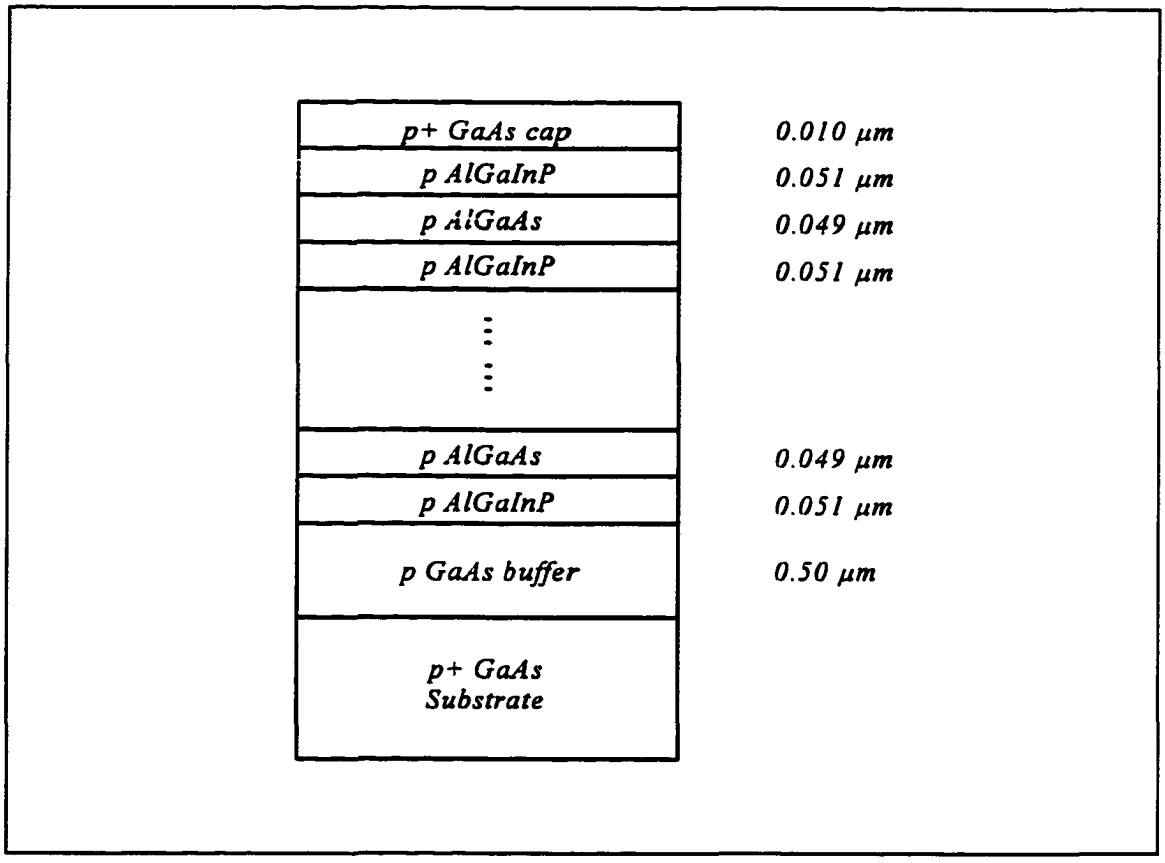

Figure 4.6 Epitaxial layer structure of a p-type DBR.

AlGaAs calibration samples had the same basic structure as AlGaInP ones, except for the addition of an ud-InGaP between the doped AlGaAs bulk layer and the doped GaAs cap. After making metal contact to the structure, the GaAs cap would be etched so that it would not affect the measurement of the AlGaAs layer. So the InGaP served as an etch-stop layer and to confine carriers in the AlGaAs.

Figure 4.6 shows a typical epitaxial layer structure for a p-type distributed Bragg reflector (DBR). All of the doped DBRs were grown on conducting substrates of the same type as the epitaxial materials, in this case p-type. A p-type GaAs buffer layer was grown first to ensure a smooth epitaxial surface and to allow time for the substrate temperature to

ramp down to the temperature needed to grow the DBR. Then the DBR was constructed by the growth of alternating AlGaInP and AlGaAs p-type epitaxial layers. Also as before, a highly doped GaAs cap layer was used to obtain a better ohmic contact. The generic structure shown consists of m+½ periods, where m is an integer. The number of periods actually grown depended on the desired reflectance of the mirror. The DBR was initiated and terminated with a quaternary layer to provide lower conductive barriers with the GaAs layers on either side, thus giving a smaller resistance.

Temperature ramp schemes for the effusion cells and the substrate, Figure 4.7, are shown for a generic m+½ period DBR. Due to the fact that Al was used in both layers and at different cell temperatures, the DBR ramping scheme was more complicated than that of the bulk layers. Note how the Al, Ga#1, and Be cells were all simultaneously ramped down during the growth of the AlGaAs layer. This was needed to give the Al cell three minutes to settle down to 1058°C and thus provide a stable flux necessary to achieve accurate composition control of the quaternary layer. The details of the growth pauses used between DBR layers are not shown in the figure. At the start of each pause the Be cell and either the Al or Ga#1 cell, depending on which layer had just been completed, were ramped in two seconds to the temperature needed for the next layer. Then the growth pause continued for another 30 seconds to let the cell temperatures settle toward their set points, and then the next layer was started. Also, the hydride gas flow into the chamber was switched, as necessary, at the very end of the growth pause. More detailed discussion for the need to ramp the effusion cell temperatures up and down every DBR period is given in Chapter V.

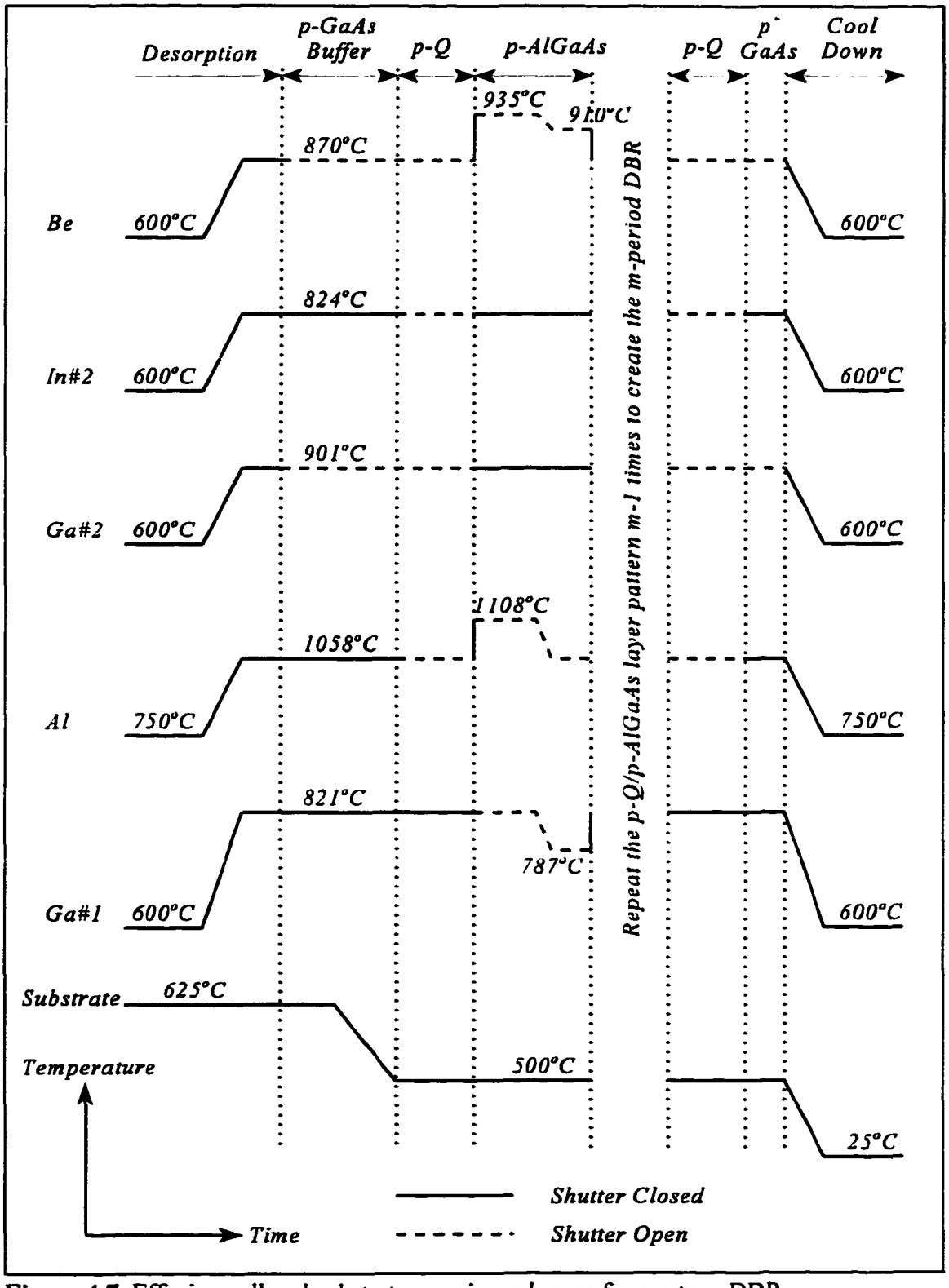

Figure 4.7 Effusion cell and substrate ramping schemes for a p-type DBR.

4.2 Double Crystal X-Ray Diffraction

Double crystal x-ray diffraction (DCXD) provides information on the crystal structure of epitaxial films. DCXD makes use of the scattering of incident x-ray particles by a periodic crystal lattice to measure its lattice constant, thus allowing the alloy composition and possibly the layer thickness of the sample to be determined. Schematically, this can be seen in Figure 4.8 below. X-rays incident upon parallel atomic planes will constructively interfere when the incident angle, θ, satisfies the Bragg condition. For a given atomic spacing of the crystal planes, d, the incident angle of the x-ray radiation is related to the radiation wavelength, λ, and to the order, n, of the reflection by

$$2d\sin\theta = n\lambda \tag{4.3}$$

which is known as the Bragg condition.

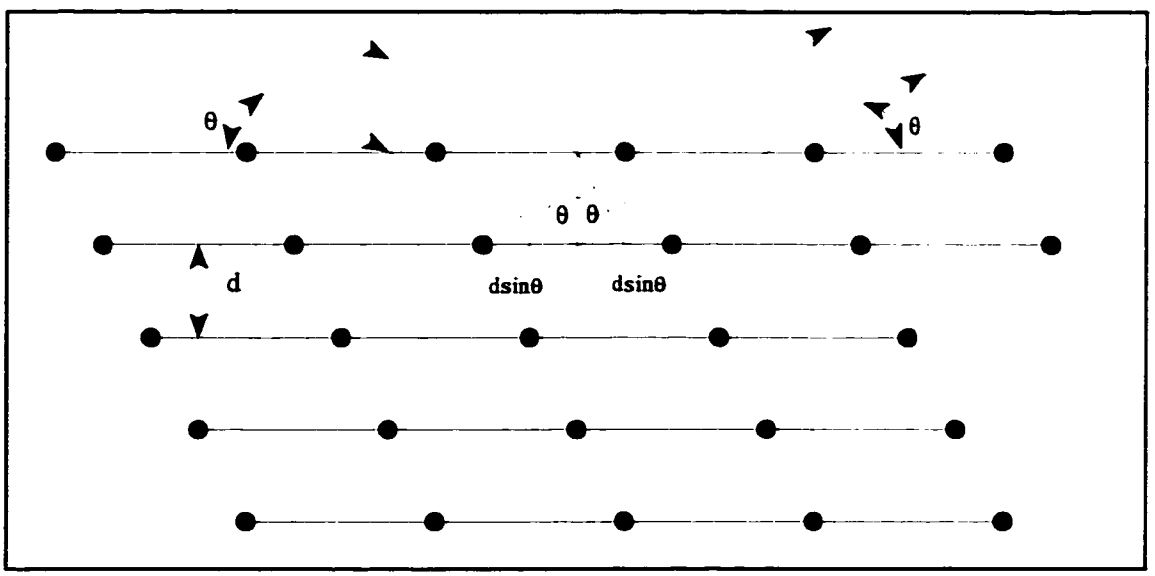

Figure 4.8 Schematic diagram of Bragg diffraction off parallel planes of a lattice.

For the AlGaInP and AlGaAs alloys lattice matched to GaAs used in this work, the Bragg angle is 33.03° for the (400) reflection. This is the most commonly measured reflection for zinc blend lattice structures due to its high intensity. The (400) atomic planes are parallel to the (100) surface and have a separation, d, of one fourth the bulk lattice constant. For GaAs this corresponds to $d=a_{GaAs}/4$ or 1.413 Å.

DCXD rocking curves are generated by scanning θ around the Bragg angle of the substrate. A typical rocking curve is shown in Figure 4.9, with an InGaP alloy epitaxial layer on a GaAs substrate. If the epilayer is grown coherently with the substrate, its lattice constant parallel to the surface is assumed to be identical to that of the substrate. Because

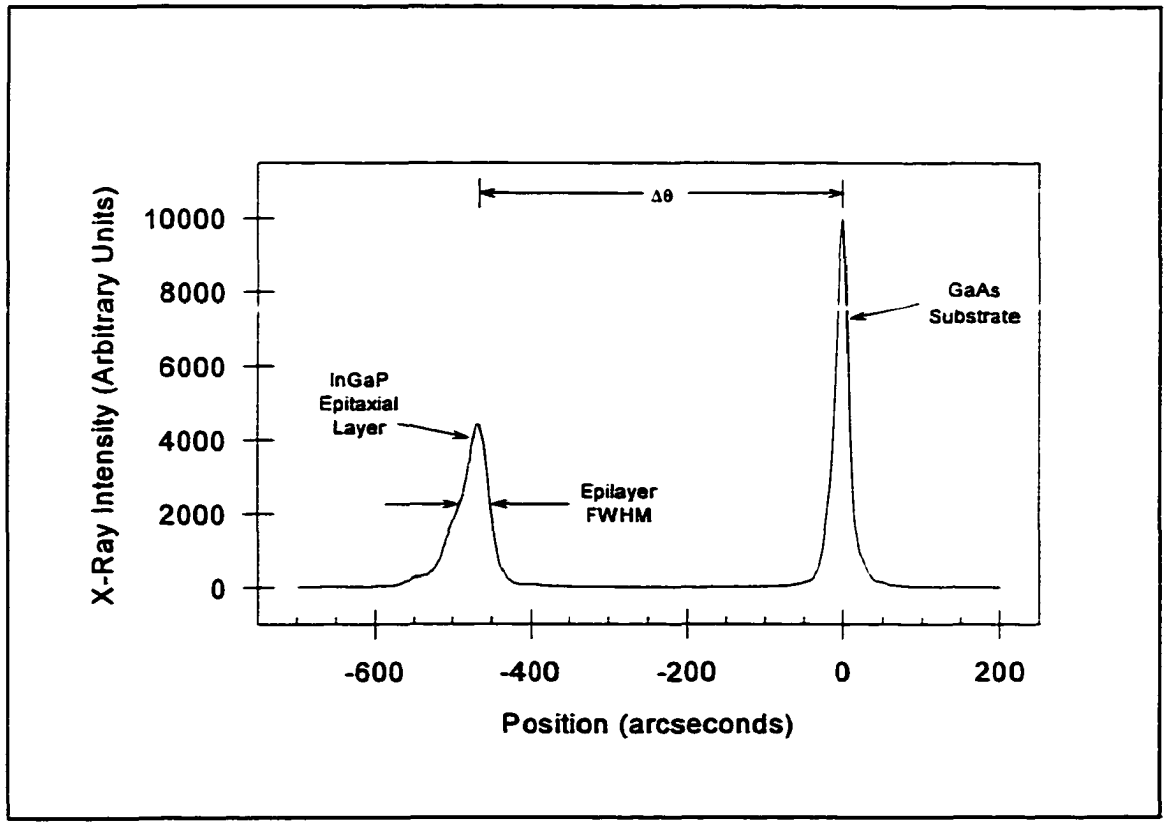

Figure 4.9 Sample x-ray rocking curve for InGaP grown on a GaAs substrate.

the thickness of the epilayer is significantly smaller than that of the substrate, its cubic structure distorts to accommodate any bulk lattice constant mismatch with the substrate. The in-plane and perpendicular lattice constants of the epilayer are no longer identical as the tetragonal distortion preserves the unit cell volume of the crystal. If the bulk lattice constant of the epilayer is larger (smaller) than the substrate, the film will undergo in-plane compression (tension) and the parallel lattice constant will be smaller (larger) than the perpendicular lattice constant [2]. Since DCXD measures the lattice separation perpendicular to the surface, a slightly mismatched, coherent epitaxial layer will have a slightly different Bragg angle than the substrate, and thus two peaks are detected in the rocking curve.

The angular separation between the two peaks, $\Delta\theta = \theta_{film} - \theta_{sub}$, is used to correct for the tetragonal distortion of the film. Using the substrate lattice constant and Bragg angle, the as-measured lattice constant (a^{*}_{epi}), mismatch (m^{*}), and ternary composition (x_{meas}) of the epilayer are obtained. Then Poisson's ratio (ν) is used to correct for the distortion, giving the true mismatch (m), lattice constant (a_{epi}), and composition (x) of the epitaxial film. The equations used to make these corrections are summarized in Table 4.1. In general, the smaller the mismatch between epilayer and substrate, the better the quality of the epitaxial film.

Another qualitative measure of film quality is the full width half maximum (FWHM) of the epilayer peak in the x-ray rocking curve spectrum. Dislocations and localized compositional variations in the crystal broaden the FWHM. So a narrow peak indicates a high quality epitaxial film.

Table 4.1 Equations to calculate mismatch and composition from the measured x-ray peak separation ($\Delta\theta$), and corrections for tetragonal distortion. a_{sub} is the substrate lattice constant, a_1 and a_2 are the end point binary lattice constants of the ternary film, and θ_B is the Bragg angle of the substrate material.

As-Measured Calculation from $\Delta\theta$	
Lattice Constant	$a^*_{epi} = a_{sub}\sin\theta_B/\sin(\theta_B + \Delta\theta)$
Mismatch	$m^* = [a^*_{epi} - a_{sub}]/a_{sub}$
Ternary Composition	$x_{meas} = (a^*_{epi} - a_2)/(a_1 - a_2)$
Corrections for the Tetragonal Distortion	
Poisson's Ratio	$\upsilon = 0.333$
Mismatch	$m = m^*(1 - \upsilon)/(1 + \upsilon)$
Lattice Constant	$a_{epi} = [1 + m]a_{sub}$
Ternary Composition	$x = (a_{epi} - a_2)/(a_1 - a_2)$

X-ray spectra for the superlattice distributed Bragg reflectors studied in this work contain additional features not seen in the spectrum from a bulk sample, which Figure 4.9 demonstrates. In addition to the central epilayer peak, there are also multiple satellite peaks present. These arise due to the periodic nature of the DBR structure, and thus a measure of the angular separation of the satellite peaks can be used to calculate the average DBR period. The shape and number of satellite peaks give a qualitative measure of the quality of the DBR, with the general idea being that narrower peaks and higher numbers of peaks observed indicate a better structure. To obtain more information from a DBR x-ray spectrum requires detailed knowledge of the structure and sophisticated computer simulation software. This

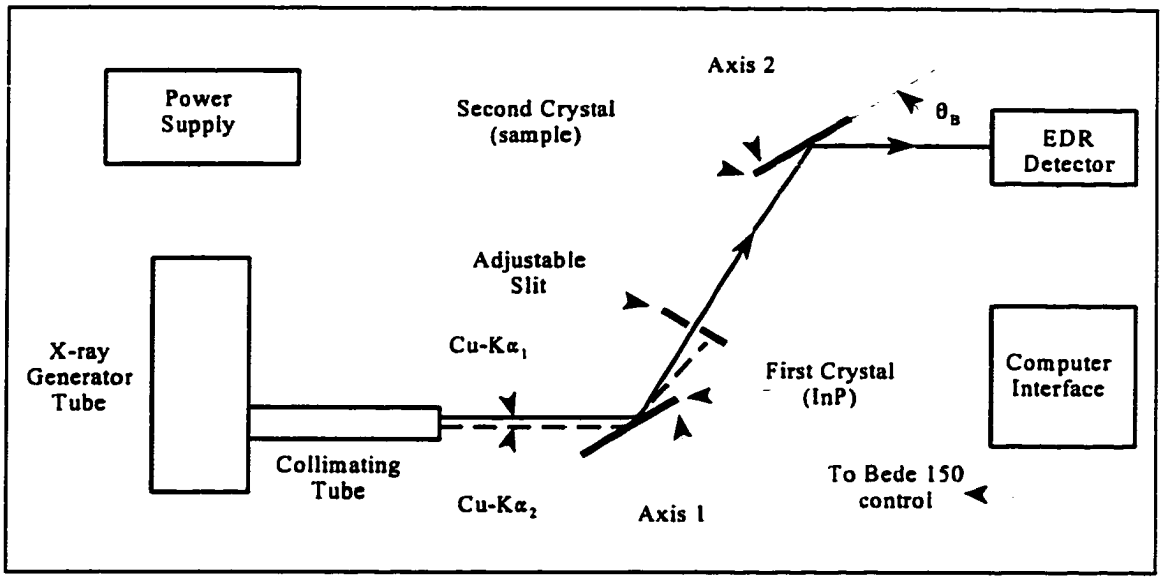

Figure 4.10 Diagram of the DCXD measurement system, where θ_B is the Bragg angle of the x-rays with the measured sample.

allows for comparison of simulated spectra with measured data so that information such as the thicknesses of the individual DBR layers and the possible material mismatches can be extracted.

DCXD measurements in this work were preformed using a Bede Scientific Instruments model 150 double axis diffractometer. Figure 4.10 shows a schematic diagram of the system. A Hiltonbrooks DG2 x-ray generator power supply and an AEG FK 60-04 x-ray tube produced the radiation. The sealed, water cooled tube had a copper anode, generating radiation between 1.39 Å and 1.55 Å, and a beryllium exit window. The radiation traveled down a collimating tube and Cu-Kα_1 and -Kα_2 transition x-rays were focused toward the high quality InP substrate which served as the first crystal. The position of Axis 1 was chosen to match the (400) reflection of the Cu-Kα_1 x-rays off the InP substrate, giving a Bragg angle of 31.67° for the 1.5405 Å radiation. The slightly differing

$K\alpha_1$ and $K\alpha_2$ wavelengths ensured their Bragg angles were not the same, and then the adjustable slit was used to select the stronger $K\alpha_1$ for incidence on the second crystal. X-rays diffracting off the second crystal, which was the sample under investigation, were measured using a Bede Scientific EDR (Enhanced Dynamic Range) Detector. The DCXD measurement system was controlled and data collected via a computer interface.

X-ray rocking curves were generated by mounting the MBE grown sample in the position of the second crystal. For a bulk epitaxial film the power supply was set at 33 kV and 12 mA, or about 400 W, and for the superlattice DBR samples it was set at 35 kV and 15 mA, or about 525 W. The detector was adjusted to be at the expected Bragg angle of the substrate material, 33.03° for GaAs, and Axis 2 was rotated until the substrate peak was detected. A tilt alignment was also done to minimize the full width half maximum (FWHM) of the substrate peak. This was achieved by rotating the sample around the vertical axis normal to Axis 2, which is not shown in the diagram. A finer scan of Axis 2 around the substrate peak measured the peaks from the epitaxial film of the sample. The minimum resolution of the system was ±0.1 arcseconds. Rocking curves for bulk samples were typically measured ±500 arcseconds around the substrate with a 1.0 arcsecond step size and using a 1.0 second detector integration time. Typical DBR measurements were taken over a range of ±3000 arcseconds on either side of the substrate peak with 2.0 arcsecond steps and a 1.0 second integration time per measured point.

4.3 Hall-van der Pauw Measurements

Net free carrier concentrations and carrier mobilities of bulk epitaxial layers were determined using the Hall-van der Pauw technique. These measurements utilized the Hall effect [5] with the van der Pauw geometry method [6], which has become the classic way to measure semiconductor carrier characteristics. The technique required the sample to be uniform and of a known thickness.

The van der Pauw method provided a way to obtain the resistivity of an arbitrary shaped sample using four contacts located around its periphery. As shown in Figure 4.11(a), the resistance of the sample, $R_{AB,CD}$, was determined by injecting a constant current through two adjacent contacts and measuring the voltage generated across the other two contacts. Then, for a symmetrically patterned structure of layer thickness t, the resistivity, ρ, was calculated as

$$\rho = \frac{t\pi}{\ln 2} R_{AB,CD} \tag{4.4}$$

When a uniform sample is placed in a magnetic field which is normal to the current flowing through the sample, the Hall effect is the formation of an electric field normal to both the magnetic field and the current flow. This is seen in Figure 4.11(b), where the magnetic field is normal to the sample surface. The current is injected between contacts at opposite corners of the sample, and the generated voltage is measured between the other two contacts. The Hall coefficient, R_H, is then defined by the applied magnetic field, B_z, the injected current density, J_x, and the generated electric field, E_y, and it is proportional to the

carrier concentration, p for positive holes and n for negative electrons. All of these relations for R_H are

$$R_H \equiv \frac{E_y}{J_x B_z} = \frac{r_H}{pq} = \frac{-r_H}{nq} \tag{4.5}$$

where q is the electron charge and r_H is the Hall factor [7]. This factor varies with material and external conditions, but is always close to unity. Measurements for this work assumed $r_H=1$ for all calculations. Due to the geometry, E_y/J_x reduced to Vt/I, and thus only the thickness needed to be known. Then to increase accuracy R_H is often calculated by using a constant current and measuring $\Delta V/\Delta B$.

Experimental procedures for Hall-van der Pauw technique measurements began with sample preparation. Samples were cleaved into squares of approximately 5 mm long sides, and then were cleaned with a solvent rinse, followed by a DI-H_2O rinse, and blown dry with

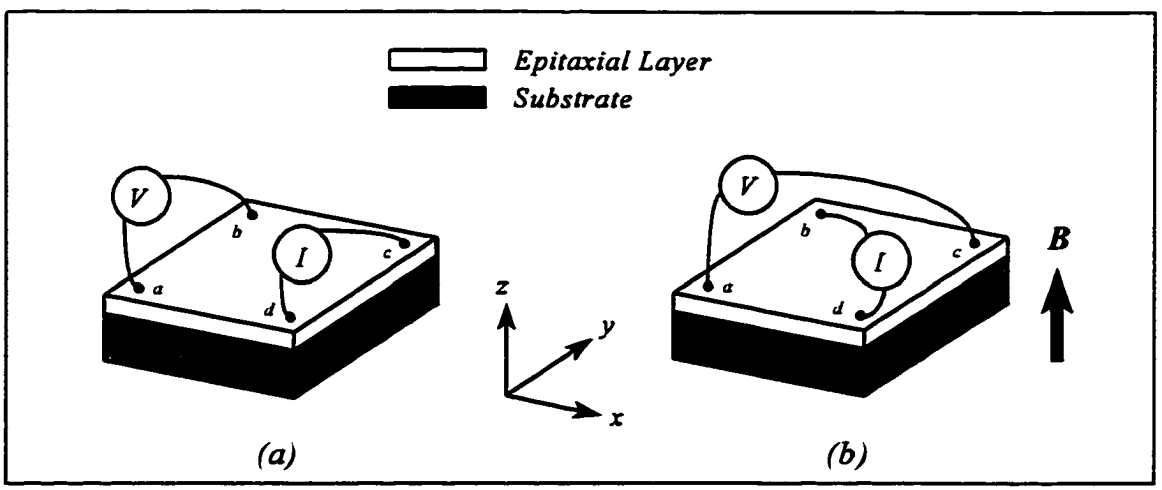

Figure 4.11 Configuration of Hall-van der Pauw measurements on a bulk epitaxial layer to determine (a) the resistivity and (b) the carrier concentration and mobility.

nitrogen gas. Four fresh eutectic contacts were then alloyed onto the sample corners at 300-350°C in a nitrogen ambient atmosphere for three minutes. InSn contacts were used for n-type epitaxial layers, and InZn contacts were used for p-type. The samples were then mounted in a holder with copper fingers making electrical connections for the Hall measurements.

The experimental Hall-van der Pauw apparatus was computer controlled. The constant current source was adjustable between 0.01 mA and 10 mA. The electromagnet for Hall measurements was set at 1400 Gauss. Measurements could be taken at 300 K and also at 77 K by immersing the sample in liquid nitrogen. In addition, every measured voltage value was an average of twenty consecutive measurements. The resistivity of the sample was found as described above and seen in Figure 4.11(a). The measurements were made for all eight contact combinations, and an average $R_{AB,CD}$ value was used in Equation (4.4) to determine the resistivity. Then the sample was subjected to the magnetic field for the Hall measurements as described above. The generated Hall voltage was measured for all four contact combinations, and then the direction of the magnetic field was reversed and the four measurements repeated. In this way the $\Delta V/\Delta B$ could be found as $(V_{Bup}-V_{Bdown})/2B$, and values from the four combinations were used in Equation (4.5) to find an average R_H. From this the net free carrier concentration and the carrier mobility in the epitaxial layer were calculated. In addition, from the polarity of the generated voltage, the carrier type was known.

4.4 Reflectance Measurements

Reflectance spectra of the Distributed Bragg Reflectors studied in this work were measured using a commercial Perkin-Elmer Lambda 2 UV/VIS Spectrometer. The Lambda 2 has a monochromator with a grating of 1053 lines/mm, and uses a double beam optical path. One optical path is directed onto the sample, and the other path is for reference in order to provide long term stability, reference compensation, and baseline correction. Measurements were computer controlled with the ability to scan over a wavelength range of 190 nm to 1100 nm. The wavelength accuracy and reproducibility were ±0.3 nm and ±0.1 nm, respectively. The sample holder for the Lambda 2 was designed for large area samples, on the order of 2 cm on a side, but the actual beam spot size was roughly 2 mm by 5 mm. Measurements were typically made on samples which were one-quarter of a two inch diameter semiconductor wafer in size.

Experimental procedures for measuring reflectance spectra were very straight forward. First the sample was cleaned with successive rinses of trichloroethylene, acetone, methanol, and deionized water, and was blown dry with nitrogen gas. Before measuring the sample in the Lambda 2, scans were done on a Labsphere reflectance calibration standard, SPRS-010. Thus the system background was normalized by setting the SPRS-010 response to 100% across the entire wavelength spectrum. Scans of the DBRs were typically made over the wavelength region of interest, from 500 nm to 800 nm, using a 1.0 nm step size and a 120 nm/min scan rate. Absolute reflectance factors of the SPRS-010 standard, which were traceable to the National Institute of Standards and Technology (NIST) with a stated uncertainty of ±0.5%, were then used to correct the raw DBR data. This correction used a

linear interpolation scheme for data points between those provided for the SPRS-010, which were every 50 nm over a 250 nm to 2500 nm spectral range. Figure 4.12 shows an example of both the raw and corrected DBR spectra, along with the spectrum for the SPRS-010 standard. Note that the normalization of the absolute reflectance value of the standard, which was around 90%, to 100% in the Lambda 2 background correction caused the raw DBR peak, measured at over 110%, to be a 99.5% reflectance.

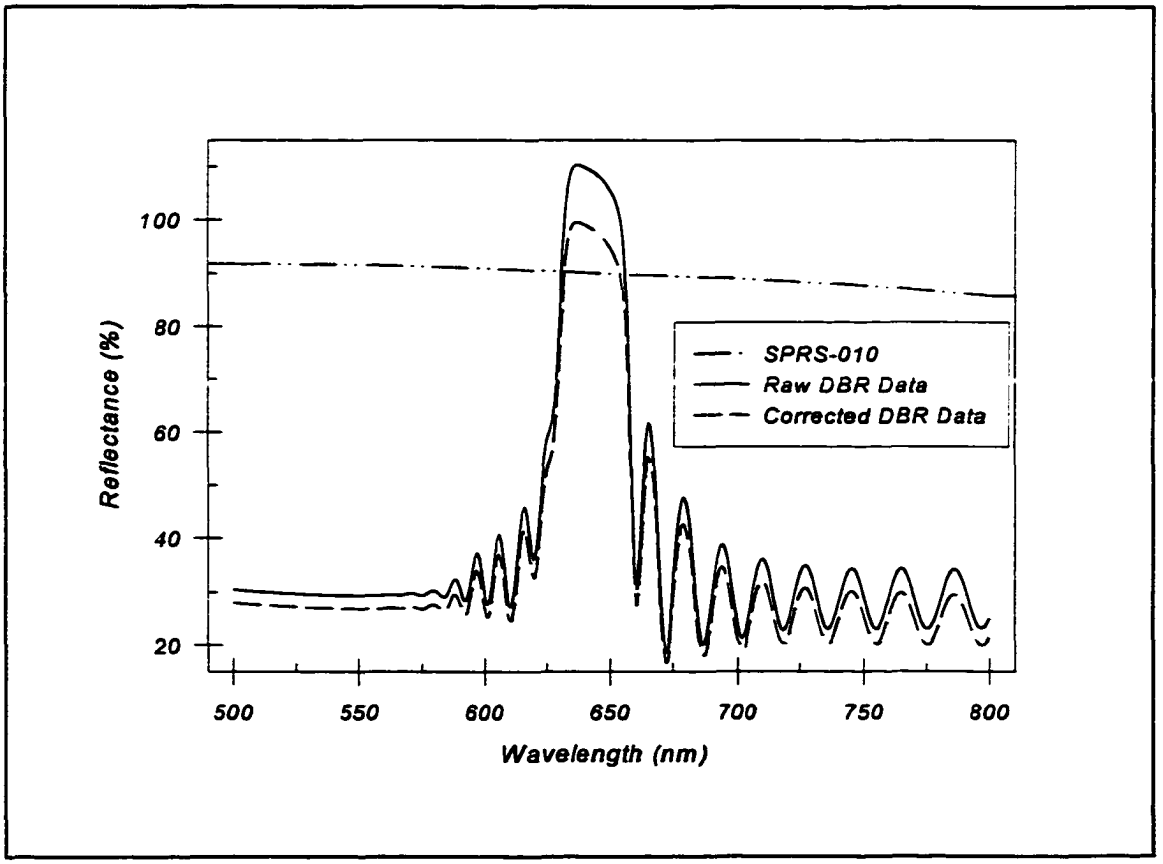

Figure 4.12 Sample reflectance plot showing both raw and corrected DBR data along with data for the SPRS-010 calibration sample.

4.5 Transmission Line Model

The final experimental procedure to be discussed is the determination of series resistance in epitaxial DBR structures using the Transmission Line Model (TLM) technique. TLM theory and application to DBRs, test structure fabrication, and resistance measurement and determination will all be described.

4.5.1 TLM Theory and DBR Application

TLM measurements were originally proposed by Shockley [8] as a convenient method for determining the specific contact resistance, ρ_c ($\Omega \cdot cm^2$), of planar ohmic contacts. A series of resistance measurements are made between identical contacts of known length, d, and width, W, with varied separation distances, as seen in Figure 4.13(a). Plotting the measured resistance, R, versus separation distance, L, and extrapolating back to the vertical axis allows for the determination of the contact resistance, R_c (Ω), from the y-intercept as seen in Figure 4.13(b). This linear resistance relation can be expressed as

$$R(L) = \frac{2R_{SK}L_T}{W}\coth(d/L_T) + \frac{R_{SH}}{W}L \qquad (4.6)$$

where R_{SH} and R_{SK} are the sheet resistances in the epitaxial layers between and beneath the contacts, respectively, and L_T is the transfer length and is a function of L_x as shown in Figure 4.13(b). The first term in Equation (4.6) is just the y-intercept, $2R_c$, while the slope of the line can be used to determine R_{SH}. Assuming $R_{SH}=R_{SK}$ and $d>>L_T$, then L_T is simply $L_x/2$, and the specific contact resistance can be easily obtained from

$$\rho_c = R_{SK}(L_T)^2 \tag{4.7}$$

Unfortunately, due to the alloying or sintering process at the metal-semiconductor interface, the sheet resistance of the epitaxial layers beneath the contacts is not the same as between the contacts in many instances ($R_{SK} \neq R_{SH}$). This means L_T is no longer $L_x/2$, and determination of ρ_c is not so easy. In order to account for this modified sheet resistance, the total resistance of the interface plus the layers beneath the contact is needed. This additional measured value is referred to as the contact end resistance, R_E [9]. In terms of the above parameters it is expressed as

$$R_E = \frac{\sqrt{R_{SK}\rho_c}}{W} \cdot \frac{1}{\sinh(d/L_T)} \tag{4.8}$$

Now, Equations (4.6) and (4.7) can be used with (4.8) to solve for L_T and thus ρ_c.

Figure 4.14(a) demonstrates a simple method for measuring R_E, and thus ρ_c. By making the three resistance measurements between the three adjacent contacts, it can be shown [9] that the contact end resistance is

$$R_E = \frac{1}{2}(R_1 + R_2 - R_3) \tag{4.9}$$

Using the known contact spacings and R_1 and R_2, the contact resistance R_c can be calculated. Then Equations (4.6) through (4.8) can be used to determine the specific contact resistance.

The TLM measurement process was applied to determine the DBR mirror resistances by performing measurements both before and after etching mesas through the mirror stack

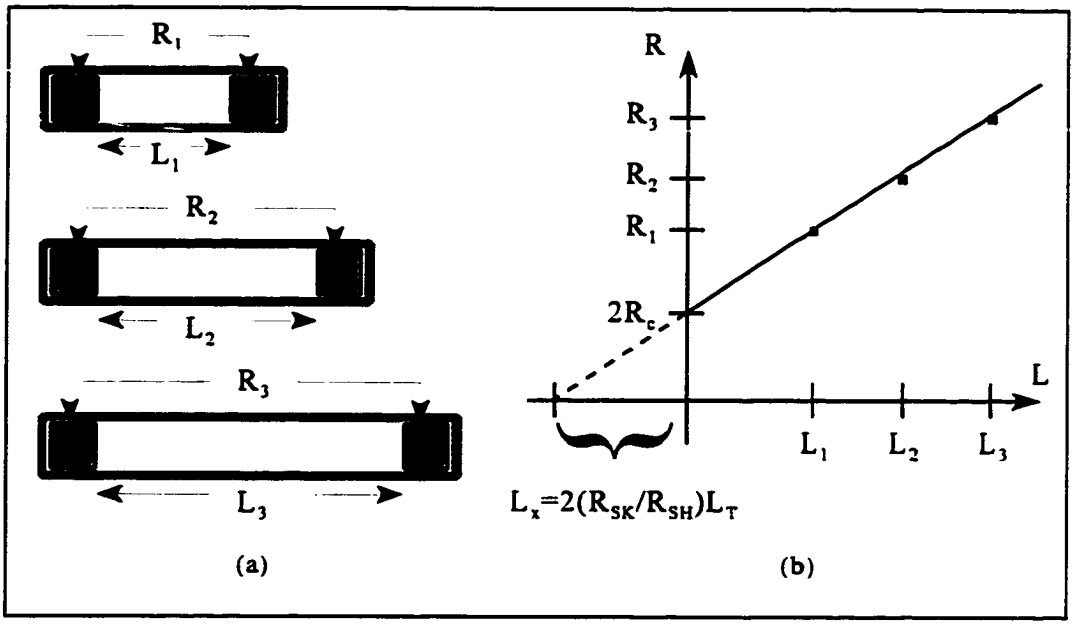

Figure 4.13 TLM measurements: (a) measured resistances for varying separation distances and (b) plotted resistance versus length to find the contact resistance.

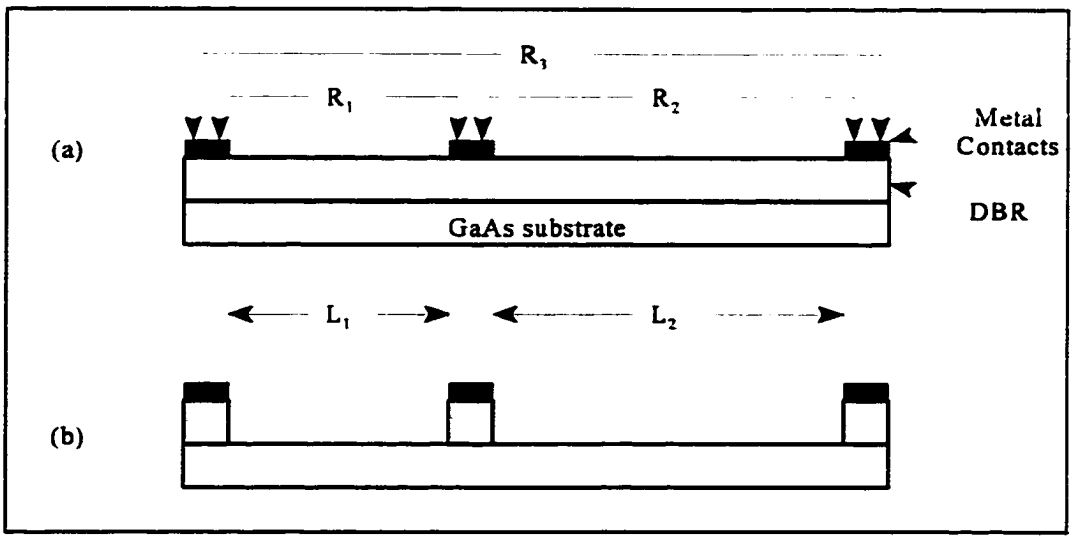

Figure 4.14 Three contact method for determining contact end resistance (R_E) and thus the specific contact resistance (ρ_c).

down to the GaAs substrate [10]. The TLM measurement with contacts on the as-grown mirror, Figure 4.14(a), determined of the actual metal-semiconductor contact resistance. After etching through the DBR stack to the conducting substrate, Figure 4.14(b), the TLM measurement determined a "contact" resistance which consisted of both the metal contact resistance and the DBR series resistance. Thus the resistance of the DBR itself would be the difference between the two measured contact resistances. In order to ensure identical metal contacts and test conditions, the two TLM test structures were fabricated simultaneously side by side on single pieces of the epitaxially grown DBR structures.

4.5.2 TLM Test Structure Fabrication

TLM test structures were fabricated using standard photolithography techniques and a three mask set specifically designed for this project. All photolithography work was done in the CSU cleanroom. A Karl-Suss mask aligner was used for aligning the mask patterns on the samples, and for exposing the photoresist. An internally developed SiO_2 chemical vapor deposition (CVD) system was used to grow dielectric insulators on the samples. And an electron beam evaporator was used to deposit the metal contact layers.

The schematic diagram of Figure 4.15 demonstrates the function of each individual mask in the set, and Figure 4.16 shows all three mask layers overlapped in a single die pattern. The first mask defined the size and shape of the mesas which were etched into the samples. The second mask defined the contact vias to be made through the insulating dielectrics covering the mesa tops. And the third mask was for a metal lift-off process which defined the metal pads used to electrically probe the test structure. The actual masks

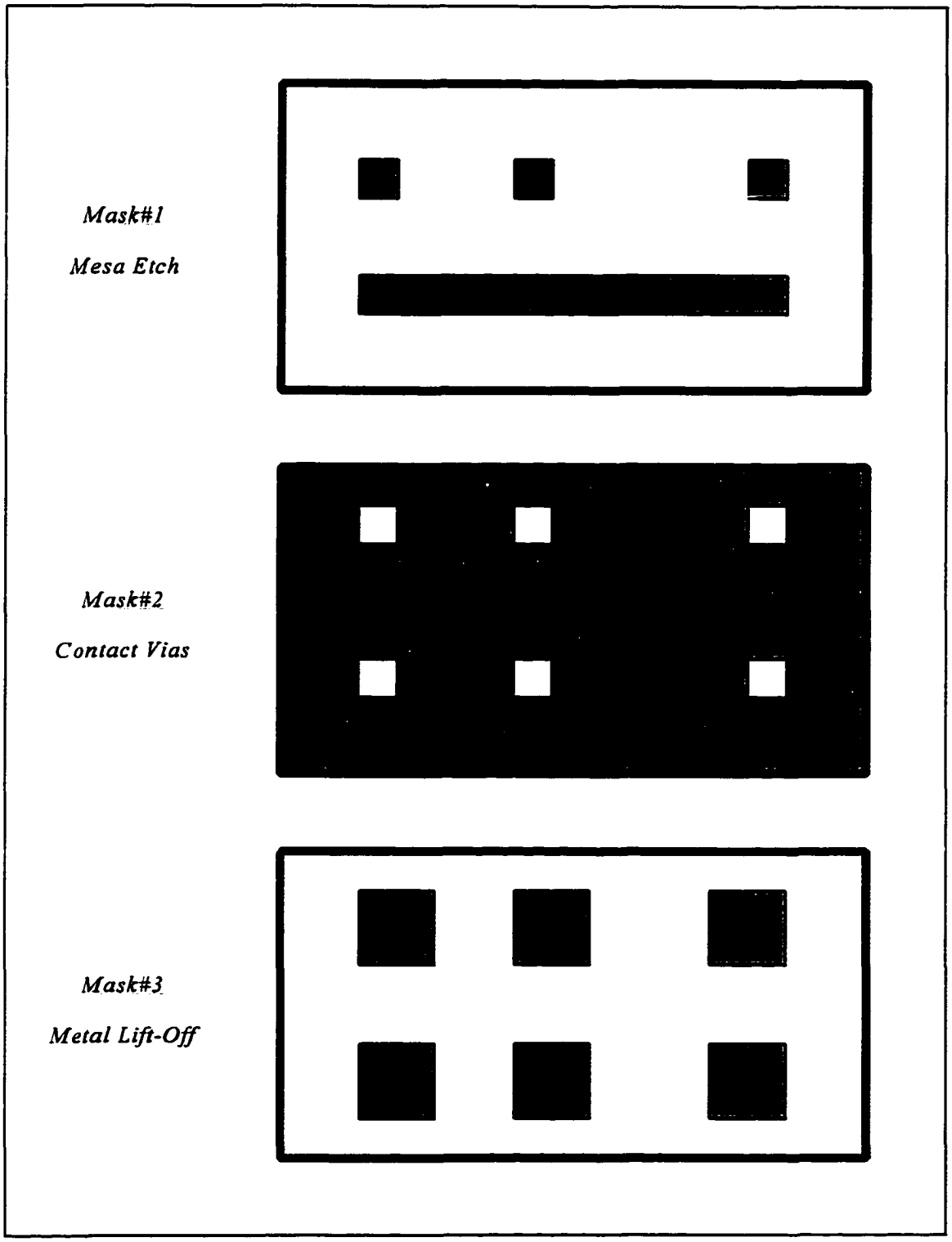

Figure 4.15 Schematic diagram of the function of each mask in the TLM set.

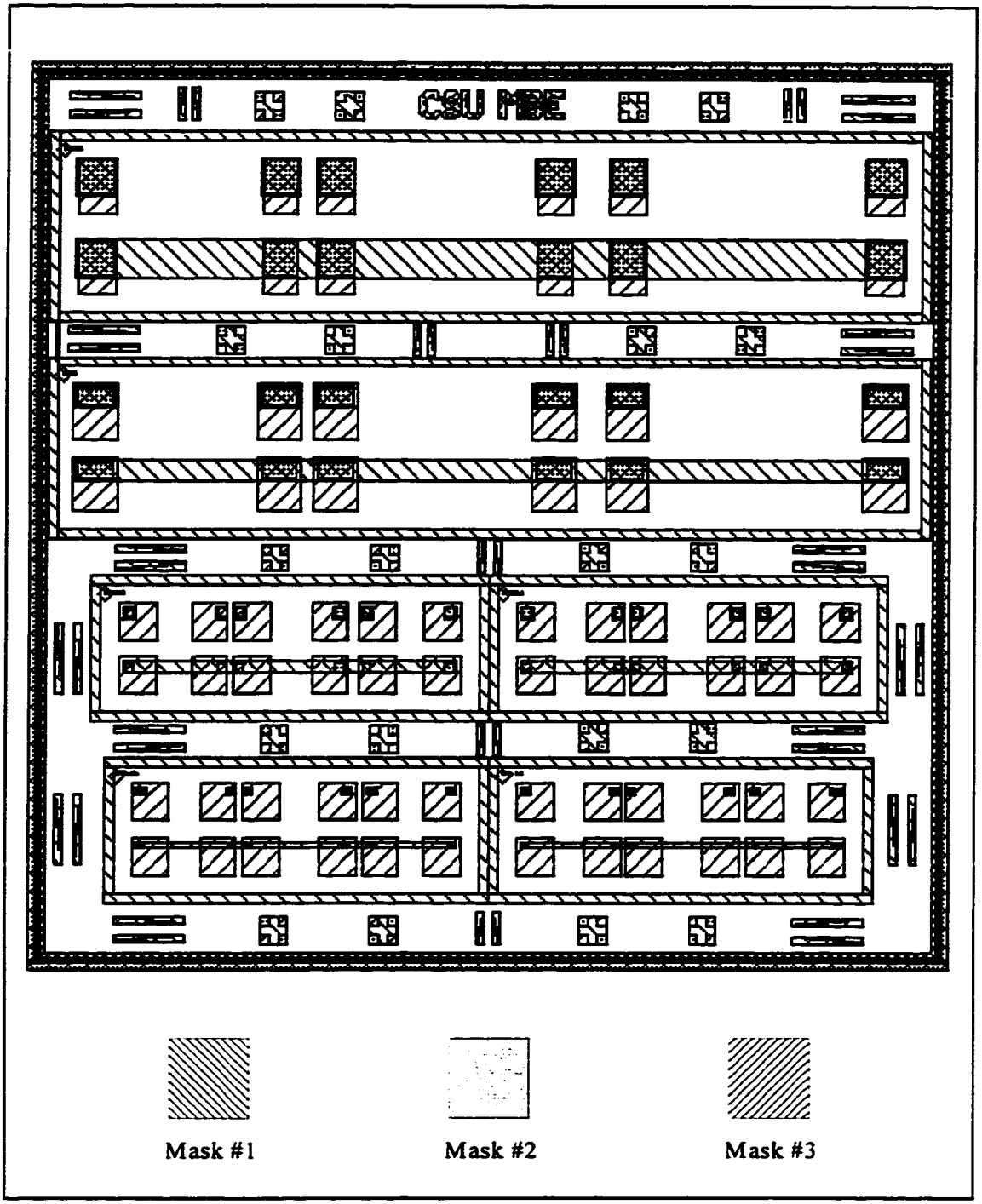

Figure 4.16 A single die pattern of the DBR mask set showing the actual layout with all three mask layers overlapped.

consisted of a 10 by 10 array of the single die pattern. Each pattern had six different TLM layouts with mesa sizes varying from 100 μm by 100 μm down to 10 μm by 20 μm. The various sizes ensured that the resolution of the measurement was small enough to measure the specific contact resistances for the given resistivities of the stacks.

The general steps involved in fabricating the TLM test structures are shown schematically in Figure 4.17; the details of the process are given in Appendix A. Pieces measuring roughly 5 mm by 10 mm were cut out of the DBR wafers for processing, and they were cleaned with a solvent rinse followed by a DI-H_2O rinse. First a thick layer of SiO_2 was deposited onto the sample by CVD. Then the first mask was used to define a photoresist mask of the mesa pattern, and the SiO_2 was selectively etched with buffered HF to transfer the mesa pattern to the dielectric. Then, with the dielectric protecting regions of the sample, mesas were etched through the DBR to the conducting substrate using a chemical assisted ion beam etching system. Then a thin CVD SiO_2 layer was deposited and a polyimide process was performed to provide a more planar surface and to electrically isolate the conducting substrate from the metal contact pads to be deposited later. The second mask was used to define a photoresist mask for opening vias in the polyimide down to the SiO_2 on the mesa tops. The polyimide etches anisotropically, with approximately 45° sidewalls, in the photoresist developer, and because of the thickness of the polyimide the resulting holes were rounded and larger than defined by the mask. For this reason the second mask was used again in order to define a photoresist mask aligned within the large polyimide holes on top of the mesas. Then sharp, well defined contact vias were etched in the SiO_2 to expose clean DBR surfaces on the mesa tops. Finally, a metal lift-off process was performed, using the

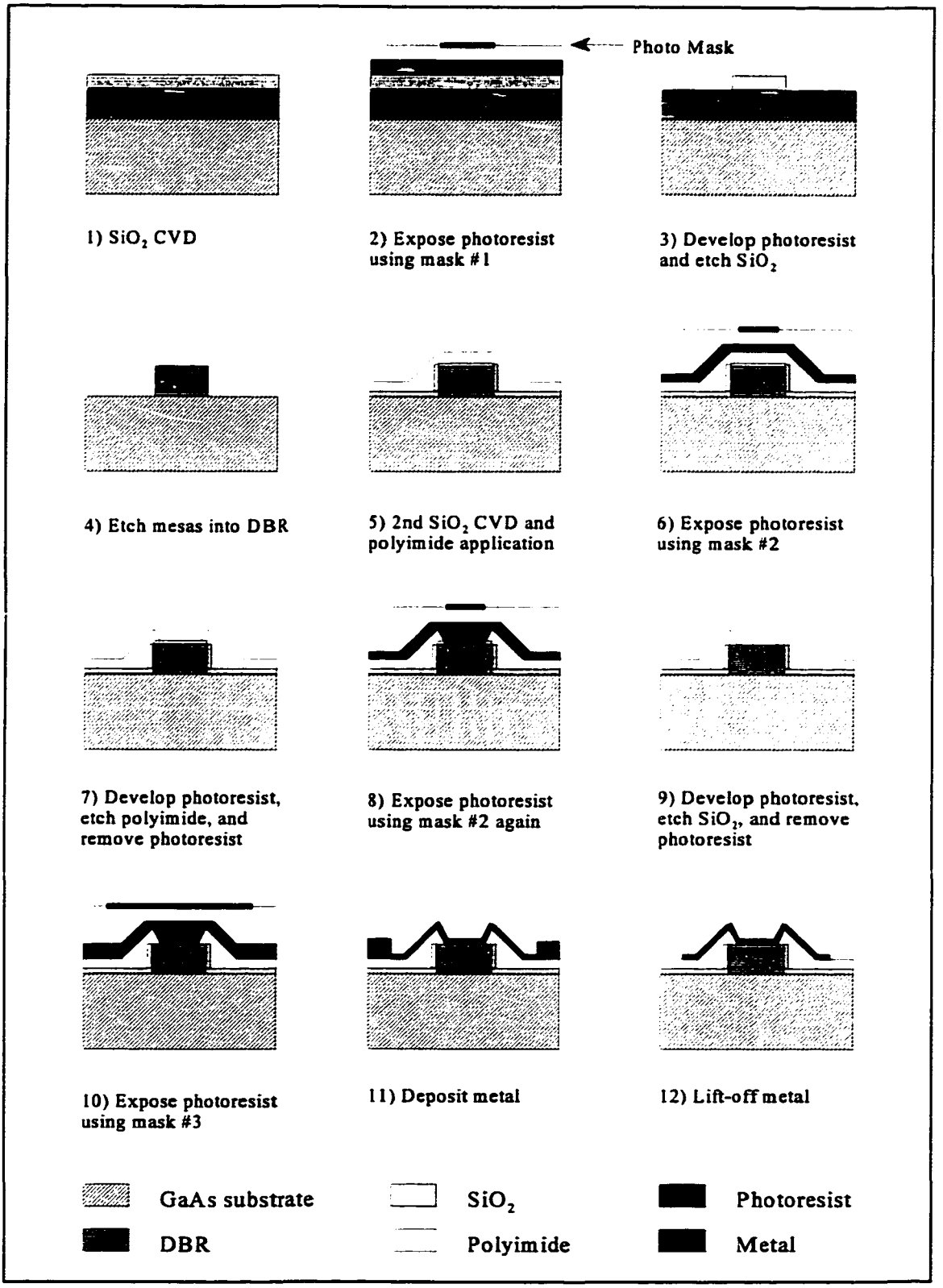

Figure 4.17 Process steps for fabricating the TLM test structures.

third mask, to make metal contact to the DBR mesas with pads large enough to probe. For n-type DBRs, the contacts were made using Ge/Au/Ni/Au metal layers, with 250Å/520Å/150Å/1000Å thicknesses. Ti/Au metal layers, with thicknesses of 600Å/2500Å, were used for contacts to the p-type DBRs.

4.5.3 TLM Resistance Measurements

Once the TLM structure fabrication was completed, resistance measurements were performed. Samples were placed on a standard probe stand, and a Hewlett-Packard 4145B Semiconductor Parameter Analyzer was used to make the measurements. R_1, R_2, and R_3 were measured for multiple sets of three consecutive, identical contacts, as described above. Then calculations were performed using Equations (4.6) through (4.9) to extract the specific contact resistances for the metal on top of the DBR stacks and for the DBR mesas on top of the GaAs substrate. Then, for a given sample, the specific contact resistance for the DBR structure itself was found as the difference between the values for the two geometries.

REFERENCES: CHAPTER IV

[1] M. Herman and H. Sitter, Molecular Beam Epitaxy: Fundamentals and Current Status; Springer-Verlag: New York, 1989.

[2] J. Tsao, Materials Fundamentals of Molecular Beam Epitaxy; Academic Press: Boston, 1993.

[3] G. Robinson, "Gas-source MBE," in the Handbook of Thin Film Process Technology, edited by D. Glocker and S. Shah; Institute of Physics: Philadelphia, 1995.

[4] J. Mahan, K. Geib, G. Robinson, and R. Long, "A review of the geometrical fundamentals of reflection high energy electron diffraction with application to silicon surfaces," *J. Vac. Sci. Technol.* **A8**, 3692 (1990).

[5] E. Hall, "On a new action of the magnet on electric circuits," *Am. J. Math.* **2**, 287 (1879).

[6] L. van der Pauw, "A method of measuring specific resistivity and Hall effect of discs of arbitrary shape," *Phillips Res. Rep.* **13**, 1 (1958).

[7] R. Pierret, Advanced Semiconductor Fundamentals (Modular Series on Solid State Devices, Volume VI); Addison-Wesley: Reading, MA, 1987.

[8] W. Shockley, "Research and investigation of inverse epitaxial UHF power transistors," *Report No. Al-TOR-64-207*, Air Force Atomic Laboratory, Wright-Patterson Air Force Base, Ohio, September 1964.

[9] G. Reeves and H. Harrison, "Obtaining the specific contact resistance from transmission line model measurements," *IEEE Elec. Device Lett.* **3**, 111 (1982).

[10] K. Tai, L. Yang, Y. Wang, J. Wynn, and A. Cho, "Drastic reduction of series resistance in doped semiconductor distributed Bragg reflectors for surface-emitting lasers," *Appl. Phys. Lett.* **56**, 2496 (1990).

CHAPTER V

RESULTS AND DISCUSSION

This chapter presents and discusses the results obtained from the experiments carried out in this project. The first two sections describe the initial material quality studies. First the growth and doping of AlGaAs with high aluminum content is described, and the measured data presented. Then the AlGaInP quaternary alloys are qualified, with experiments determining refractive index values and carrier concentrations discussed. The next sections present the growth and structural characterization of both the two low band offset DBRs and their two control DBR samples. Growth discussions include structural design and growth parameters, while characterization includes measured data from x-ray diffraction and reflectance experiments. The final section presents the transmission line measurements and the resulting specific contact resistance data. The control sample DBRs should have a larger resistance due to their larger heterojunction band offsets.

5.1 AlGaAs Material Study

This section describes the molecular beam epitaxy (MBE) growth and the characterization of AlGaAs alloys with high aluminum content ($x_T>0.8$). First, results are presented from growths exploring the optimum parameters for obtaining high quality AlAs.

Then some background is given on the difficulties documented by other researchers in obtaining electrically conducting AlGaAs with high carrier concentrations. This section concludes with results of an AlGaAs doping study using the films grown for this project.

5.1.1 AlAs Growth Conditions

The growth of the binary AlAs had never been characterized in the CSU GSMBE system. The first step was to find the proper growth regime, that is the proper combinations of growth rates and substrate temperatures (T_{sub}), where high quality material is obtained. Double crystal x-ray diffraction (DCXD) spectra were used as a judge of material quality; the narrower the full-width half-maximum (FWHM) of the epilayer peak, the higher the crystal quality. This is demonstrated in Figure 5.1, where the x-ray spectra for two different samples are shown. For MBE1048, the epilayer peak is broad and flat, indicating a poor crystal morphology. On the other hand, MBE1063 shows a well defined epilayer peak indicative of good crystal morphology (i.e., a high degree of structural perfection). Computer simulations indicated that the minimum DCXD FWHM of AlAs grown on GaAs is 21 arcseconds. The FWHM of MBE1063 is 24", so this x-ray spectrum is indeed indicative of high quality AlAs.

A series of AlAs samples was grown at various substrate temperatures and growth rates. Each sample was evaluated by DCXD and plotted at its own growth conditions in a plot of growth rate versus T_{sub}. This is shown in Figure 5.2, where open symbols represent poor crystal quality and closed symbols represent good crystal quality. At 530°C, poor quality material was obtained for a high growth rate of 1.0 μm/hr, while below 0.5 μm/hr

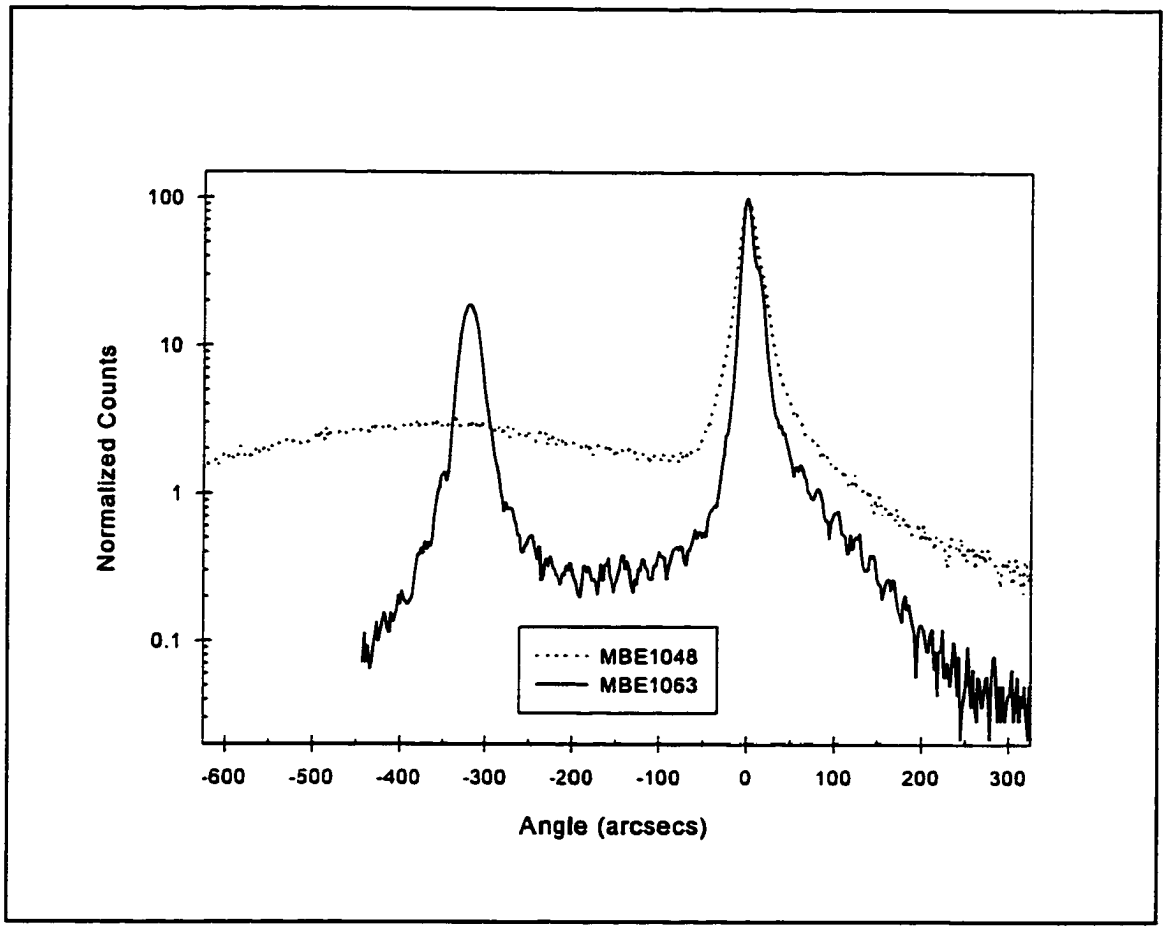

Figure 5.1 DCXD spectra of bulk AlAs samples demonstrating high quality crystal morphology (MBE1063) and poor morphology (MBE1048).

good crystal material was obtained. Growth of good quality AlAs continued as T_{sub} was decreased down to 480°C, but at 470°C the morphology again turned poor. The transition region between good and poor crystal quality indicated on the plot is an estimate from the limited number of AlAs samples grown. It is an indication of a transition from a layer by layer growth mechanism, which results in good quality morphology, to an island growth mechanism resulting in a rougher surface and wider x-ray spectrum. Figure 5.2 thus provides the growth parameter window for obtaining high quality AlAs in the CSU GSMBE system.

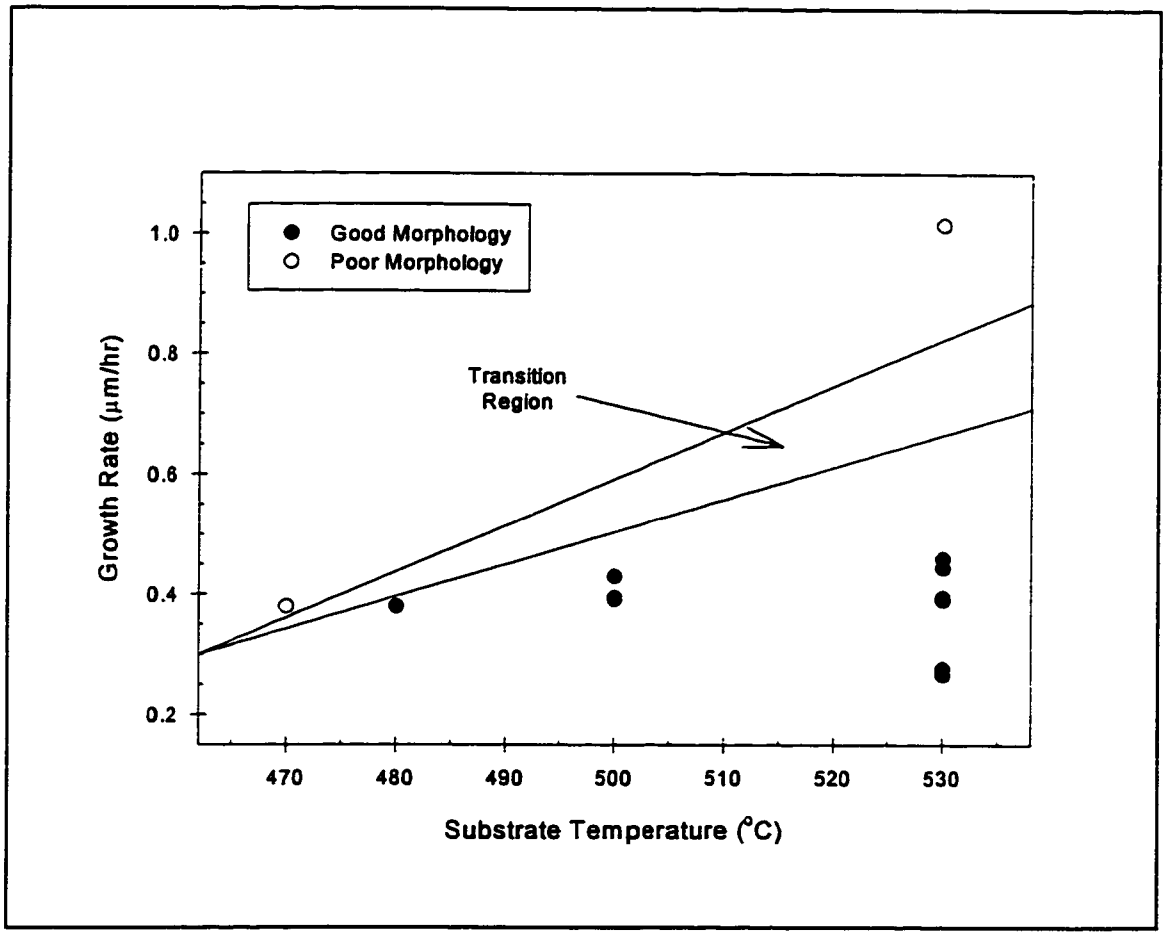

Figure 5.2 AlAs crystal quality as a function of growth parameters plotted in the growth space. Filled circles indicate good crystal morphology as measured by DCXD, and open circles indicate poor morphology.

5.1.2 AlGaAs Doping Limits

As mentioned in Chapter III, obtaining high electrically active carrier concentrations in AlAs is difficult. Several mechanisms which can cause the measured free carrier concentration to be much lower than the concentration of dopant atoms are discussed below. Very few published studies of AlGaAs doping by beryllium (Be) and silicon (Si), the two most common dopants for MBE-grown III-V semiconductors, have carried out experiments at high Al content (x_T>0.8) and at high dopant concentrations. This section will briefly look

at some of the previous work so that the results of the next section may be placed in a more knowledgeable context.

Data on maximum carrier concentrations obtainable in MBE-grown AlGaAs using Be and Si dopants is surprisingly incomplete given how common the materials are. Silicon doped n-type carrier concentrations have been reported up to the mid $10^{18}\,cm^{-3}$ over the full composition range of AlGaAs [1]. In addition, for $xT<0.5$, the carrier concentration is roughly equivalent to the number of dopant atoms until the concentration saturates in the 10^{18} cm^{-3} range. Studies of beryllium p-type doping limits have achieved hole concentrations of $2\times10^{20}\,cm^{-3}$ in GaAs [2], and $3\times10^{19}\,cm^{-3}$ in $Al_{0.3}Ga_{0.7}As$ [3], but for pure AlAs the maximum hole concentration is reported to be only $5\times10^{17}\,cm^{-3}$ [4]. A liquid phase epitaxy (LPE) study did obtain a hole concentration of 6×10^{17} cm^{-3} for $Al_{0.9}Ga_{0.1}As$, with a Be acceptor concentration of $3.5\times10^{18}\,cm^{-3}$, but no data was given for pure AlAs [5].

Possible explanations for the saturation of carrier concentrations with increasing dopant concentration include dopant precipitation [6], compensation [2], and redistribution [7]. Precipitation is the clustering together of dopant atoms, rather than their homogeneous distribution throughout the epilayer, such that they no longer act as substitutional dopants in a semiconductor crystal lattice. An example of compensation in n-GaAs would be the incorporation of Si atoms in As lattice sites, forming acceptors, rather than in the preferential Ga sites to form donors, with the effect of the donor-acceptor pair being the cancellation of each other. The onset of the pair compensation phenomena occurs at high dopant concentrations such that a continued increase in the number of dopant atoms does not increase the carrier concentration. Redistribution, which has been observed for Be in

AlGaAs, can occur either as a carry-forward mechanism, where Be accumulates and rides on the surface during growth and thus is not incorporated into the film, or as diffusion of the dopant atoms away from their original position. Diffusion has been observed in p-type GaAs/AlAs DBRs [4], where the diffusivity of Be in AlAs is much larger than in GaAs, and as the Be moves quickly out of the AlAs it slows in the GaAs and thus piles up at the heterojunctions. This report claimed the solid solubility limit of Be in AlAs was $5\times10^{17}cm^{-3}$.

One of the most systematic AlGaAs doping studies included the determination of the donor (E_d) and acceptor (E_a) activation energies [8]. These energies are defined as the difference between the position of the conduction (valence) band and the position of donor (acceptor) energy level, with positive values indicating dopant levels within the semiconductor band gap. Figure 5.3(a) shows the plot of silicon donor activation energy in AlGaAs as a function of Al composition. E_d was found to increase from 10 meV for GaAs and reach a maximum in the region of the Γ-X crossover, near xT=0.5. Then E_d steadily dropped to about 60 meV for AlAs. The larger E_d value, or deeper donor level, means that at room temperature the number of ionized impurities, that is the fraction of donor atoms which become electrically active, will be smaller for AlAs than for GaAs, assuming a constant Si atomic density. Similarly, as seen in the plot of Figure 5.3(b), E_a for Be in AlGaAs was found to slowly increase from 15 meV for GaAs to 41 meV for AlGaAs with xT=0.7, the highest Al composition included in the study. The theoretical, dashed curve extrapolates E_a to around 70 meV for AlAs; so once again the number of ionized impurities in AlAs would be smaller than in GaAs for a given Be atomic density. Typical carrier concentrations in [8] were all less than $10^{18}\ cm^{-3}$, and no indication was given that higher

(a)

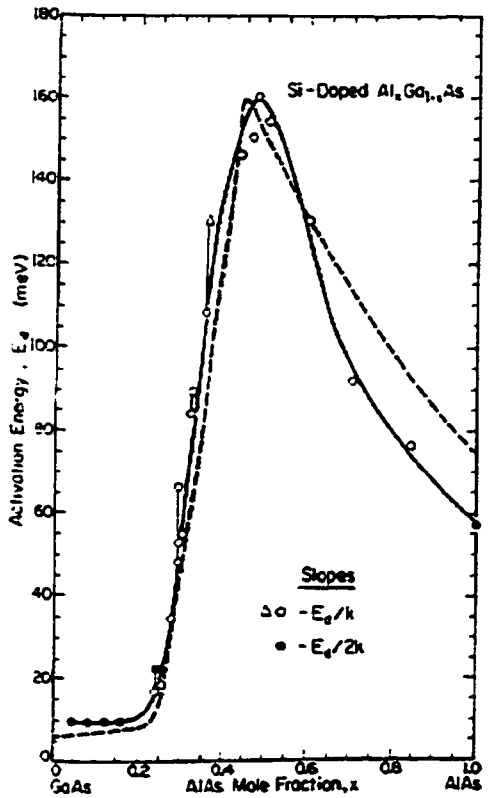

(b)

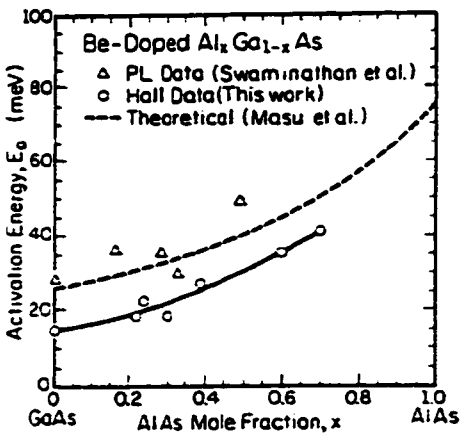

Figure 5.3 Plots of the composition dependent donor (a) and acceptor (b) activation energies in AlGaAs from Chand, et. al. [8]. The solid lines connect experimental data, while the dashed lines are obtained from theoretical calculations. In (a) the symbols indicate growth temperature, circles for 610°C and triangles for 700°C, and the vertical bars show variation of E_d with doping concentration for a given value of x.

concentrations were attempted, although the lack of p-type results for xT>0.7 may indicate that samples were grown, but electrically conductive material was not achieved. As indicated by the vertical bars in Figure 5.3(a), E_d varied with doping concentration for a given Al content. The paper reported an inverse relationship, with E_d decreasing as the doping level increased.

5.1.3 AlGaAs Doping Study

This section describes the results of the AlGaAs doping study done in an attempt to obtain carrier concentrations high enough ($2\times10^{18}cm^{-3}$) to be used in the DBRs. A series of doped AlGaAs (xT>0.85) samples were grown at varying substrate temperatures and dopant flux values. Typical growth rates were around 0.4 μm/hr, although two data points were taken at 0.27 μm/hr. Net carrier concentrations were measured at room temperature using the Hall-van der Pauw technique. The results are summarized in plots of carrier concentration versus inverse dopant cell temperature for both silicon, Figure 5.4, and beryllium, Figure 5.5, dopants. The concentrations are as-measured values, and have not been normalized to a constant growth rate. Note that as the cell temperature increases, moving from right to left on the plots, the flux from the cells also increases. This is demonstrated by the open circles on the plot which indicate the target doping values. Carrier concentrations measured in bulk layers of GaAs, for the same flux from the dopant source cell and normalized to the target growth rate, were used as the target doping levels. As seen in the previous section, the carrier activation in GaAs is typically 100% [1], so the target concentration is assumed to be equal to the dopant concentration, meaning the target is the

maximum free carrier concentration obtainable. The filled symbols in the plots indicate the substrate growth temperature of the sample measured to obtain the given data point. Note that for the range of T_{sub} used in Figures 5.4 and 5.5 the carrier concentrations in GaAs are independent of T_{sub}. It also should be noted that in both figures the data points at 2×10^{15} cm^{-3} were not measured values, but rather were used to indicate samples that were grown but proved to be electrically non-conducting.

For the n-type case of Figure 5.4, the free electron concentration increased with silicon cell temperature at a given T_{sub}=530°C, solid circles, but the value appeared to saturate at about 1×10^{17} cm^{-3}. However, as seen in the target data, the amount of scatter in the data is such that a definite conclusion that saturation has been observed cannot be said with any confidence. In order to verify that saturation occurred, possibly due to compensation as described earlier, more samples would need to be grown and measured.

Of bigger concern is the fact that the net free carrier concentration is over two orders of magnitude smaller than the assumed dopant concentration indicated by the open circles. This large discrepancy cannot be explained simply by the difference in Si activation energies for GaAs and AlAs, as described in the previous section. The ratio of ionized dopants to total doping concentration, N_D^+/N_D, can be calculated using [9]

$$\frac{N_D^+}{N_D}=\frac{1}{1+g_D\exp[\frac{E_F-(E_c-E_d)}{kT}]} \tag{5.1}$$

where g_D is the donor degeneracy factor, E_F is the position of the Fermi level, E_c is the position of the conduction band, k is the Boltzmann constant, and T is the temperature in

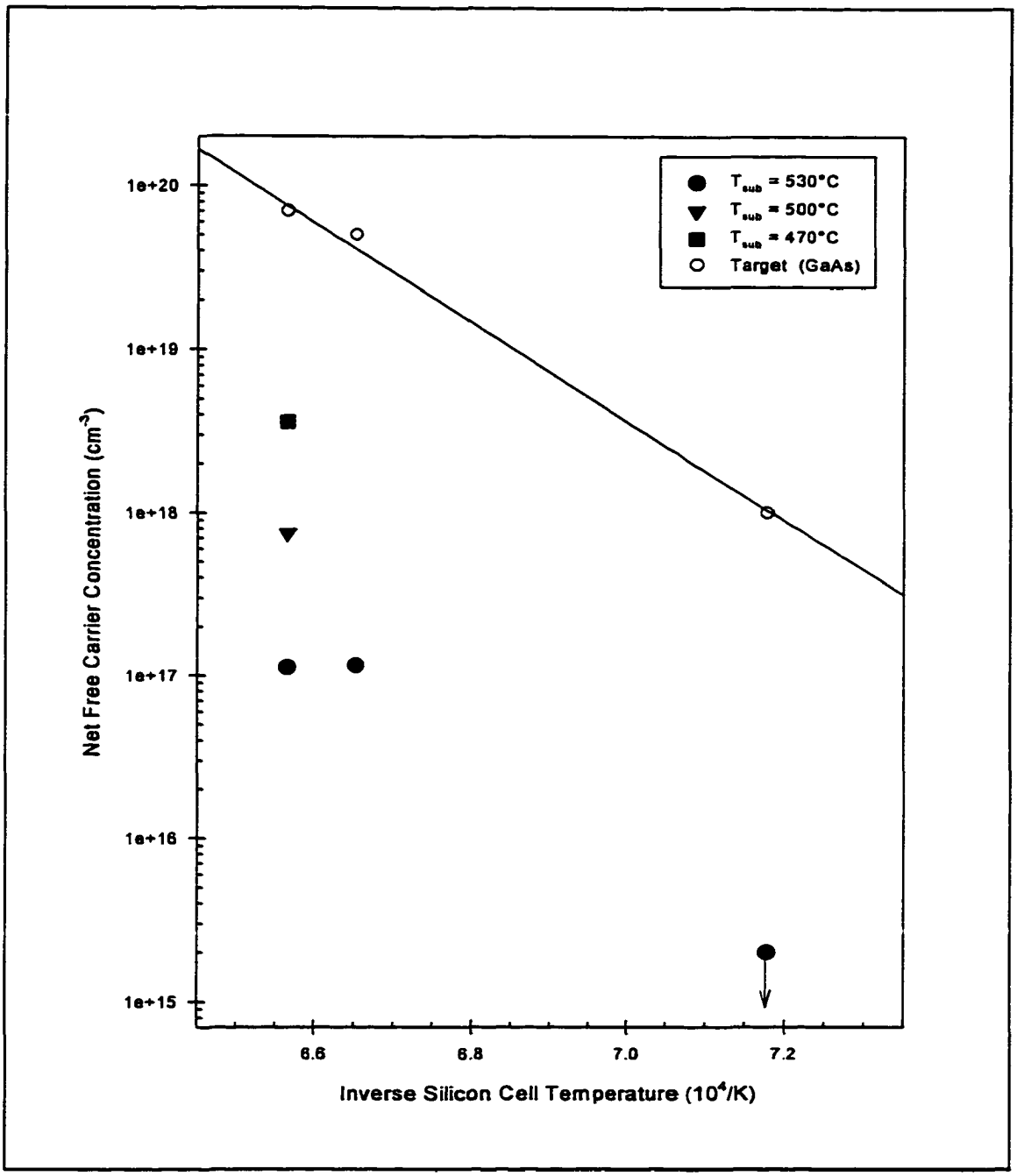

Figure 5.4 As-measured n-type AlAs net free carrier concentration as a function of inverse dopant cell temperature and of substrate growth temperature (T_{sub}). The data point at 2×10^{15} cm^{-3} indicates a measured sample which was non-conducting.

Kelvin. Assuming Fermi-Dirac statistics for determining the Fermi level and using E_d=75 meV for AlAs, which is a large estimate from the theoretical curve of Figure 5.3(a), 7% of the targeted 7.0×10^{19} cm^{-3} Si atoms should be ionized in AlAs at room temperature. This is 35 times larger than the 0.2% ratio of free carriers to target doping that Figure 5.4 indicates.

Some other mechanism must be at work which limits the free electron concentration in the AlAs as compared to GaAs. The most likely possibility is the existence of deep level traps in the energy band gap of the material which capture the electron from the silicon donor. The role played by Al could cause this either directly or indirectly. At high Al content in AlGaAs, the crystal lattice may distort and form native defects which may act as deep levels. Or, since Al tends to getter impurities such as oxygen, higher Al content means more unwanted impurities are incorporated with electrically active deep levels. Either mechanism implies that as the Al content increases the trap concentration should increase, and thus the carrier to dopant concentration ratio should decrease. Unfortunately Figure 5.4 does not provide a large enough sample size to see such a trend.

Returning to Figure 5.4, for a constant donor flux the electron concentration increased with decreasing T_{sub}, reaching 3.6×10^{18} cm^{-3} for T_{sub}=470°C. This is consistent with published reports that demonstrate carrier concentrations for both Si and Be dopants decrease with increasing substrate temperature for a given dopant level [2]. The electron concentration was still over an order of magnitude less than the silicon dopant concentration, but the goal of high electron concentrations for DBRs was obtained.

As seen in Figure 5.5, similar results were observed for p-type AlGaAs doped with beryllium. In this case, though, the hole concentration in AlAs apparently saturated at about

3×10^{17} cm^{-3} for both increased Be flux, or cell temperature, and for decreased T_{sub}. This corresponds very well to the results for Be in MBE grown AlAs quoted in the previous section [4]. However, as indicated by the shaded symbols, the inclusion of 15% gallium increased the hole concentration to 2×10^{18} cm^{-3} for T_{sub} at 500°C and 480°C. There is still over an order of magnitude difference between the number of acceptor atoms and the number of holes, which again cannot be explained solely by the activation energy differences. The increased hole concentration with decreased Al content follows the trend of the deep level trap mechanism discussed above. It is also possible that the small amount of gallium provides the beryllium with preferential occupation sites that become ionized acceptors, rather than filling sites that become compensating pairs as described in the previous section. Regardless of the mechanism, the bottom line is that large enough hole concentrations were obtained in high Al content AlGaAs for use in the DBRs.

To summarize, the results of the AlGaAs material study affected the choices of materials for the low band offset DBRs. The optimum choice for the n-type DBR, AlAs/AlGaInP with xQ=0.10, was still valid since the AlAs was successfully doped to the desired concentration levels. Looking back at Table 3.2, the optimum material system for the p-type DBR would be either AlAs/AlGaInP with xQ=0.25, or AlGaAs/AlGaInP with xT=0.9 and xQ=0.14. The former choice would be preferred both for the aesthetic reason of symmetry with the n-DBR and for the fact that it would be easier to grow. However, AlAs could not be doped high enough with Be so this system was eliminated. Since the AlGaAs with xT=0.9 was successfully doped to high carrier concentrations the latter choice was still valid for the low valence band offset DBR.

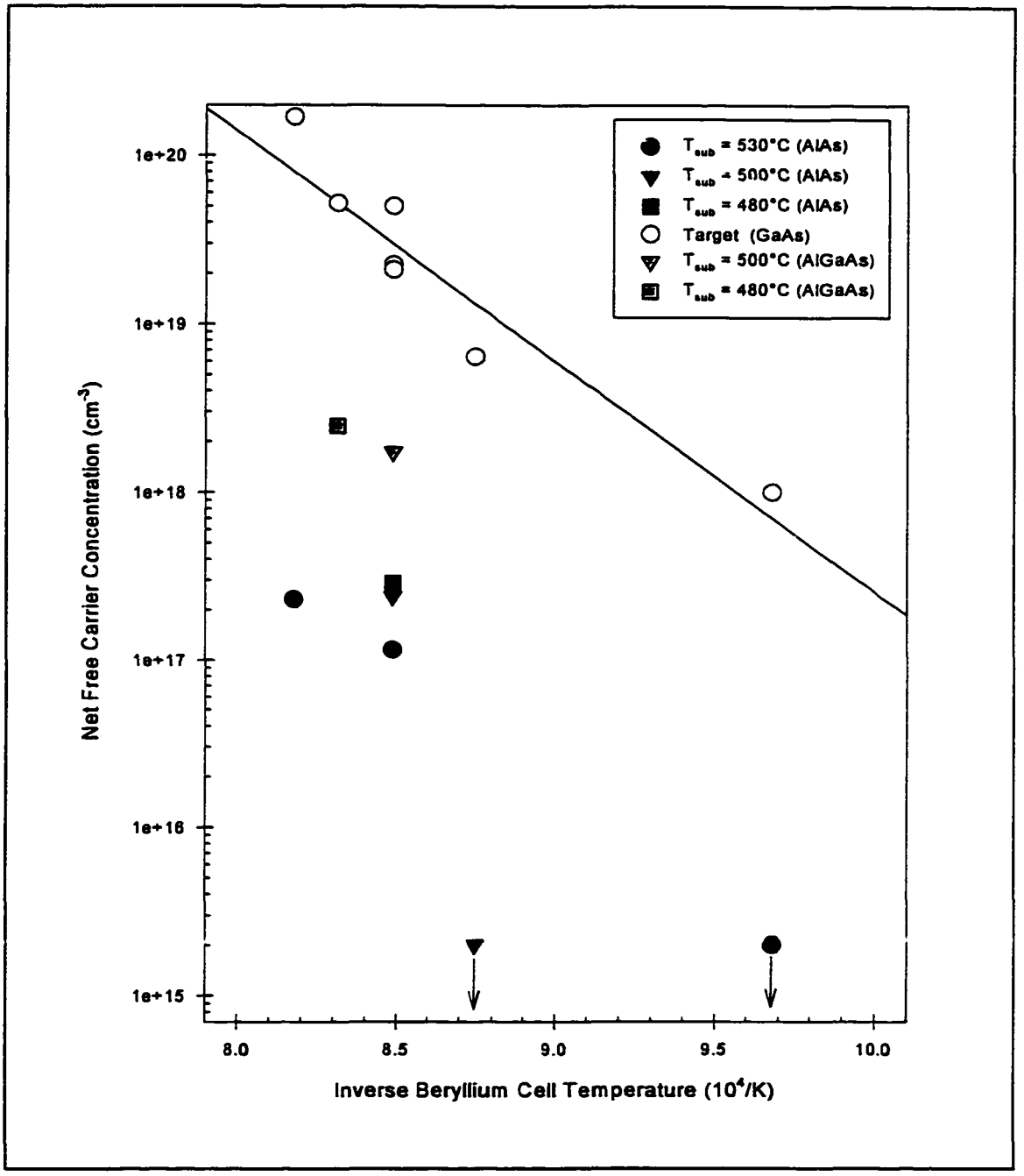

Figure 5.5 As-measured p-type AlGaAs net free carrier concentration as a function of inverse dopant cell temperature and of substrate temperature (T_{sub}). The solid symbols are AlAs samples, the shaded symbols are samples of $Al_{0.85}Ga_{0.15}As$, and the open symbols are the target values as measured in GaAs samples. The data points at 2.0×10^{15} cm^{-3} indicate measured films which were non-conducting.

5.2 AlGaInP Material Study

The first experiments performed in this work were the growth of DBRs using the AlGaInP material system. Preliminary AlInP/GaInP DBRs were designed, with center wavelengths in the visible spectrum, using refractive index values obtained from Tanaka *et al.* [10]. Tanaka *et al.* curve fit the theoretical expression for the refractive index from a single effective oscillator model [11] to experimental AlGaInP refractive index data, and obtained composition dependent coefficients for use in the expression. The results of Tanaka *et al.* were used to calculate AlGaInP refractive indices for all values of xQ. The initial DBR growths were used to adjust the calculated optical constants by matching the measured reflectance to the calculated reflectance. Once the AlGaInP compositions were determined for optimum low band offset DBRs, as described in Chapter III, bulk quaternary samples were grown and tested to ensure control of the doping concentrations and electrical properties of the material system. This section discusses the results of these experiments on the AlGaInP epitaxial layers.

The first of the initial AlInP/GaInP DBR growths fell well short of the target center wavelength. As Figure 5.6 shows, the measured peak was at 614 nm while the target peak based on design simulation was 680 nm. In addition, the measured peak reflectance for the 24.5 period DBR was only 78%, compared to the 99% design value. This drastic reflectance shortfall was attributed to the fact that the wavelength of the measured peak was below that corresponding to the band gap of GaInP, meaning that every other layer of the DBR was absorbing the optical signal. After multiple trial DBRs fell short of the target peak, it was clear something in either the design or growth was in error.

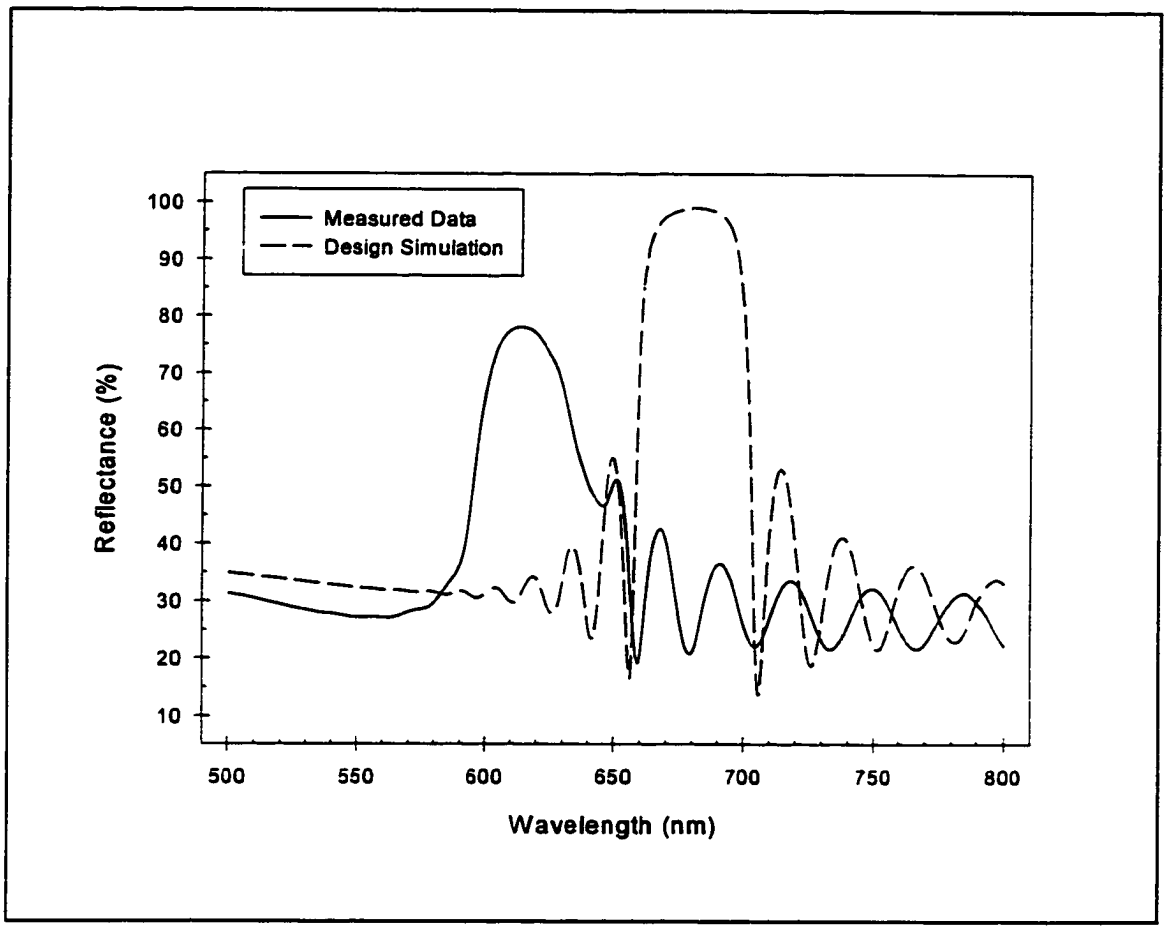

Figure 5.6 Measured and designed reflectance spectra for the initial 24.5 period AlInP/GaInP DBR growth.

The center DBR wavelength is dependent upon the layer thicknesses and the optical constants, so before concluding the error was in the optical constants the precision in the layer thickness needed to be determined. A Tencor Instruments Alpha Step 100 mechanical stylus profilometer was used to measure the total DBR structure thickness, and DCXD provided a measurement of the average superlattice period, both of which were compared with the expected DBR height and period. In addition, bulk GaInP or AlInP ternary calibration samples were grown the same day as the trial DBRs, and Alpha Step measurements provided a ternary growth rate used to set the growth time for one DBR layer.

So, from run to run reproducibility, one DBR layer thickness was known from calibration with an accuracy of about 1-2%. Then the thickness of the other layer was deduced from post-growth measurements of the average DBR period with an uncertainty of less than 2%.

With accurate layer thickness values, the optical constants were examined next. TFCalc, a commercial software tool which is described in more detail in the next section, was used to simulate the trial DBRs and adjust the refractive indices to fit measured reflectance spectra. After several trial DBR growths it was determined that the optical constants of the as-grown AlGaInP materials were about 5% smaller than the calculated values based on Tanaka *et al.* The percent adjustment was assumed to be constant with respect to wavelength, although this was not verified. The adjusted AlGaInP refractive index data was used throughout the rest of the project. DBR design and simulation with the new data proved to be a good match with measured results over the range of composition and thickness required for this project.

Several bulk AlGaInP epitaxial samples were grown throughout this work to calibrate the material composition and carrier concentration in the quaternary films. The structural diagram and description of these calibration samples were previously given in Figure 4.4 and Section 4.1, respectively. For the end point ternary alloys, GaInP and AlInP, the composition was found directly from DCXD measurements. In addition to DCXD, the quaternary films needed an independent measurement of the band gap energy, through room temperature photoluminescence (PL) experiments, to separate out the Al and Ga compositions. The net free carrier concentrations and carrier mobilities of these bulk layers were determined using the Hall-van der Pauw technique previously described in Chapter IV.

Table 5.1 Summary of bulk AlGaInP calibration growths.

Quaternary	Al Composition (xQ)		Type	Carrier Concentration (cm^{-3})		Mobility (cm^2/Vs)
	Target	Measured		Target	Measured	
AlGaInP	0.10	0.096	n	2.0×10^{19}	3.40×10^{18}	213
AlInP	0.52	0.51	n	2.0×10^{19}	3.51×10^{18}	34.7
AlGaInP	0.14	0.15	p	7.2×10^{18}	6.57×10^{18}	14.4
AlGaInP	0.44	--	p	2.0×10^{19}	4.57×10^{17}	11.7
AlInP	0.52	0.52	p	2.0×10^{19}	2.26×10^{17}	7.9

Table 5.1 summarizes the characterization of the bulk quaternary samples. As before, the target doping levels were the carrier concentrations measured in bulk layers of GaAs for the same growth rate and material flux from the dopant source cell. None of the quaternary films exhibited carrier concentrations equal to the target doping level, which is most likely due to mechanisms similar to those seen in AlGaAs. For the p-type beryllium, the ratio of free carriers to target dopants decreased as the Al content increases, again following the trend expected from increasing deep level traps due to the aluminum. For the n-type silicon dopant the ratio remained relatively unchanged with Al content at approximately 17%. In this case the cause is most likely associated with the mechanisms discussed in Section 5.1.2, such as differences in activation energy or pair compensation in AlGaInP as compared to GaAs.

From the data in Table 5.1, it is obvious that high enough carrier concentration levels, $2\times10^{18}\,cm^{-3}$ and greater, were obtained in the AlGaInP for use in both the n-type (xQ=0.10) and p-type (xQ=0.14) DBRs. So, combined with the results of the AlGaAs material study, the choice of optimum low band offset DBRs made in section 3.1.3 were confirmed.

However, the same cannot be said for the control DBRs with respect to the use of the AlInP materials in place of the AlGaAs layers. A sufficient concentration of carriers was obtained for n-type AlInP, but p-type AlInP had only $2.3\times10^{17}\,cm^{-3}$ carriers, even with a target doping level of $2\times10^{19}\,cm^{-3}$.

Following the example of p-type AlGaAs, an AlGaInP quaternary sample with xQ=0.44 was grown to see if the addition of gallium to the composition would significantly increase the measured hole concentration. Note in Table 5.1 that the exact composition could not be measured because no PL emission was detected from this indirect band gap material. The measured hole concentration doubled to $4.6\times10^{17}\,cm^{-3}$ compared to that of AlInP, but was still short of the desired level for the DBRs. However, since a better alternative was not available, the quaternary compound with xQ=0.44 was used as the low refractive index layer in the p-type control DBR instead of AlInP. This substitution means a smaller valence band offset in the control DBR than was used in the theoretical calculations of Chapter III, which should decrease the calculated resistance due to the barrier. However, since the carrier concentration is also lower, the width of the heterojunction barrier is larger and that should increase the barrier resistance. The lower carrier concentration also means the theoretical bulk resistance of the DBR would increase. Calculations show that this material substitution actually increases the theoretical DBR specific contact resistance of the p-type control DBR by about 3%, so it should still provide a good comparison with the low valence band offset DBR.

5.3 DBR Design and Growth

With all of the constituent semiconductor materials properly characterized, the two low band offset DBRs and their control DBR samples were designed and grown. This section details the structure of the DBRs needed to obtain greater than 99% reflectance at the peak wavelength of 650 nm. Also, some of the growth constraints, placed by the MBE system, and DBR growth calibrations are discussed.

As described in Chapter II, DBRs are designed using knowledge of the indices of refraction of the constituent materials. For AlGaInP the values from Tanaka *et al.* [10] were corrected using experimental results as described earlier in this chapter, and for AlGaAs data for this parameter was taken from Adachi [12]. All of the DBRs were designed and simulated using a commercial software tool called TFCalc [13]. TFCalc simulates the electromagnetic interaction of a thin film coating with an incident illuminant source by solving Maxwell's equations. The reflectance, transmittance, and absorptance, among other optical properties, can be computed for the coating by TFCalc. The thin film structure is modeled in one dimension, and is completely defined by the material composition and the thickness of each layer. Any material may be defined by providing TFCalc with the appropriate optical parameters, the refractive indices and the absorption coefficients, as a function of wavelength. Thus a DBR is simply defined by alternating the two material layers for the desired number of periods. The substrate material can also be included in the analysis. When simulating the reflectance, the results are given as a function of wavelength and either could be plotted within TFCalc or saved as a table in a data file.

The first step in the DBR design used Equation (2.2) to calculate the quarter wavelength thickness of each material layer. These results were used for the creation of the DBR structures in the TFCalc program. Analysis of the four DBRs under investigation revealed that 40 mirror periods would achieve 99% reflectance at 650 nm for each case. In addition, the high refractive index quaternary layer needed to be at the top of the DBR, forming the incident interface with the air, so that the phase of the reflection was correct and a maximum reflectance was obtained. When the order was reversed, placing the low index layer on top, the phase shift was destructive and a notch appeared in the DBR peak. Figure 5.7 demonstrates this effect of the layer order for a 20 period AlAs/AlGaInP (xQ=0.10) DBR

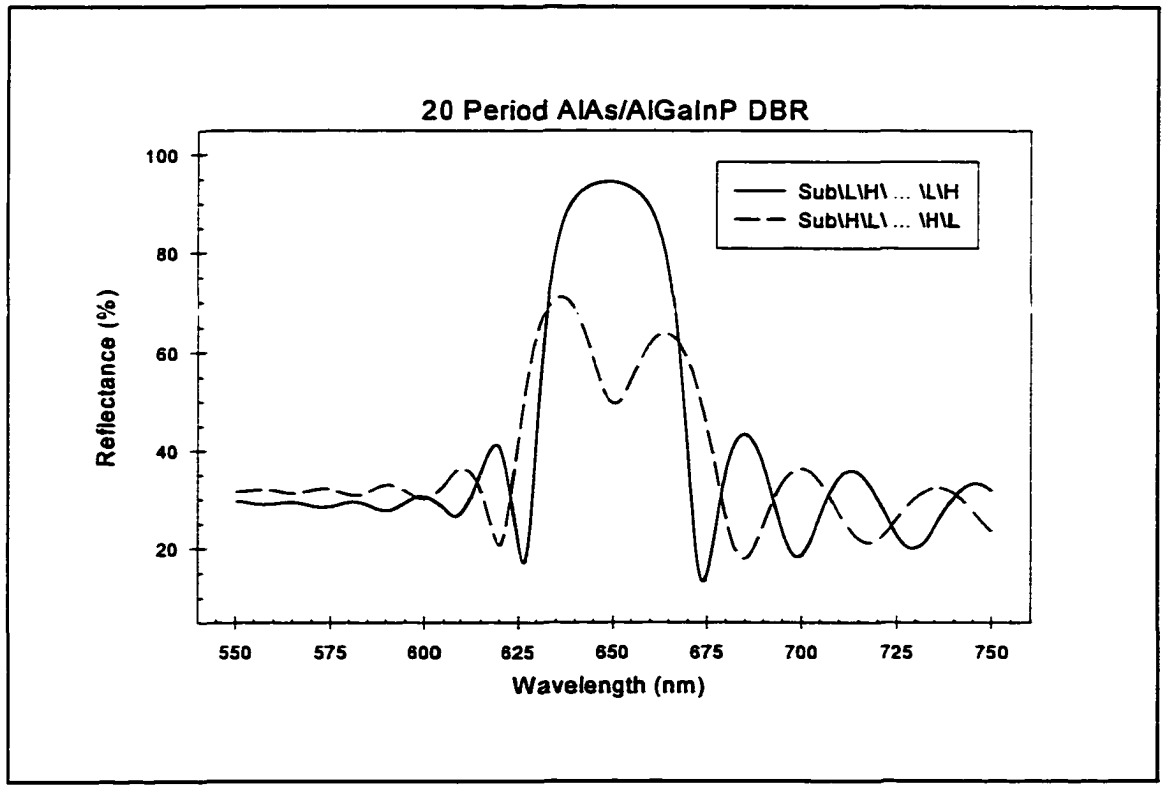

Figure 5.7 The order of the high (H) and low (L) refractive index layers has a dramatic effect on the reflectance of a 20 period AlAs/AlGaInP (xQ=0.10) DBR.

as calculated by TFCalc. As the number of periods increases the notch becomes less pronounced, but the decrease in reflectance remains. Thus all DBRs were designed and grown with a high index quaternary layer terminating the top of the DBR structure.

Table 5.2 summarizes the structural design of all four DBRs, including the number of periods and the quarter wavelength thickness of each layer. In the first column, the low index of refraction layer is listed first, and the high index layer is listed second. For the n-type DBRs, 40.5 periods were used beginning with a high index quaternary layer next to the substrate, alternating that with the low index ternary layer, and ending with a high index quaternary layer on top. The p-type DBRs were similarly designed with 40.5 periods, also beginning and ending with the high index quaternary layer. Note that in the table below the low band offset DBRs are the mixed arsenide and phosphide structures (the first and third ones listed), while the control samples (the second and fourth ones listed) are the all phosphide structures.

Table 5.2 Summary of structural design of each DBR.

DBR Materials (n_L / n_H)	Composition	Type	Number of Periods	d_L (Å)	d_H (Å)
AlGaAs/AlGaInP (low offset DBR)	xT=0.90/xQ=0.14	p	40.5	510	488
AlGaInP/AlGaInP (control sample)	xQ=0.44/0.14	p	40.5	517	488
AlAs/AlGaInP (low offset DBR)	xQ=0.10	n	40.5	522	484
AlInP/AlGaInP (control sample)	xQ=0.52/0.10	n	40.5	524	484

One characteristic in the design of all four structures that was not mentioned in Table 5.2 was the addition of a 100 Å GaAs cap layer on top of the DBRs. The cap was heavily doped to facilitate improved electrical contact when evaporating metal onto the processed structure for the electrical measurements. For the experiments described in Section V.4, the GaAs cap layer was removed from a piece of each as-grown sample so that the cap did not affect the proper evaluation of the quality of each DBR. For the determination of the specific contact resistances as described in Section V.5, pieces of each sample with the cap layer remaining were taken through the process steps.

The actual growth of each of the DBRs was more complicated than simply laying down alternating layers of materials. The difficulty centered on the fact that aluminum was used in both DBR layers, and that there was only one Al source cell available in the GSMBE system. Due to constraints of phosphorous gas flow and material quality, the maximum AlGaInP growth rate was fixed at 1.0 μm/hr. At this rate the Al flux was approximately equivalent to an AlAs growth rate of 0.1 μm/hr and 0.14 μm/hr for the n-type and p-type DBR high index layers, respectively. Using such a constant, low Al flux rate throughout the structure would be impractical in the CSU MBE laboratory since it would take approximately 30 minutes to grow a single AlGaAs layer, or over 20 hours to grow a 40 period DBR. On the other hand, from Figure 5.2, the growth rate of the low index AlGaAs layers was limited to a maximum of about 0.4 μm/hr. Any faster and the quality of the material degraded. So in order to balance growth rates between maximizing material quality and minimizing growth time, the Al cell temperature was ramped up and down once each period to provide the fluxes necessary for each layer.

The temperature ramping scheme was demonstrated in Figure 4.7 for a p-type AlGaAs/AlGaInP DBR. Precise control of the Al flux was most critical for the high index quaternary layers, where the flux must be constant and accurate in order to obtain the correct composition. A ramping study of the Al cell showed that a one minute ramp, from a flux equivalent to 0.4 μm/hr down to around a 0.1 μm/hr equivalent flux, followed by a three minute soak was sufficient to allow the Al cell to reach a steady thermocouple temperature, and presumably a steady Al flux, for growth of the quaternary layer. Since it was undesirable to stop growth for extended periods of time, the cell ramp down took place during the growth of the AlGaAs layers. Fortunately, the primary concern in the AlGaAs layers was the thickness as opposed to the composition. For the p-type DBR of Figure 4.7, the Ga#1 and Be cells were ramped down simultaneously with the Al cell to provide an approximately constant AlGaAs composition and doping level. As long as the ternary composition was near xT=0.9, the DBR would still have a low valence band offset. For the n-type AlAs/AlGaInP the ramping was less complex. Since the binary composition of the AlAs was assured, only the Si cell was ramped along with the Al cell in order to provide an approximately constant doping level. At the end of the quaternary layers, the cells were ramped up to the fluxes required for the AlGaAs layers during the 30 second growth pause, as was described in Chapter IV.

The most critical part of ramping the cells during the AlGaAs layers was adjusting the growth time of the low index layer to obtain the proper quarter wavelength thickness. The growth rates were steady at the start, 0.4 μm/hr, and at the end, 0.1 μm/hr or 0.15 μm/hr depending on whether the mirror was n-type or p-type, of each AlGaAs layer. Also, the one

minute ramp down was approximated as a linearly varying growth rate, thus theoretically setting the AlGaAs growth time. However, due to the nature of the effusion cells, the flux varied as the cells settled to their steady state set points. This caused an uncertainty in the growth time which could have a serious impact on the accuracy of the AlGaAs layer thickness and thus on the reflectance spectrum of the DBR.

To obtain a more accurate total AlGaAs growth time, two calibration DBRs were grown: one intentionally overshooting the thickness required for the 650 nm peak target wavelength, and the other deliberately below the target. In all other respects, such as material composition and quaternary layer thickness, the two calibration DBRs were identical. Changing the AlGaAs layer thickness was accomplished by keeping the ramp time and the low flux growth time constant, and varying the high flux growth time. The variation was approximately three quarters of a minute on either side of the theoretically correct time, which corresponded to approximately a 25 nm shift in the peak wavelength from its target. Figure 5.8(a) shows the reflectance spectra for two p-type AlGaAs/AlGaInP (xT=0.9/ xQ=0.14) calibration samples. MBE1129 was grown with too short of a high flux growth time, and the corresponding time for MBE1133 was too long. Since the only difference between the two DBRs was the AlGaAs layer thickness, it was assumed that the peak wavelength was linearly proportional to the AlGaAs growth time, which controls the layer thickness. In Figure 5.8(b) the peak wavelengths were plotted as a function of the high flux growth time. A straight line was drawn between the points, and the time required to obtain a peak wavelength of 650 nm was determined. A similar process was done to calibrate the AlAs layer growth time for the low conduction band offset n-type DBR.

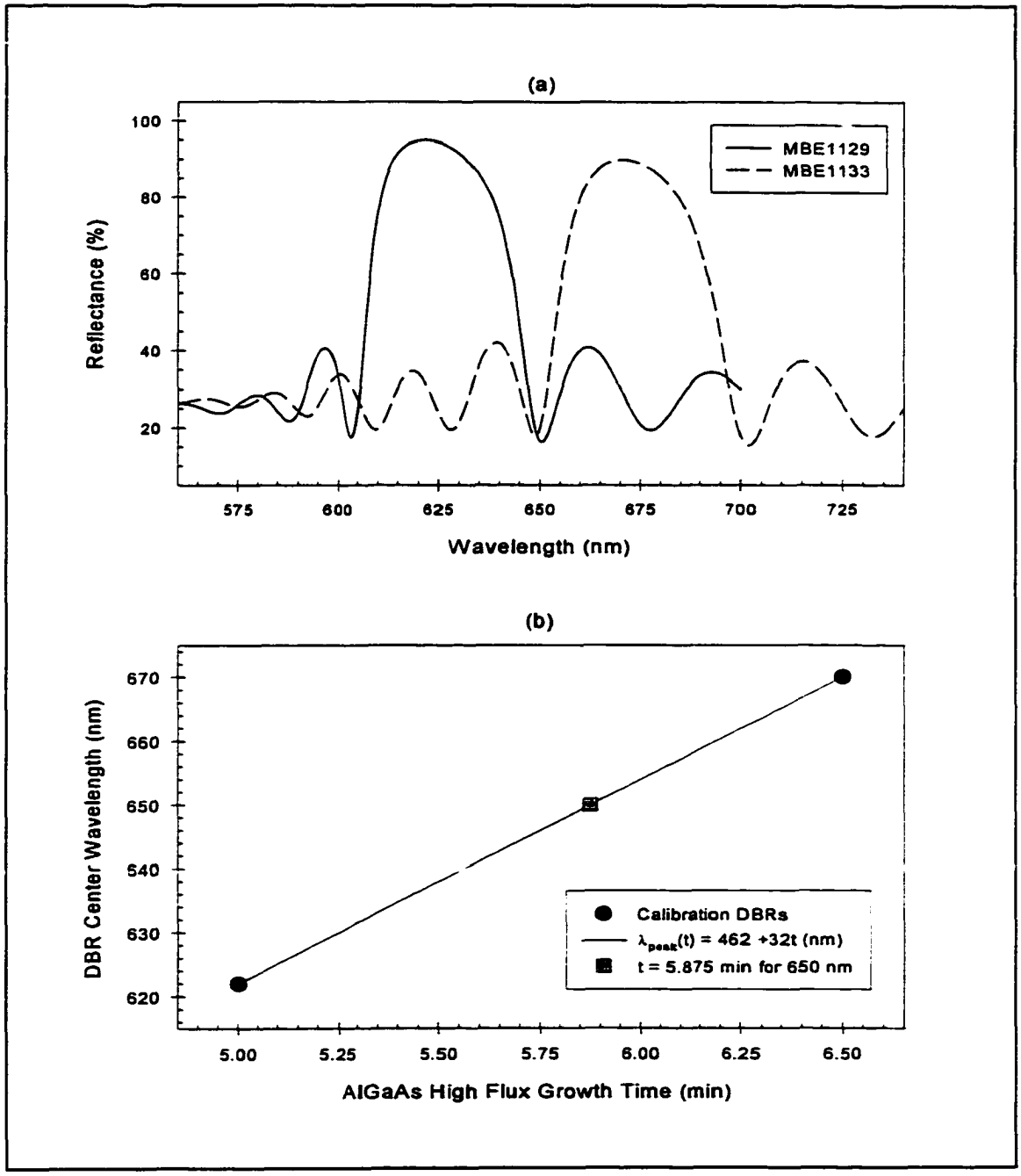

Figure 5.8 P-type AlGaAs/AlGaInP DBR growth time calibration: (a) measured reflectance spectra; (b) determination of the high flux growth time to achieve a target peak wavelength of 650 nm.

5.4 DBR Structural Characterization

With the DBR structures designed and their growths calibrated, the two low band offset mirrors and their corresponding control samples were grown via GSMBE. This section evaluates the structural quality of the DBRs. Reflectance and double crystal x-ray diffraction (DCXD) measurements were used to characterize the structures. DCXD spectra indicated the crystal quality of the semiconductor films, and were used to determine the average DBR superlattice period. Comparison of the measured reflectance spectra with the design targets and simulations indicated the optical quality of the DBR structures.

5.4.1 P-Type DBRs

After the growth of the calibration mirrors, the two p-type DBRs were grown. The low valence band offset AlGaAs/AlGaInP DBR was designated MBE1136, and the AlGaInP/AlGaInP control sample was MBE1139. As specified, the high index AlGaInP quaternary layer common to both samples contained 14% aluminum, while the low index AlGaAs and AlGaInP layers had 90% and 44% aluminum, respectively. Both DBRs consisted of 40.5 periods, starting and terminating with the common quaternary layer. The as-grown surface of each sample was smooth and mirror like, and the color of both samples was red, which was expected from the peak reflection target wavelength of 650 nm.

Figure 5.9 shows the measured and simulated DCXD spectra for MBE1136, the low valence band offset DBR. As on each DCXD plot in this section, the angular position of the high intensity peak associated with the GaAs substrate has been normalized to zero arcseconds (0"). Looking at the simulation, the spectrum of a high quality, uniform

superlattice contains a series of well defined, evenly spaced peaks. The central superlattice peak, which is often the largest in amplitude but not in this case, is labeled n=0. From the angular difference between the n=0 and the substrate peaks, the average superlattice mismatch can be calculated as described in Chapter IV. The other superlattice satellite peaks are ordered from the central one and labeled n = ±1, ±2, and so on while moving away from the center peak; only the first five peaks are labeled in the figure. The angular separation, $\Delta\theta$, between any two adjacent satellite peaks is related to the superlattice period, d_{SL}, by [14]

$$d_{SL} = \frac{\lambda \sin(\theta_B)}{\Delta\theta \sin(2\theta_B)} \tag{5.2}$$

where λ is the wavelength of the x-ray radiation, θ_B is the Bragg angle, and $\Delta\theta$ must be in radians. The measured separation between adjacent peaks may vary, but by using an average $\Delta\theta$ in Equation (5.2) DCXD provides a value for the average superlattice period.

The measured DCXD spectrum of Figure 5.9 indicated that the DBR was a high quality superlattice. The superlattice peaks were all sharp and narrow, just as expected from the simulation. From the average superlattice peak separation, 193.8", the average DBR period was found to be 978 Å, or 20 Å short of the target period, which was the sum of the two individual layer thicknesses as given in Table 5.2. The n=0 peak was only 84" to the left of the GaAs substrate peak, and corresponded to a lattice mismatch of 625 ppm as calculated using the equations of Table 4.1. Since the thickness of the DBR was composed of approximately half AlGaInP and half AlGaAs, the lattice mismatch of the n=0 peak was essentially the average of the mismatch of the two individual materials with respect to the

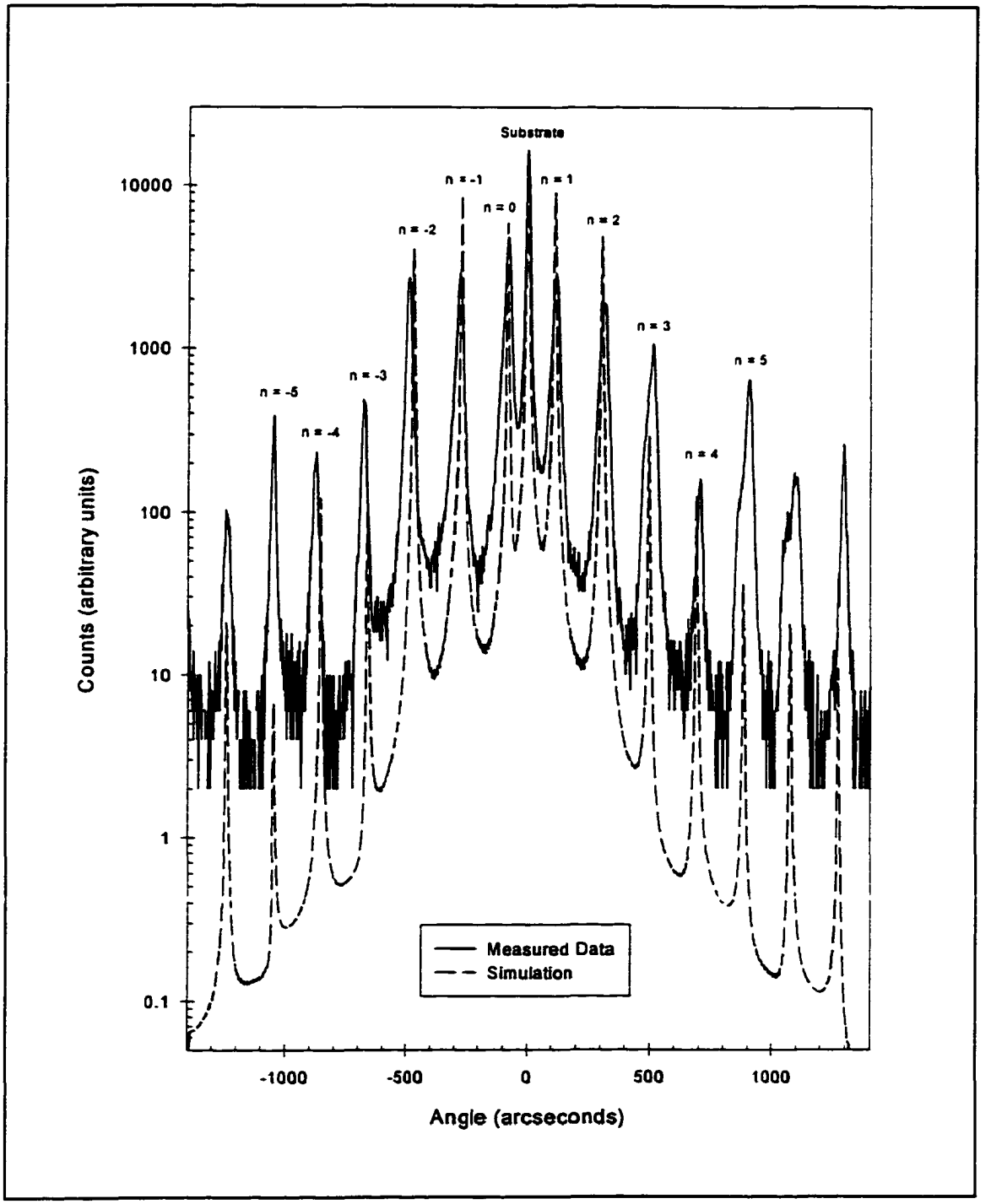

Figure 5.9 Measured and simulated DCXD spectra for MBE1136, the low valence band offset AlGaAs/AlGaInP DBR.

GaAs substrate, assuming each material was of uniform composition throughout the entire DBR structure. Since the experimental mismatch of $Al_{0.9}Ga_{0.1}As$ was approximately 1250 ppm, the above n=0 mismatch implied that the quaternary layer was nearly lattice matched with the substrate. The x-ray simulation in Figure 5.9 used a 982 Å period, the above ternary mismatch, and an $Al_{0.145}Ga_{0.38}In_{0.475}P$ quaternary composition, which is indeed nearly lattice matched. The resulting correlation between simulation and measurement was very good, meaning that the as-grown structure was very uniform. Note that more satellite peaks were observed than are shown in the plot; 15 peaks were counted on either side of n=0 over a range of 6000", which was the total sweep of the measurement. Thus the crystal quality of MBE1136 was extremely high.

Figure 5.10 shows the measured and simulated reflectance spectra for MBE1136. The central peak had a measured reflectance of 99.5% at 637 nm with a FWHM of 35 nm, while the simulation had a 99.3% peak at 646 nm and a 28 nm FWHM. The TFCalc simulation used the target period of 998 Å. The measured sideband peaks in either direction from the central peak were nearly in phase with the simulation. The only real discrepancy between the spectra was the asymmetry of the measured central peak. The peak was not uniform with a nearly flat maximum reflectance band as in the simulation, but instead had a sloped central band. Also, the first sideband peak on the low wavelength side was washed out and nearly indistinguishable. Modification of the simulation to include nonuniform layer compositions and thicknesses throughout the DBR structure could alter the position and strength of the central peak, as well as the shape and strength of the sideband peaks, but was unsuccessful in reproducing the asymmetry of the central reflectance peak.

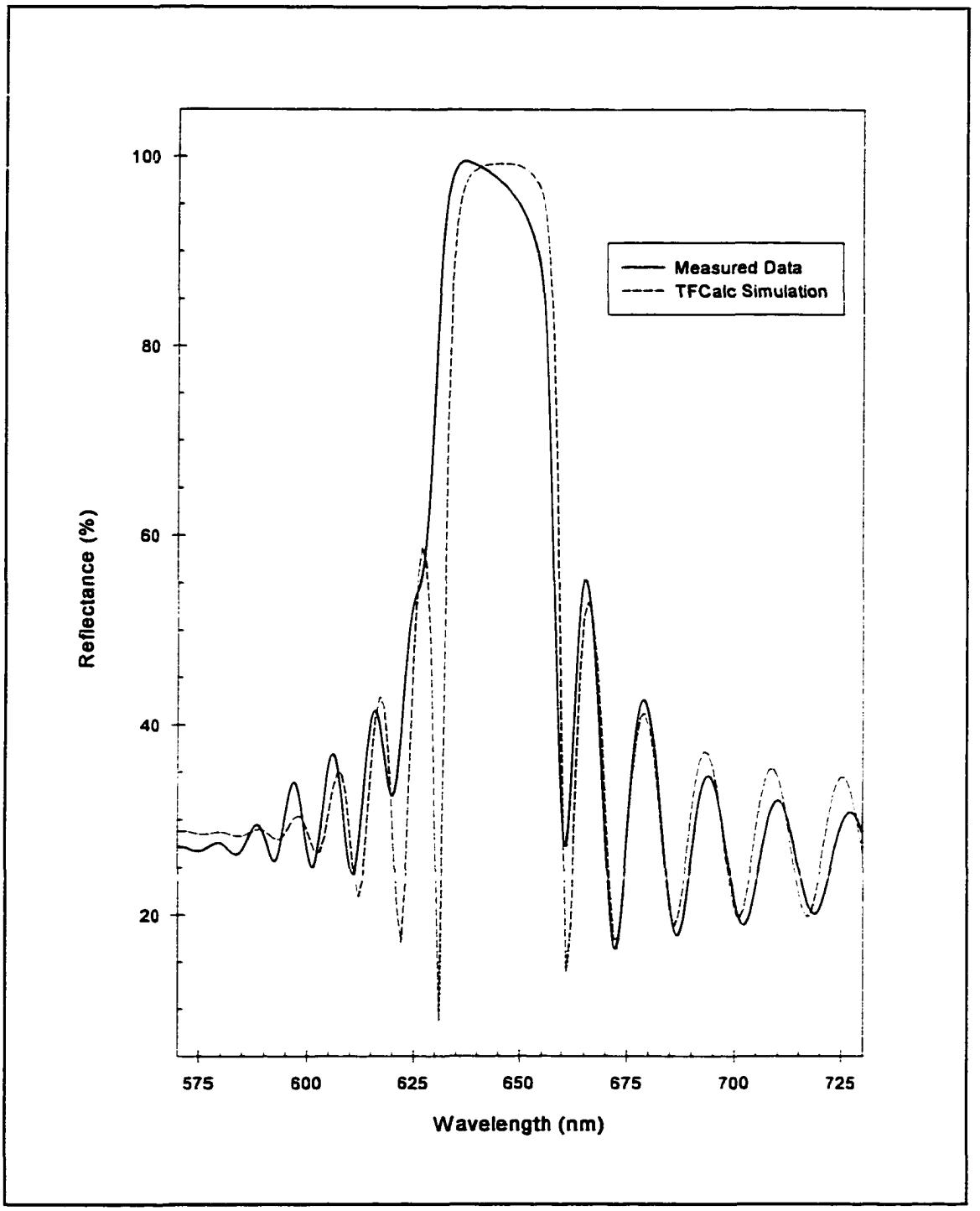

Figure 5.10 Measured and simulated reflectance spectra for MBE1136, the p-type AlGaAs/AlGaInP low valence band offset DBR.

Figure 5.11 shows (a) the reflectance spectra and (b) the DCXD spectra for the p-type AlGaInP/AlGaInP (xQ=0.44/0.14) control DBR, MBE1139. In Figure 5.11(a), the peak of the measured reflectance spectrum was well short of the target design simulation. The measured peak was 98.5% at 629 nm with a 33 nm FWHM, while the target was 98.6% at 649 nm with a 25 nm FWHM. The measured central peak again showed a sloped asymmetry which could not be duplicated by simulation. Also, the first sideband peak on the lower wavelength side was nearly washed out, although not as much as observed in MBE1136. The post growth TFCalc reflectance simulation, also shown in Figure 5.11(a), used a period of 970 Å and refractive index data for the compositions of the targeted layers, and a better match was found with the measured spectrum.

In Figure 5.11(b), the measured x-ray spectrum of MBE1139 showed only a few, broad satellite peaks, in stark contrast to Figure 5.9 for MBE1136. Using the peaks available, the average separation was found to be 193.1", corresponding to a DBR period of 981 Å which was short of the 1005 Å target period. The DCXD simulation used a 991 Å period and $Al_{0.145}Ga_{0.38}In_{0.475}P/Al_{0.44}Ga_{0.08}In_{0.48}P$ material layers to match the peak positions. It also supported the absence of satellite peaks at positions less than the n=-1 peak, and followed the weakening of peaks in the opposite direction. However, the simple structure of the simulation could not imitate the broadening seen in the measured peaks. Alpha step measurements determined an average DBR period of 963 Å, and agreed with both the x-ray and TFCalc reflectance simulations that showed the thickness of the as-grown structure for MBE1139 was short of the design thickness.

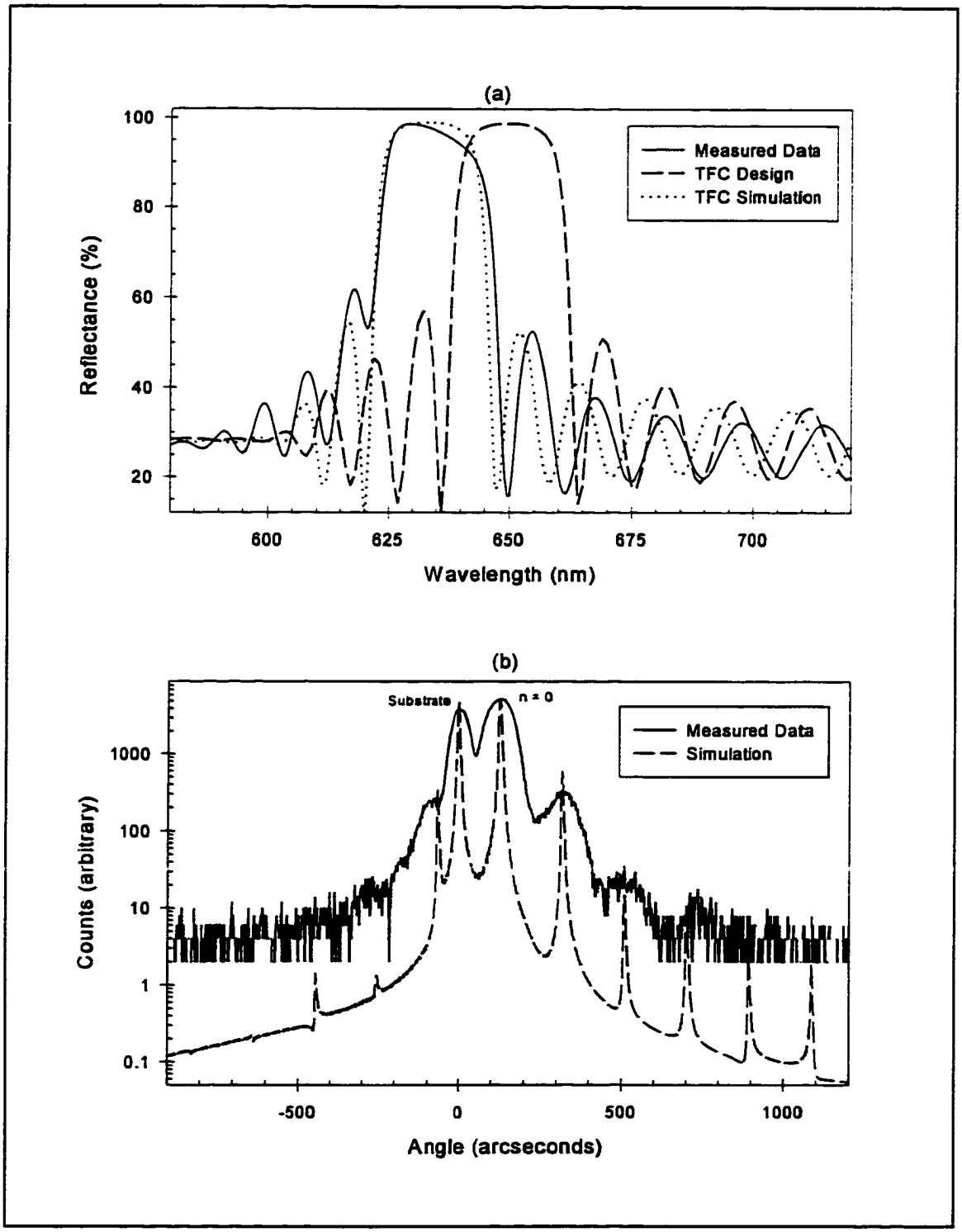

Figure 5.11 Measured and simulated (a) reflectance and (b) DCXD spectra for MBE1139, the AlGaInP/AlGaInP (xQ=0.44/0/14) p-type control DBR.

In summary, the p-type DBR structures did not turn out ideally. The DBR period for each of the as-grown samples was short of the design target, causing the reflectance peak to occur at wavelengths somewhat less than the 650 nm target. There was also evidence that the semiconductor alloy layers were nonuniform in composition or thicknesses or both throughout the DBR structure. This could cause the washing out of the first low wavelength sideband peak in the reflectance spectrum, and also could cause the broadening of the peaks in the DCXD spectrum. The effect was much more severe in the control sample, MBE1139, than in the low valence band offset DBR, MBE1136, especially in the measured DCXD spectrum.

However, these imperfections in the structural qualities of the p-type DBRs did not prevent their electrical measurement and the evaluation of their specific contact resistance values. The structural consistency, in terms of the number of layers and the heterojunction interfaces and in terms of the relative quality of the crystal structure, between the low valence band offset DBR and the control sample allows for a meaningful comparison of their respective specific contact resistance measurements. Thus any differences in these determined resistance values could be attributed to the choice of semiconductor material layers, and thus to their differences in valence band offset values, rather than being caused by any stark differences in their MBE growths or in the crystal quality of their DBR structures.

5.4.2 N-type DBRs

Right after the growth of the p-type DBRs, the two n-type DBR samples were grown. The low conduction band offset AlAs/AlGaInP DBR was designated MBE1140, and the AlInP/AlGaInP n-type control sample was MBE1141. The high index of refraction AlGaInP layer common to both samples contained 10% aluminum, and both DBRs started and terminated with this common quaternary layer. The as-grown samples had smooth, mirror like surfaces, and the color of each was red as expected from the peak reflection target wavelength of 650 nm.

Figure 5.12 shows the (a) reflectance and (b) x-ray spectra for the 40.5 period low band offset sample, MBE1140. Both graphs contained characteristics typical of nonuniform structures similar to those seen in the p-type DBRs. The reflectance spectrum had the asymmetric central peak and somewhat washed out lower wavelength sideband peak, with that first minimum having a much higher reflectance than predicted. In the measured DCXD spectrum, each superlattice peak was actually a double peak, and they were broader than simulation. All of this indicated a nonuniform DBR structure.

The reflectance spectrum in Figure 5.12(a) shows a much broader measured central peak for MBE1140 than any TFCalc simulation could attain. The measured peak reflectance was 100% at 656 nm with a 47 nm FWHM, while the simulation had 99.6% peak reflectance at 659 nm and a 30 nm FWHM. The simulation imitated the short wavelength fall off edges of the central peak and the first short wavelength sideband peak. However, the simulation was not able to match the FWHM of the central peak or the positions of the other sideband peaks. In fact, the measured central peak seemed to engulf the first simulated sideband peak

on the long wavelength side. The DBR period of the uniform structure in the simulation was 1027 Å, or about 2% larger than the 1006 Å target thickness. The larger simulation period correlated with the fact that the position of the measured central peak was at a longer wavelength than the 650 nm target. By using a complicated nonuniform structure in the TFCalc simulation the sideband peaks could be adjusted to more closely follow the measured spectra, but the width and shape of the central peak could not be duplicated.

The measured DCXD spectrum of MBE1140, Figure 5.12(b), showed multiple strong satellite peaks on either side of the central n=0 peak, despite the fact that their double peak characteristic was indicative of a nonuniform structure. The substrate and n=0 superlattice peaks were perfectly overlapped, meaning the quaternary layer mismatch exactly compensated the AlAs mismatch to give zero average mismatch for the overall DBR structure. From the average separation of the satellite peaks, 185.4", the average DBR period calculated from x-ray was 1022 Å. The simulation used $Al_{0.10}Ga_{0.4276}In_{0.4724}P$ quaternary layers, which included more gallium than the target composition of $Al_{0.10}Ga_{0.416}In_{0.484}P$, to balance the AlAs mismatch and place the n=0 peak on top of the substrate peak. The period used in the simulation was 1023 Å.

In addition, the average DBR period measured by the alpha step profilometer was 1037 Å, compared to 1022 Å from x-ray and 1027 Å from reflectance evaluations. Each of these experimental measurements determined a DBR period larger than the 1006 Å target value. This consistency between the various measurement techniques helped reaffirm the reliability of the data.

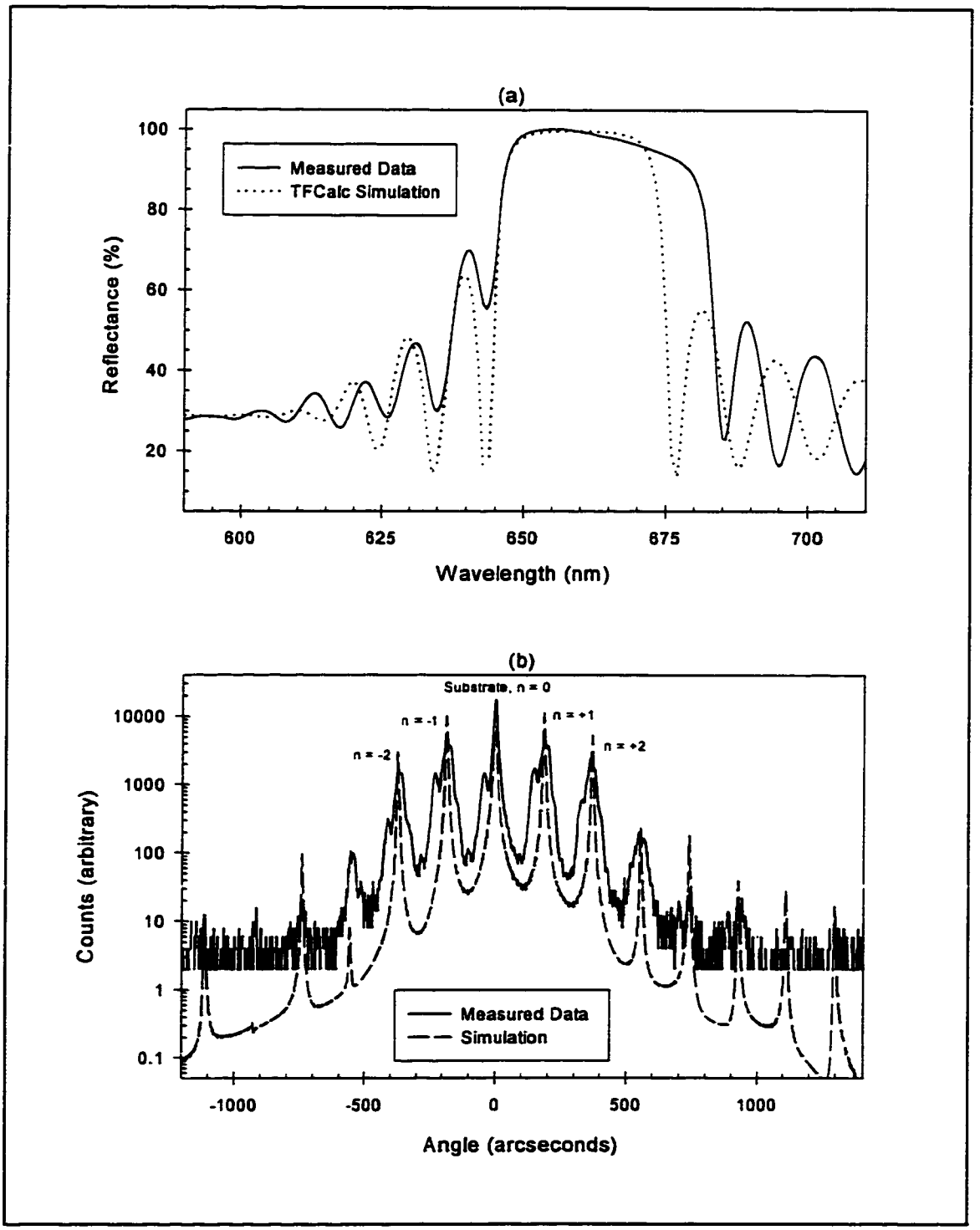

Figure 5.12 Measured and simulated (a) reflectance and (b) DCXD spectra for MBE1140, the low band offset AlAs/AlGaInP (xQ=0.1) n-type DBR.

The measured and simulated reflectance and DCXD spectra for the final DBR structure, the n-type control sample MBE1141, are shown in Figure 5.13 (a) and (b), respectively. The spectra were very similar to those of the previous samples. One major difference between MBE1141 and the other DBRs was the premature termination of the growth due to a power failure in the engineering building. The growth was cut off during the quaternary layer of the 37th period, so instead of a complete 40.5 period DBR, the mirror actually consisted of 36 full AlInP/AlGaInP (xQ=0.52/0.10) periods plus an AlGaInP "cap" layer approximately 300 Å thick. The measured alpha step thickness gave an average DBR period of approximately 978 Å, which was short of the 1008 Å target for the structure.

The reflectance spectra in Figure 5.13(a) were unusual compared to the previous samples in the sense that the simulated FWHM of 30 nm was nearly identical to the 31 nm measured value. The TFCalc simulation used 36 uniform AlInP/AlGaInP periods each 974 Å thick, and a 300 Å quaternary cap layer. The measured and simulated spectra both had central peak reflectance values of 99.5%, located at 628 nm and 632 nm, respectively. The different peak locations, while also having the width of the simulated peak fall nearly on top of the measured peak, was due to the asymmetry of the measure peak. Looking at the sidebands, the first peak to the short wavelength side was again washed out in the measured spectrum, and the simulated sideband peaks were out of phase with the measured peaks.

The measured x-ray spectrum of MBE1141, Figure 5.13(b), also showed multiple strong satellite peaks on either side of the n=0 peak for this n-type control DBR. The average measured peak separation, 204.1", gave an average DBR period, 928 Å, that was much shorter than either value determined by alpha step or by reflectance, but all three

experimental values were consistently less than the target period thickness. The x-ray simulation matched the location and relative intensities of the measured satellite peaks by using a uniform 36 period DBR with 929 Å thick period and by including a 300 Å quaternary cap layer. The quaternary composition in the simulation was $Al_{0.10}Ga_{0.4275}In_{0.4725}P$, which was nearly the same as used in the simulation of MBE1140, and the AlInP layer mismatch was -325 ppm. The simulated satellite peaks were much narrower than the measured peaks, which may be due to nonuniform properties of the as-grown structure.

In summary, the two n-type DBR structures were very similar to their p-type counterparts. There was evidence of possible nonuniform thickness and/or composition of the material layers throughout each DBR structure. This could cause the washing out of the first short wavelength sideband peak in the reflectance spectra, and also cause the broadening of the peaks in the DCXD spectra. There was also the consistent asymmetry of the central reflectance peak, for which a readily evident cause was not found. The average error between the measured peak reflectance wavelength and the 650 nm target was 2.4% for the four DBR samples, which was within the run to run reproducibility of the MBE growth. As stated before, these imperfections in the structural qualities of the DBR did not preclude the accurate evaluation of their electrical resistance measurements. The deviations in layer thickness and alloy composition from the target values were not large enough to prevent a meaningful comparison of specific contact resistance values for DBRs with different heterojunctions. The DCXD and reflectance measurements confirmed the high quality of each sample, and ruled out any problems with their growth before continuing with the determination and comparison of the specific contact resistance values.

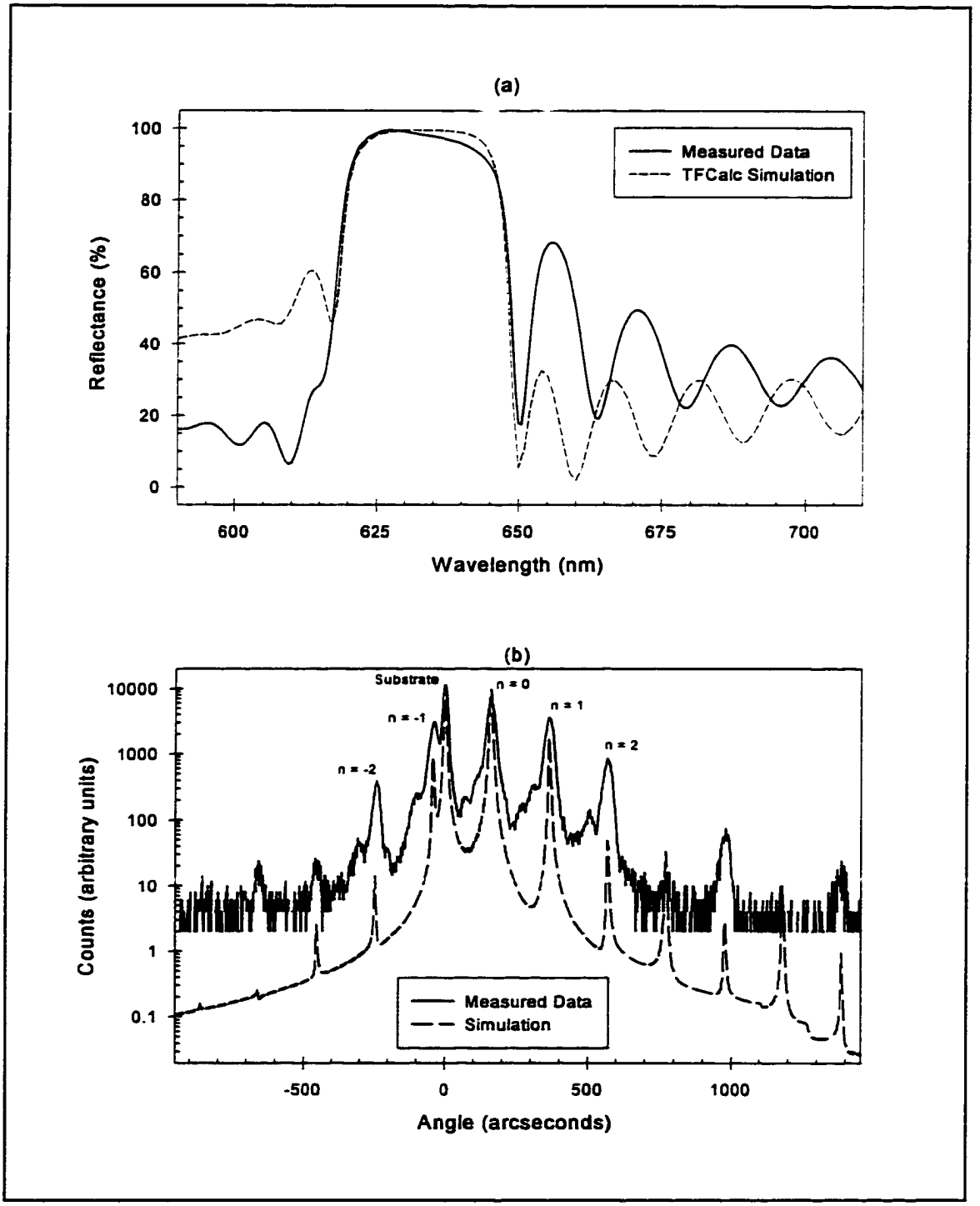

Figure 5.13 Measured and simulated (a) reflectance and (b) DCXD spectra for MBE1141, the AlInP/AlGaInP (xQ=0.52/0.10) n-type control DBR.

5.5 TLM Measurements

The final section of this chapter presents the results of the Transmission Line Model (TLM) measurements and specific contact resistance (ρ_c) calculations for the four DBR samples. Multiple pieces of all four DBR samples were taken through the full TLM fabrication process, as described in Chapter IV and Appendix A, and measurements. The measured ρ_c values for the two low band offset DBRs were within experimental error of the theoretical values, which were determined in Chapter III and summarized in Table 3.3. However, the measured values for the two control samples were not close to their corresponding theoretical values. Possible mechanisms and structural problems will be presented and discussed in an attempt to correlate the measured data with the theory for the control samples. It will be shown that a single effect can explain these differences in both the p-type and n-type control samples.

5.5.1 Specific Contact Resistance Data

Tables 5.3 through 5.6 present the measured specific contact resistance data for all four DBRs. Table 5.3 gives the ρ_c data for MBE1136, the low valence band offset p-type DBR. At the bottom of the table, the average ρ_c values are given along with the standard deviation (σ) of the data in each column. For each column the specific contact resistance was expressed as an average value, plus or minus experimental error, which was taken to be σ. As discussed in Chapter IV, the specific contact resistance for the DBR stack itself, ρ_c(DBR), is the difference between the values determined for the mesa geometry, ρ_c(mesa), and the stripe geometry, ρ_c(stripe), for a given contact size. Even though ρ_c(DBR) is a difference of

two experimentally determined values, its uncertainty or error is not the difference in the errors of the two values, but rather it is the sum of the errors. Thus ρ_c(DBR) can be expressed as

$$\rho_c(DBR)=[\rho_c(mesa)-\rho_c(stripe)]\pm(\sigma_m+\sigma_s) \qquad (5.3)$$

where $\sigma_{m,s}$ represent the errors in the mesa and stripe ρ_c values, respectively.

Table 5.3 Measured specific contact resistance data for MBE1136, the low valence band offset p-type AlGaAs/AlGaInP DBR.

Contact Size (μm):	100x100	100x100	50x100	50x100
Structure Type:	Mesa	Stripe	Mesa	Stripe
ρ_c (Ω·cm^2):	1.7902E-03	1.3796E-03	1.4781E-03	1.2002E-03
	1.7956E-03	1.4023E-03	1.4702E-03	1.1862E-03
	1.8097E-03	1.4848E-03	1.4543E-03	1.2122E-03
	1.8007E-03	1.6163E-03	1.5438E-03	1.4327E-03
	1.7943E-03	1.5980E-03	1.5383E-03	1.4663E-03
	1.7903E-03	1.5636E-03	1.7832E-03	1.2673E-03
			1.6161E-03	
Average ρ_c:	1.7968E-03	1.5074E-03	1.5549E-03	1.2942E-03
# of data points:	6	6	7	6
Standard Deviation:	6.771E-06	9.230E-05	1.065E-04	1.131E-04

The first two columns of data in Table 5.3 are for the 100×100 μm contact via measurements. Typical measured resistances for this size contact were 30-40 Ω on this sample. Using Equation (5.3) gives ρ_c(DBR) = (2.89±1.00)×10^{-4} Ω·cm^2 for the 100×100 μm contacts. Looking at the last two columns for the 50×100 μm contact vias, where typical measured resistances were 50-60 Ω, the value for ρ_c(DBR) is (2.61±0.22)×10^{-4} Ω·cm^2. Note that for the smaller contact sizes available on the mask set, 25×25 μm and 10×20 μm, the

measured I-V curves were very non-linear and the ρ_c calculations were not valid. So for the low valence band offset DBR, MBE1136, the average ρ_c(DBR) value was $(2.75\pm1.60)\times10^{-4}$ $\Omega\cdot cm^2$. From Chapter III, Table 3.3, the theoretical value of ρ_c(DBR) was 2.30×10^{-4} $\Omega\cdot cm^2$ for this p-type DBR structure. Thus the theory was very close to the measured value and was within the experimental error.

Table 5.4 gives the specific contact resistance data for MBE1139, the p-type control DBR. For this sample the resistances were much higher than expected. For the TLM processed pieces the typical measured resistances using the 100×100 μm contacts were around 7 kΩ and 7 MΩ for the stripe and mesa geometries, respectively. All of the ρ_c calculations from the data were very questionable, and thus invalid. In an attempt to obtain better data, larger metal contacts were evaporated onto a plain, unprocessed piece of the sample. This was done using the third mask of the TLM mask set, so that the size of the contact pads and their separation distances were still known. The data in Table 5.4 is from this plain piece of MBE1139, and only gives the specific contact resistance of the metal with the DBR. For the three columns the overall ρ_c(stripe) average was $(2.95\pm0.88)\times10^{-2}$ $\Omega\cdot cm^2$.

The problem was how to obtain a value for ρ_c(DBR). From evaluating the data for the other DBR samples, it turned out that the ratio of ρ_c(mesa) to ρ_c(stripe) was approximately the same as the ratios of the raw measured resistances. For example, for the 100×100 μm contacts of MBE1136, the ρ_c ratio was 1.7968/1.5047, or 1.19, while the ratio was 1.21 for the typical resistance values. Applying this to MBE1139, the ratio of the typical resistance values was 7MΩ/7kΩ, or 1000. In order for the ρ_c ratio to be the same, the value of ρ_c(mesa) had to be about 1000 times that of ρ_c(stripe), or 30 $\Omega\cdot cm^2$. This meant the value

Table 5.4 Measured specific contact resistance data for MBE1139, the p-type control DBR.

Contact Size (μm):	100x150	100x100	100x100
Structure Type:	Plain	Plain	Plain
ρ_c (Ω·cm^2):	3.3646E-02	2.2585E-02	1.8169E-02
	2.6168E-02	1.8061E-02	1.8887E-02
	3.2200E-02	2.2742E-02	1.7621E-02
	4.6736E-02	2.1472E-02	2.3009E-02
	2.5970E-02	2.1320E-02	3.7305E-02
		2.3544E-02	3.7915E-02
		4.0318E-02	3.9378E-02
		3.8616E-02	3.7478E-02
			3.7827E-02
			3.7594E-02
Average ρ_c:	3.2944E-02	2.6082E-02	3.0518E-03
# of data points:	5	8	10
Standard Deviation:	7.561E-03	7.889E-05	9.174E-04

for ρ_c(DBR) was also approximately 30 Ω·cm^2, which was much larger than the theoretical 3.85×10^{-4} Ω·cm^2 value for this DBR structure as found in Table 3.3. Possible reasons for this large discrepancy between theory and measurement will be explored in the next section. Note that Table 3.3 has AlInP/AlGaInP (xQ=0.52/0.14) for the p-type control DBR, while MBE1139 is AlGaInP/AlGaInP (xQ=0.44/0.14). The need for the substitution of $Al_{0.44}Ga_{0.08}In_{0.48}P$ for $Al_{0.52}In_{0.48}P$ was discussed in Section 5.2, and as mentioned there it made a negligible difference on the theoretical resistance of the p-type control sample.

Table 5.5 shows the measured ρ_c data for the low conduction band offset n-type DBR, MBE1140. The data was from pieces that went through the complete TLM processing. Resistance values for regions on the die with the two larger area contacts were too small to provide meaningful data. So the table contains all of the ρ_c data for the 25×25

Table 5.5 Measured ρ_c data for MBE1140, the low conduction band offset n-type DBR.

Contact Size (μm):	25x25	25x25	10x20	10x20
Structure Type:	Mesa	Stripe	Mesa	Stripe
ρ_c (Ω·cm^2):	1.1945E-04	8.4621E-05	7.7133E-05	5.7150E-05
	1.1647E-04	8.3827E-05	7.7226E-05	5.6488E-05
	1.1854E-04	8.8714E-05	7.6583E-05	5.9431E-05
	1.1923E-04	1.0031E-04	8.2483E-05	5.8798E-05
	1.0409E-04	1.0152E-04	9.7778E-05	5.3140E-05
	1.0315E-04	1.0075E-04	1.0155E-04	3.8730E-05
	1.0267E-04	1.0260E-04	9.7174E-05	5.1783E-05
	1.1559E-04	8.3920E-05	1.0422E-04	5.2115E-05
	1.1274E-04	1.0910E-04		7.0699E-05
	1.2052E-04	9.2903E-05		7.5152E-05
	1.0300E-04	9.1766E-05		8.1458E-05
	1.0392E-04	9.7382E-05		6.1607E-05
	1.1083E-04	9.7576E-05		5.9075E-05
	1.1705E-04	9.6422E-05		5.9817E-05
	1.1788E-04	8.5194E-05		
	1.2181E-04	8.1226E-05		
	1.1795E-04	8.2707E-05		
	1.2733E-04	9.0980E-05		
	1.1809E-04	9.1380E-05		
	1.2472E-04	8.5858E-05		
	1.2503E-04	1.0535E-04		
	1.2502E-04	1.0121E-04		
	1.2708E-04	1.0361E-04		
		9.6081E-05		
		8.6196E-05		
		8.5832E-05		
		8.5365E-05		
		1.2362E-04		
Average ρ_c:	1.1618E-04	9.4144E-05	8.9268E-05	5.9675E-05
# of data points:	23	28	8	14
Standard Deviation:	7.864E-06	9.651E-06	1.123E-05	1.021E-05

μm and 10×20 μm contacts, which yielded typical measured resistance values of 35 Ω and 75 Ω, respectively. From the data the average value for ρ_c(DBR) was (2.58±1.95)×10^{-5} Ω·cm^2, which was within experimental error of the 1.20×10^{-5} Ω·cm^2 theoretical value as seen in Table 3.3 for the low conduction band offset DBR.

Table 5.6 shows the measured ρ_c data for MBE1141, the n-type control DBR. Again the data was from pieces that went through the complete TLM processing and measured on the 25×25 μm and 10×20 μm contacts. Typical measured resistance values were 20 Ω for the former and 45 Ω for the latter contact size. Looking at the table, the measured ρ_c(mesa) and ρ_c(stripe) data were less than that of the other three samples and pushed the limit of the measurement capabilities of the mask design. The average ρ_c(mesa) and ρ_c(stripe) values were comparable to one another with standard deviations such that ρ_c(DBR) ranged from nearly 1×10^{-5} Ω·cm^2 to negative values. From the data the average value for ρ_c(DBR) was (5±4)×10^{-6} Ω·cm^2 for the n-type control DBR. This was an order of magnitude smaller than the 7.53×10^{-5} Ω·cm^2 theoretical value.

All of the specific contact resistance values, both experimental and theoretical, are summarized in Table 5.7. Both the p-type and n-type low band offset DBRs gave experimental ρ_c within measurement accuracy of the theoretical values, so these structures performed as expected. On the other hand, the control samples gave ρ_c values orders of magnitudes away from the theoretical numbers. For the p-type control DBR the measured was 10,000 times greater than the theory, which means the selection of materials for the low valence band offset DBR was a vast improvement. For the n-type control DBR the measured ρ_c was actually 10 times less than expected from theory, and also was smaller than the low

Table 5.6 Measured ρ_c data for MBE1141, the n-type control DBR.

Contact Size	25x25	25x25	10x20	10x20
Structure	Mesa	Stripe	Mesa	Stripe
ρ_c (Ω·cm^2):	7.6666E-05	6.5114E-05	4.3162E-05	3.8462E-05
	7.5517E-05	6.5484E-05	4.2799E-05	3.7862E-05
	7.6840E-05	6.7441E-05	4.3108E-05	3.7532E-05
	7.8750E-05	6.8678E-05	4.3300E-05	3.7800E-05
	6.7304E-05	7.1914E-05	4.4845E-05	4.4222E-05
	6.8136E-05	7.1272E-05	4.4688E-05	3.6530E-05
	6.6480E-05	7.3281E-05	4.5174E-05	4.6154E-05
	5.4987E-05	6.2460E-05	3.9571E-05	3.4163E-05
	5.9097E-05	6.1376E-05	3.8908E-05	4.3600E-05
	5.7995E-05	6.3449E-05	4.2278E-05	3.5889E-05
	5.8507E-05	6.2968E-05		3.5315E-05
	6.0363E-05	6.3513E-05		3.5483E-05
	6.1007E-05	7.1003E-05		
	5.3077E-05	6.5365E-05		
	5.5474E-05	5.3199E-05		
	5.6224E-05	6.1667E-05		
	5.6771E-05	6.4218E-05		
	5.5467E-05	5.4608E-05		
	5.4727E-05	5.6111E-05		
	5.4711E-05			
	6.1693E-05			
	6.4167E-05			
	6.9826E-05			
	5.9097E-05			
	5.3402E-05			
	6.9757E-05			
	6.3568E-05			
Average ρ_c:	6.2578E-05	6.4375E-05	4.2783E-05	3.8584E-05
# of data points:	27	19	10	12
Standard Deviation:	7.716E-06	5.480E-06	1.993E-06	3.740E-06

Table 5.7 Summary of theoretical and experimental specific contact resistance values for the four DBR structures.

Sample	Type	DBR Materials	Composition	ρ_c ($\Omega \cdot cm^2$)	
				Theoretical	Experimental
MBE1136	p	AlGaAs/AlGaInP	xT=0.9/xQ=0.14	2.35×10^{-4}	2.75×10^{-4}
MBE1139	p	AlGaInP/AlGaInP	xQ=0.44/0.14	3.85×10^{-4}	30
MBE1140	n	AlAs/AlGaInP	xQ=0.10	1.20×10^{-5}	2.58×10^{-5}
MBE1141	n	AlInP/AlGaInP	xQ=0.52/0.10	7.53×10^{-5}	5×10^{-6}

conduction band offset DBR. This would seem to indicate that the materials for the low band offset made no improvement in the n-type DBR performance. This problem, as well as the question of why the theory worked so well for the low offset DBRs but not for the control samples, will be discussed in the next section.

5.5.2 Discrepancies in the Control Samples

As pointed out above, the experimental specific contact resistance values for both the p-type and n-type control samples were orders of magnitude away from their theoretical values. On the other hand, the calculated values based on the theoretical model matched very well with the experimental results for the low valence and conduction band offset DBRs. Because of this, it was assumed that the error lay somewhere within the structure of the control samples themselves, rather than in the DBR resistance model based on the Schottky barrier theory. Since the DBR resistances were dominated by the barrier resistances, any possible changes to the bulk resistance, such as from an error in the bulk resistivity values, were ignored. Possible structural problems with the control samples that would affect the

resistance due to the barrier include an error in the determination of the energy band offsets used in the theory, or the incorporation of charge during the MBE growth at the heterojunction interfaces, either between the individual DBR layers or between the DBR and the GaAs substrate.

Using the measured ρ_c values and the fact that the error must be in the barrier resistances, one can work backward through the theory to determine the energy band offsets required to obtain the measured values. For the p-type control sample a larger valence band barrier is needed in order to obtain the higher ρ_c measured, while for the n-type control sample a smaller conduction band barrier is needed to obtain the lower ρ_c. The suspect heterojunction either could be at the interface between the GaAs substrate and the high index of refraction AlGaInP layer, xQ=0.14 for p-type and 0.10 for n-type, at the bottom of the DBR, or at the interfaces between the high and low index DBR layers. Since the AlGaInP/GaAs heterojunction in each control sample also existed in the corresponding low band offset samples, that junction could not be the source of the errors. Any changes in that barrier height to bring theory in line with experiment for the control samples would ruin the current agreement for the low offset DBRs. Thus the problem had to be between the high index AlGaInP DBR layers and the low index AlGaInP layers, xQ=0.44 for p-type and 0.52 (i.e. AlInP) for n-type. Assuming identical heterojunction barriers throughout the DBR structures, the barrier heights required theoretically to correspond to the measured ρ_c values were 572 meV for p-type and 50 meV for n-type, compared to 179 meV and 151 meV, respectively, as used in the original theoretical calculations. Thus the valence band offset increased by almost 400 meV for the p-type control DBR, while the conduction band offset

decreased by 100 meV for the n-type control DBR. This can be seen in Figures 5.14 and 5.15 for the p-type and n-type heterostructures, respectively. Part (a) of each figure shows the band diagrams for the control samples as originally calculated in Chapter III, and part (b) shows how the heterojunctions must change so the theoretical ρ_c values match experiment.

The possibility of an error in the band offsets used in the calculations exists, but such an error could not account for the large discrepancy required in both the n-type and p-type control DBRs. For the AlGaInP material system the energy band gap, E_g, is well established for all aluminum compositions. Thus for an AlGaInP/AlGaInP heterojunction the difference in the band gaps, ΔE_g, is also accurately known. However, the split of ΔE_g between the valence band (ΔE_v) and the conduction band (ΔE_c) offsets has been the subject of debate in the literature. So the values used in the calculations of Chapter III and Appendix C may have some uncertainty. With ΔE_g known and fixed, any error in the value of ΔE_v must be equal and opposite to that of ΔE_c. So even when taking into account the difference in ΔE_g values for the p-type $Al_{0.44}Ga_{0.08}In_{0.48}P/Al_{0.14}Ga_{0.38}In_{0.48}P$ as compared to the n-type $Al_{0.52}In_{0.48}P/Al_{0.10}Ga_{0.42}In_{0.48}P$ heterojunction, 373 meV versus 430 meV, it is impossible for ΔE_v to increase 400 meV in the p-type sample while ΔE_c decreases only 100 meV in the n-type sample. Thus any errors in the energy band offset values for the AlGaInP material system can not explain the discrepancy between the experimental and theoretical ρ_c values for the control DBR samples.

The existence of charge at the interface between the individual DBR layers is a possible cause for the difference between the theoretical control DBR structures and the as-grown samples. Remember, in an ideal isotype heterojunction (p-p or n-n) carriers move

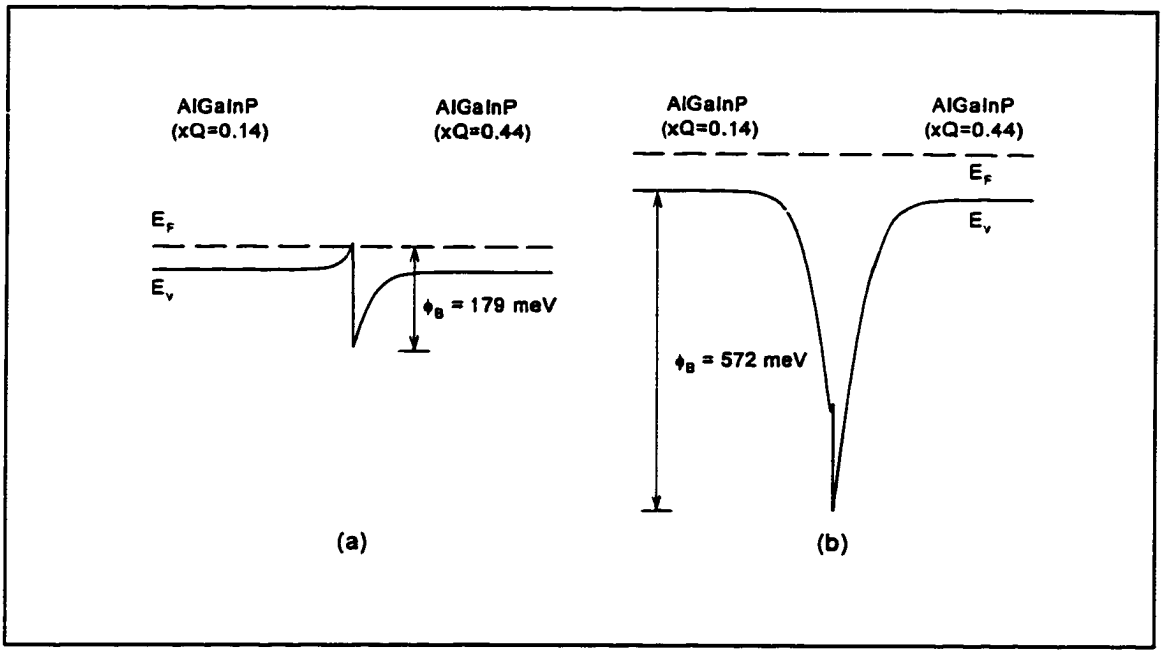

Figure 5.14 Heterojunction energy band diagrams for the p-type AlGaInP/AlGaInP (xQ=0.44/0.14) control sample (a) as designed for growth and (b) as required to make ρ_c theory match experiment. Part (b) was calculated with the inclusion of a positive charge trapped at the AlGaInP/AlGaInP interface.

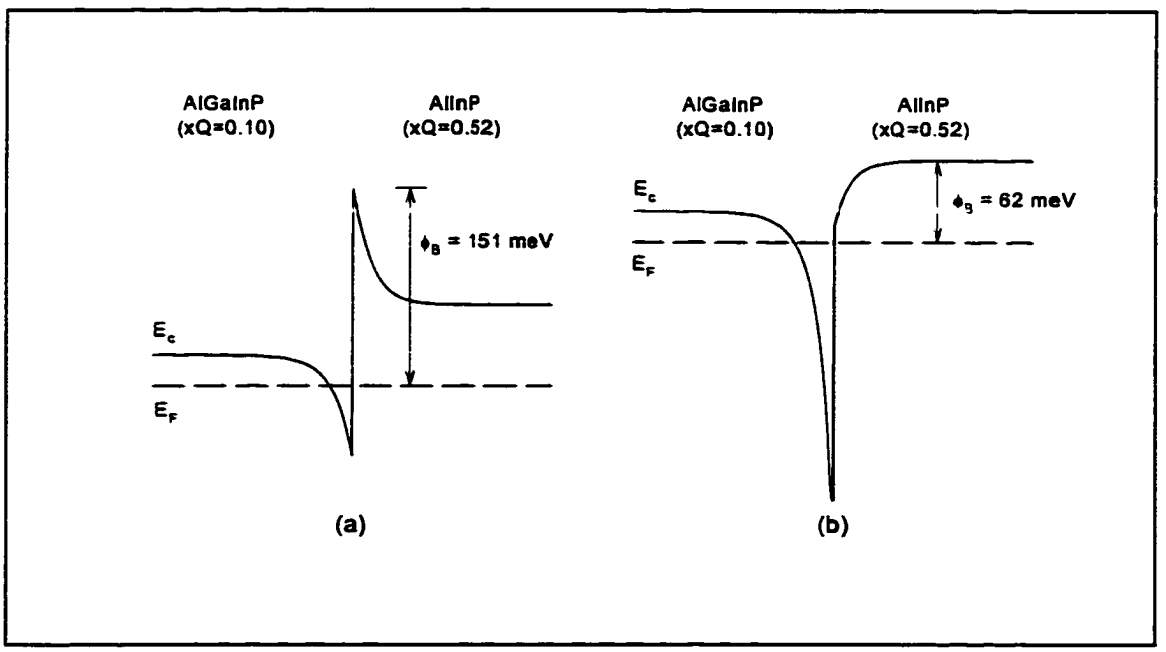

Figure 5.15 Heterojunction energy band diagrams for the n-type AlInP/AlGaInP control sample (a) as originally calculated in Chapter III, and (b) as required to make theory match experiment. Part (b) was calculated using a positive charge at the interface.

from the larger band gap material into the smaller band gap material, causing the energy bands to bend, until equilibrium is achieved. The incorporation of charge at a heterojunction interface changes the amount of carrier movement needed to reach equilibrium and thus alters the band bending and the resulting barrier. Whether the barrier energy is increased or decreased depends upon the type of doping in the semiconductor layers and the sign of the charge trapped between them. For a p-type heterojunction, a negative charge trapped at the interface means less hole depletion to achieve equilibrium and thus a smaller barrier, while a positive interface charge results in increased hole depletion and a larger energy band barrier. Similarly, for an n-type heterojunction a negative charge at the interface means more electron depletion to achieve equilibrium with a larger barrier, and a positive interface charge results in a smaller conduction band energy barrier.

So, looking at the barrier shifts required to make the theoretical ρ_c correspond with experiment, +400 meV for p-type and -100 meV for n-type, the incorporation of a positive charge at each DBR interface was needed for both control samples. A 1.0 nm n-type layer with donor concentration N_i was used to simulate the addition of a positive charge trapped at the DBR interfaces, and SimWindows was used to calculate the equilibrium band structure. By adjusting the value of N_i the barrier height at the interface could be controlled. For the p-type control DBR, an interface concentration of $N_i=7.0\times10^{19}$ cm^{-3} resulted in a valence band barrier height of 572 meV, which was the value required for the theoretical ρ_c calculation to match the experimental value of 30 $\Omega\cdot$cm^2. For the n-type control DBR, the inclusion of an N_i greater than 4.0×10^{19} cm^{-3} resulted in the flattening of the conduction band in the large band gap AlInP layer so that the barrier was no longer a triangular one but rather

was a step barrier of 62 meV. Using this barrier height the theoretical ρ_c calculated was 6.5×10^{-6} $\Omega\cdot cm^2$, which was within the range of the experimental value. Thus the incorporation of $N_i \approx 7\times10^{19}$ cm^{-3}, or 7×10^{12} positive charges/cm^2, at the interface between each DBR layer brought the theoretical specific contact resistance calculations into agreement with the measured values for both the p-type and n-type control DBR samples. The band diagrams in part (b) of Figures 5.14 and 5.15 were obtained from SimWindows calculations by including the 7×10^{19} cm^{-3} positive charge concentration at the DBR heterojunction interface.

In summary, as seen in Table 5.7, the low band offset DBRs performed as expected from the theoretical specific contact resistance calculations. However, neither of the control samples performed as expected; the p-type one was much more resistive while the n-type sample was much less resistive. In order to have theory match experiment, a large positive interface charge was incorporated between each DBR layer for these control samples. Comparing the results of the low valence band offset $Al_{0.9}Ga_{0.1}As/Al_{0.14}Ga_{0.38}In_{0.48}P$ DBR with its p-type $Al_{0.44}Ga_{0.08}In_{0.48}P/Al_{0.14}Ga_{0.38}In_{0.48}P$ control sample, it was obvious that the use of the low band offset had its desired effect. The lower barrier resulted in a smaller impediment to carrier flow and thus significantly decreased the resistance of the stack. For the n-type case, the benefits of using the low conduction band offset $AlAs/Al_{0.10}Ga_{0.42}In_{0.48}P$ design were not as evident. The $Al_{0.52}In_{0.48}P/Al_{0.10}Ga_{0.42}In_{0.48}P$ control sample actually had a smaller resistance. However, as the above analysis showed, this was due to the incorporation of the positive interface charge. When using the control DBR in a vertical cavity surface emitting laser (VCSEL) the existence of the interface charge would cause

more problems than the lower ρ_c would solve. The presence of the charge could increase the optical absorption in the VCSEL, increasing the gain required to meet threshold and increasing the power consumed in the device, thus degrading performance. In addition, the underlying cause of the charge at the interface is not understood, so it may not be controllable or reproducible and thus not a practical method for lowering the DBR resistance. Overall, the low band offset AlGaAs/AlGaInP design resulted in better DBR structures for use in VCSELs than the all phosphide AlGaInP control DBRs.

REFERENCES: CHAPTER V

[1] D. Lee, "Carrier Concentrations in AlGaAs," in Properties of Aluminum Gallium Arsenide, Edited by S. Adachi; INSPEC: London, 1993.

[2] R. Malik, J. Nagle, M. Micovic, T. Harris, R. Ryan, and L. Hopkins, "Doping limits of C, Be, and Si in GaAs grown by solid source molecular beam epitaxy with a thermally cracked As_2 source," *J. Vac. Sci. Technol.* **B10**, 850 (1992).

[3] M. Ilegems, "Beryllium doping and diffusion in molecular beam epitaxy of GaAs and $Al_xGa_{1-x}As$," *J. Appl. Phys.* **48**, 1278 (1977).

[4] R. Kopf, E. Schubert, S. Downey, and A. Emerson, "N- and p-type dopant profiles in distributed Bragg reflector structures and their effect on resistance," *Appl. Phys. Lett.* **61**, 1820 (1992).

[5] S. Fujita, S. Bedair, M. Littlejohn, and J. Hauser, "Doping characteristics and electrical properties of Be-doped p-type $Al_xGa_{1-x}As$ by liquid phase epitaxy," *J. Appl. Phys.* **51**, 5438 (1980).

[6] T. Drummond, W. Lyons, R. Fischer, R. Thorne, and H. Morkoc, "Si incorporation in $Al_xGa_{1-x}As$ grown by molecular beam epitaxy," *J. Vac. Sci. Technol.* **21**, 957 (1982).

[7] D. Miller and P. Asbeck, "Be redistribution during growth of GaAs and AlGaAs by molecular beam epitaxy," *J. Appl. Phys.* **57**, 1816 (1985).

[8] N. Chand, R. Fischer, J. Klem, T. Henderson, P. Pearah, W. Masselink, Y. Chang, and H. Morkoc, "Beryllium and silicon doping studies in $Al_xGa_{1-x}As$ and new results on persistent photoconductivity," *J. Vac. Sci. Technol.* **B3**, 644 (1985).

[9] R. Pierret, Advanced Semiconductor Fundamentals (Modular Series on Solid State Devices, Volume VI); Addison-Wesley: Reading, MA, 1987.

[10] H. Tanaka, Y. Kawamura, and H. Asahi, "Refractive indices of $In_{0.49}Ga_{0.51-x}Al_xP$ lattice matched to GaAs," *J. Appl. Phys.* **59**, 985 (1986).

[11] S. Wemple and M. DiDomenico, Jr., "Behavior of the electronic dielectric constant in covalent and ionic materials," *Phys. Rev. B* **3**, 1338 (1971).

[12] S. Adachi, "GaAs, AlAs, and $Al_xGa_{1-x}As$: Material parameters for use in research and device applications," *J. Appl. Phys.* **58**, R1 (1985).

[13] TFCalc, Version 3.2; copyright: Software Spectra, Inc., Portland, OR, 1996.

[14] W. Bartels, "Characterization of thin layers on perfect crystals with a multipurpose high resolution x-ray diffractometer," *J. Vac. Sci. Technol.* **B1**, 338 (1983).

CHAPTER VI

CONCLUSIONS

The objective of this research project was to lower the series resistance of distributed Bragg reflectors (DBRs) for use in visible wavelength vertical cavity surface emitting lasers (VCSELs) through the selection of semiconductor materials with small energy band offsets. The low band offsets provided smaller barriers to carrier flow than seen in typical DBR structures, thus lowering the resistance of the stack without resorting to complicated designs and growths. This chapter presents a summary of this work, from the initial theoretical calculations through the materials characterization and experimental results.

A wide variety of III-V semiconductors were investigated to determine their suitability for providing the low band offset heterojunctions sought for the DBR structures. In DBRs it is desirable for the difference in refractive index, Δn, between the two constituent material layers to be as large as possible in order to minimize the number of periods required to obtain the reflectance necessary for VCSELs. However, in a given semiconductor material system such as AlGaAs, Δn is directly proportional to the change in energy band gap, ΔE_g, so that using AlAs/GaAs layers in a DBR to get a large Δn also results in large barriers to current flow across the heterojunction interfaces of the DBR. Energy band offset calculations, using an approach to the Van de Walle model solid theory [1] as demonstrated

by Krijn [2], showed that low valence and conduction band offsets could be attained, while still maintaining sufficiently large Δn values, through the use of AlGaAs/AlGaInP heterojunctions.

In this mixed arsenide and phosphide system, aluminum compositions of $xT=0.9$ for the AlGaAs and $xQ=0.14$ for the AlGaInP were selected to give a low valence band offset, $\Delta E_v=100$ meV, p-type DBR. A 40.5 period structure gave greater than 99% reflectance near the target wavelength of 650 nm. The same optical properties were achieved in a 40.5 period n-type DBR using $xT=1.0$ and $xQ=0.10$, which had a 20 meV conduction band offset. To provide a comparison with the low band offset AlGaAs/AlGaInP DBRs, heterojunctions with large band offsets were also selected for study. The larger band offsets should result in DBRs with larger resistance values. For continuity, the AlGaInP layer of the low band offset structures was kept the same, and different composition AlGaInP alloys, $xQ=0.44$ for p-type and 0.52 for n-type, were substituted for the AlGaAs layers. Valence and conduction band offsets for the two control samples were 179 meV and 151 meV, respectively, and each DBR structure met the targeted optical characteristics with the same 40.5 periods.

The specific contact resistance, ρ_c in units of $\Omega \cdot cm^2$, of the DBR stack was calculated for each of the four structures under investigation. The total stack resistance was modeled as a series of bulk layer resistances plus a series of barrier resistances in order to account for the properties of the individual materials plus the effects of their interfaces. The bulk layer resistances were calculated using the resistivities and thicknesses of the individual material layers, while barrier resistances were determined through an application of the Schottky metal-semiconductor contact theory. Numerical results showed that the use of the low band

offset DBR structures decreased ρ_c by a factor of only about two for the p-type case and a factor of six for the n-type case when compared to the control sample structures.

The material quality of the AlGaAs and AlGaInP alloys used for the DBRs was studied through a series of bulk layer gas source molecular beam epitaxy (MBE) growths. Growth conditions were established for obtaining good crystal quality AlAs films, as determined by double crystal x-ray diffraction (DCXD) measurements. Carrier concentration levels of 2×10^{18} cm^{-3} were desired for the DBR structures, and this level was obtained, as determined by Hall-van der Pauw measurements, for n-type AlAs using silicon dopants and a lower substrate growth temperature than typically used for GaAs. However, doping AlAs p-type with beryllium proved to be more difficult. Even with a high dopant flux and a low substrate temperature, 3×10^{17} cm^{-3} was the maximum hole concentration achieved. As it turned out, this was very close to the maximum value found in the literature, 5×10^{17} cm^{-3} [3]. In order to obtain hole concentrations of 2×10^{18} cm^{-3}, a small amount of gallium was added to the alloy. Thus, for the low valence band offset DBR, xT=0.9 was used instead of pure AlAs. A more detailed investigation, beyond the limited number of samples grown for this project, into the cause of the carrier concentration saturation for the high aluminum content AlGaAs alloys would make a useful future study.

Similar results were seen during the characterization of the bulk AlGaInP alloys. DCXD experiments revealed high quality crystal structures for all aluminum compositions, from GaInP to AlInP. High carrier concentrations were obtained for the low aluminum content AlGaInP, xQ=0.14 for p-type or 0.10 for n-type, used in the quaternary layers common to both the low band offset and control DBR samples. For the high aluminum

content AlGaInP layers used in the control samples, 2×10^{18} cm^{-3} electrons were measured in the n-AlInP, but in the p-AlInP a hole concentration of only 2×10^{17} cm^{-3} was attained. Following the p-AlAs example and adding some gallium increased the concentration of holes, but it also decreased the valence band barrier, potentially decreasing the DBR resistance, which was the purpose of the control sample. A compromise was reached with the use of p-AlGaInP with xQ=0.44, where the hole concentration was boosted somewhat, to about 5×10^{17} cm^{-3}, while still maintaining a large enough valence band offset to provide a meaningful control sample. Theoretical resistance calculations showed that this material substitution had a negligible effect on the resistance of the p-type control DBR.

With the individual layer materials qualified, the four DBR structures were grown by MBE and their structural quality was characterized by DCXD and reflectance measurements. The x-ray spectra showed multiple satellite peaks, as expected from a superlattice design, for all four samples, indicating the DBRs were of high quality crystal structure. The measured peak reflectance was 99% for each sample, as needed in a VCSEL, and their locations were all within 4% of the 650 nm target center wavelength. Also, the shape of the measured reflectance spectrum was consistently asymmetric when compared with simulation.

Pieces of all four DBR samples were processed and their specific contact resistances determined using the transmission line model. The measured values of the low band offset DBRs, 2.75×10^{-4} $\Omega\cdot cm^2$ for p-type and 2.58×10^{-5} $\Omega\cdot cm^2$ for n-type, were within experimental uncertainty of their theoretical values. For the control samples the experimental ρ_c was four orders of magnitude larger than the theory in the p-type case, while for the n-type case the

measured ρ_c was an order of magnitude smaller. This discrepancy was explained in both control samples by the incorporation of a large positive charge at the interfaces between the individual layers of the DBR structures. The interface charge caused the valence band barrier to increase in the p-type DBR, thus increasing the measured ρ_c, while in the n-type control sample the positive charge caused the conduction band barrier to decrease, resulting in a measured ρ_c value that was smaller than the original theoretical value.

Thus the low energy band offset DBRs were an improvement over the all phosphide control mirrors. In the p-type case, the low valence band structure provided a much smaller resistance. On the other hand, the low conduction band n-type structure did not have a smaller ρ_c than its control sample. However, as discussed in Chapter V, the interface charge of the control sample could be a greater detriment to a VCSEL than its lower resistance would be a benefit to the laser. So the low conduction band offset DBR was still a more desirable structure.

The measured specific contact resistance results for the low band offset DBRs compared very favorably with numbers reported in the literature for AlGaAs DBRs. Dividing by the number of periods for comparison purposes, *the ρ_c values for this work were 6.9×10^{-6} $\Omega\cdot cm^2$/period for p-type and 6.4×10^{-7} $\Omega\cdot cm^2$/period for n-type*. For an abrupt DBR design as used in this project, with no grading of the composition or modulation of the doping near the interfaces, 2×10^{-4} $\Omega\cdot cm^2$/period has been reported for a p-type AlAs/GaAs DBR nominally doped 3×10^{18} cm^{-3} [4]. Using various alloy composition grading and modulation doping schemes, ρ_c values for p-type AlAs/GaAs DBRs drop to anywhere in the range of $1\text{-}10\times10^{-6}$ $\Omega\cdot cm^2$/period [4-7], depending upon the scheme and the nominal doping

levels. So the simple, abrupt interface, low valence band offset p-type DBR of this project performed better than an abrupt interface AlAs/GaAs DBR, and comparable to DBRs using structural schemes that were more complicated as well as more difficult to grow.

Because the resistance of the p-type DBRs is considered the dominant resistance in a VCSEL, there was minimal ρ_c data available in the literature for n-type DBRs. One report, for a linearly graded, modulation doped AlAs/GaAs structure gave $5\times10^{-6}\,\Omega\cdot cm^2$/period [7], which is an order of magnitude larger than achieved with the low conduction band offset AlAs/AlGaInP DBR. The only report on all phosphide DBRs gave $1.5\times10^{-4}\,\Omega\cdot cm^2$/period for an abrupt interface, n-type AlInP/AlGaInP (xQ=0.2) structure [8]. This was even larger than the original theoretical calculation for the n-type control DBR, $2\times10^{-6}\,\Omega\cdot cm^2$/period, which had a similar structure but with xQ=0.10 giving it a smaller conduction band offset. *So the low conduction band offset DBR design resulted in a much lower ρ_c per period than those few reported in the literature.*

Finally, the most obvious future extension of the work in this dissertation would be the growth of visible wavelength VCSELs using the low band offset DBRs. The resulting laser characteristics could then be compared with those using the more common AlGaAs DBRs [9]. Incorporating some of the resistance minimization schemes used in the AlGaAs DBRs into the AlGaAs/AlGaInP design, to see what, if any, improvements they would make, would be very interesting. Part of the reason for using the low band offset material was to avoid the complicated growths associated with those schemes, and their use may not be worth it in the n-type case. However, for the p-type DBR a simple interface grading scheme such as a single barrier reduction interface layer, as opposed to some of the elaborate and

more complicated schemes used in AlGaAs DBRs, would help minimize the small valence band offset. With this addition, ρ_c for the AlGaAs/AlGaInP p-type DBR could possibly drop an order of magnitude below that measured for the p-type all-AlGaAs DBRs. An important thing to recall from the theoretical calculations in Chapter III is that the AlGaInP/GaAs (DBR/substrate) interface in the low valence band offset DBR contributed 80% of the total calculated resistance. In a visible VCSEL structure there would be no GaAs next to the p-DBR, and this fact alone would improve its resistance. At the very least, the introduction of a simple doping modulation, with greater than 10^{18} cm^{-3} used only near the interfaces, could be implemented without hurting the already small ρ_c values of the low offset DBRs, and it would improve the characteristic properties of VCSELs using that DBR structure.

REFERENCES: CHAPTER VI

[1] C. Van de Walle, "Band lineups and deformation potentials in the model-solid theory," *Phys. Rev. B* **39**, 1871 (1989).

[2] M. Krijn, "Heterojunction band offsets and effective masses in III-V quaternary alloys," *Semicond. Sci. Technol.* **6**, 27 (1991).

[3] R. Kopf, E. Schubert, S. Downey, and A. Emerson, "N- and p-type dopant profiles in distributed Bragg reflector structures and their effect on resistance," *Appl. Phys. Lett.* **61**, 1820 (1992).

[4] R. S. Geels, S. W. Corzine, J. W. Scott, D. B. Young, and L. A. Coldren, "Low threshold planarized vertical cavity surface emitting lasers," *IEEE Photonics Tech. Lett.* **2**, 234 (1990).

[5] S. Chalmers, K. Lear, and K. Killeen, "Low resistance wavelength-reproducible p-type (Al,Ga)As distributed Bragg reflectors grown by molecular beam epitaxy," *Appl. Phys. Lett.* **62**, 1585 (1993).

[6] M. Hong, J. P. Mannaerts, J. M. Hong, R. J. Fischer, K. Tai, J. Kwo, J. M. Vandenberg, Y. H. Wang, and J. Gamelin, "A simple way to reduce series resistance in p-doped semiconductor distributed Bragg reflectors," *J. Crystal Growth* **111**, 1071 (1991).

[7] M. Peters, B. Thibeault, D. Young, A. Gossard, and L. Coldren, "Growth of beryllium doped $Al_xGa_{1-x}As$/GaAs mirrors for vertical cavity surface emitting lasers," *J. Vac. Sci. Tech.* **B12**, 3075 (1994).

[8] H. Sugawara, K. Itaya, and G. Hatakoshi, "Characteristics of a distributed Bragg reflector for the visible-light spectral region using InGaAlP and GaAs: comparison of transparent- and loss-type structures," *J. Appl. Phys.* **74**, 3189 (1993).

[9] W. Chow, K. Choquette, M. Crawford, K. Lear, and G. Hadley, "Design, fabrication, and performance of infrared and visible vertical cavity surface emitting lasers," *IEEE J. Quantum Elec.* **33**, 1810 (1997).

APPENDIX A

TLM FABRICATION PROCESS STEPS

This appendix provides a detailed outline of the DBR Transmission Line Model (TLM) test structure fabrication process. All process steps were carried out in the Electrical Engineering Department's Semiconductor Processing Cleanroom at CSU, unless otherwise indicated. Equipment specifications, when applicable, were given in Chapter IV. This appendix is sectioned into procedures surrounding each of the three mask steps previously described in Chapter IV.

A.1 Mask #1: Mesa Etch

1) Clean sample
   - solvent rinse (trichloroethylene, acetone, methanol)
   - 20 second buffered hydrofluoric (HF) acid etch
   - deionized water (DI H_2O) rinse an nitrogen gas (N_2) blow dry
2) SiO_2 CVD (0.5 μm to 1.0 μm)
   - 20 to 30 minutes at 320°C substrate temperature and slow substrate rotation
   - Silane flow set at 38 sccm; O_2 flow set at 4 sccm
3) Photolithography
   - mount sample on cover slip using crystal bond
   - rinse sample with acetone, methanol, and DI H_2O
   - pre-bake at 120°C for 2 minutes
   - coat with Shipley C-20 primer; let stand 5 seconds; spin at 5000 rpm for 30 seconds
   - spin on Shipley 1818 photoresist at 6000 rpm for 30 seconds
   - soft bake at 95°C for 2 minutes
   - expose to Mesa Etch mask for 8 seconds
   - develop in AZ 400K developer (always mixed 1:4 with DI H_2O) for 40 seconds
   - post-bake at 120°C for 2 minutes

- etch SiO_2 mesas using buffered HF for 1 to 2 minutes (depending on SiO_2 thickness)
- remove remaining photoresist using acetone
- remove sample from cover slip and rinse with acetone, methanol, and DI H_2O

4) DBR mesa etch (performed at the Engineering Research Center, CSU)
- Chemical Assisted Ion Beam Etching using chlorine gas
- etch times vary depending upon sample and chamber conditions

A.2 Mask #2: Contact Vias

1) SiO_2 CVD (1500 - 2000 Å)
- rinse with acetone, methanol, and DI H_2O
- 3 to 5 minutes at 320°C substrate temperature and slow substrate rotation
- Silane flow set at 38 sccm; O_2 flow set at 4 sccm

2) Polyimide VM651 adhesion promoter preparation
- remove from freezer (allow it to warm to room temperature before opening)
- mix solution of methanol, DIH_2O, and VM651 (95:5:0.1-1.0 ml)
- must stand a minimum of 12 hours before use (20 day shelf life)

3) Polyimide photolithography process
- remove PI-2555 polyimide from freezer and allow it to warm to room temp.
- mount sample on cover slip with crystal bond
- rinse with acetone, methanol, and DI H_2O
- pre-bake 2 minutes at 120°C
- spin on VM651 at 5000 rpm for 30 seconds
- coat sample with PI-2555; let stand for 30 seconds
- spin polyimide for 30 seconds at 7000 rpm
- soft cure 10 minutes at 120°C
- let cool and air dry for 30 minutes at room temperature
- spin on Shipley 1818 photoresist at 6000 rpm for 30 seconds
- soft bake 2 minutes at 95°C
- align Mask #2 features with the mesas on the sample
- expose to Contact Via mask for 8 seconds
- develop in AZ 400K developer for approximately 40 seconds (the polyimide etches in the developer at the same time)
- rinse quickly with acetone, methanol, and DI H_2O
- remove from cover slip
- hard cure in polyimide oven with N_2 overflow using the following cure cycle:
  1 hour ramp from room temperature to 200°C
  4 hour cure at 200°C
  1 hour ramp back to room temperature

4) SiO_2 via etch photolithography
- mount sample on cover slip with crystal bond
- rinse with acetone, methanol, and DI H_2O

- pre-bake at 120°C for 2 minutes
- spin on Shipley 1818 photoresist at 6000 rpm for 30 seconds
- soft bake at 95°C for 2 minutes
- align Mask #2 features within the polyimide openings on the mesas of the sample
- expose to Contact Via mask for 8 seconds
- develop in AZ 400K developer for 40 seconds
- post-bake at 120°C for 2 minutes
- etch SiO_2 vias down to bare semiconductor on the mesa tops using buffered HF

A.3 Mask #3: Metallization

1) Lift-off photolithography
   - mount sample on cover slip
   - rinse with acetone, methanol, and DI H_2O
   - pre-bake 2 minutes at 120°C
   - spin on Shipley 1818 photoresist at 4500 rpm for 30 seconds
   - soft bake 2 minutes at 95°C
   - soak in chlorobenzene for 4 minutes
   - blow dry with N_2 gas (do not rinse with DI H_2O)
   - align Mask #3 features with those on the sample
   - expose to Metallization mask for 0.9 minute
   - develop in AZ 400K developer for approximately 1.0 minute
2) Metal evaporation and lift-off
   - follow standard cleanroom electron beam evaporator procedures
   - n-type contacts: Ge/Au/Ni/Au (250/520/150/1000 Å)
   - p-type contacts: Ti/Au (600/2500 Å)
   - soak in acetone to remove photoresist and lift-off metal
   - remove from cover slip
   - rinse in acetone, methanol, and DI H_2O
3) Anneal metal
   - place sample in Bio-Rad annealing furnace
   - cover with glass jar and purge with nitrogen
   - anneal for approximately 3 minutes
   - sample temperature around 400°C; varies depending upon metal

APPENDIX B

AlAs/AlGaInP BAND OFFSET CALCULATION

This is a sample program file for the Mathcad software package. It demonstrates the heterojunction band offset calculations described in Chapter III. This example uses AlAs as the low refractive index layer, and varies the aluminum concentration in the AlGaInP alloy for the high index layer. The matrices are all taken from data in Krijn's paper [*Semicond. Sci. Tech.* **6**, 27 (1991)]. Other AlGaAs material data is taken from Adachi [*J. Appl. Phys.* **58**, R1 (1985)].

$Al_xGa_yIn_{1-x-y}As$ Quaternary

Note: Krijn only has matrix elements for gamma bands. Assume AlGaAs is a direct band gap (Γ) for xT<0.45, and is an indirect band gap (X) for xT>0.45.

AlGaAs =====> xT = Al concentration; 1-xT-y = 0; and $y(xT) := 1 - xT$

$$CevavT := \begin{bmatrix} -6.67 & -0.201 & -0.049 \\ -0.496 & -0.378 & 0 \\ -0.324 & 0 & 0 \end{bmatrix} \qquad EvavT(xT) := \left[\sum_{i=0}^{2} \left[\sum_{j=0}^{2} CevavT_{i,j} \cdot xT^i \cdot (1 - xT)^j \right] \right]$$

$$C\Delta oT := \begin{bmatrix} 0.38 & -0.19 & 0.15 \\ -0.25 & 0.3 & 0 \\ 0.15 & 0 & 0 \end{bmatrix} \qquad \Delta oT(xT) := \left[\sum_{i=0}^{2} \left[\sum_{j=0}^{2} C\Delta oT_{i,j} \cdot xT^i \cdot (1 - xT)^j \right] \right]$$

$$CEg\Gamma T := \begin{bmatrix} 0.36 & 0.68 & 0.38 \\ 1.89 & 0.71 & 0 \\ 0.7 & 0 & 0 \end{bmatrix} \qquad Eg\Gamma T(xT) := \left[\sum_{i=0}^{2} \left[\sum_{j=0}^{2} CEg\Gamma T_{i,j} \cdot xT^i \cdot (1 - xT)^j \right] \right]$$

$$EvT(xT) := EvavT(xT) + \frac{\Delta oT(xT)}{3} \qquad EgXT(xT) := 1.90 + 0.125 \cdot xT + 0.143 \cdot xT^2 \quad (x>0.45)$$

For AlAs: xT := 1.0 ===> ΔoT(xT) = 0.28 eV EvT(xT) = -7.397 eV

EgXT(xT) = 2.168 eV EvavT(xT) = -7.49 eV

$Al_xGa_yIn_{1-x-y}P$ Quaternary

Lattice Constants: aAlP 5.4510 Å aInP 5.86875 Å

aGaP 5.4505 Å aGaAs 5.65315 Å

$aQ(x,y) := x \cdot aAlP + y \cdot aGaP + (1 - x - y) \cdot aInP$

Lattice Matched to GaAs: $xlmalinp := \frac{aGaAs - aInP}{aAlP - aInP}$ $ylmgainp := \frac{aGaAs - aInP}{aGaP - aInP}$

xlmalinp = 0.5161 ylmgainp = 0.51548

===> for AlInP: x = 0.516 y = 0

===> for GaInP: x = 0 y = 0.515

$xQ := 0, 0.012 .. 0.516$

$ylm(x) := \frac{aGaAs - x \cdot aAlP - (1 - x) \cdot aInP}{aGaP - aInP}$

$aQlm(x) := x \cdot aAlP + ylm(x) \cdot aGaP + (1 - x - ylm(x)) \cdot aInP$

check: aQlm(xlmalinp) = 5.65315 Å aQlm(0) = 5.65315 Å

ylm(xlmalinp) = 0 ylm(0) = 0.51548

Energy Levels:

$$Cevav := \begin{pmatrix} 7.04 & 0.24 & 0.12 \\ 0.597 & 0.573 & 0 \\ .453 & 0 & 0 \end{pmatrix} \qquad EvavQ(x) := \sum_{i=0}^{2} \sum_{j=0}^{2} Cevav_{i,j} \cdot x^i \cdot ylm(x)^j$$

$$C\Delta o := \begin{pmatrix} 0.11 & 0.03 & 0 \\ 0.04 & 0 & 0 \\ 0 & 0 & 0 \end{pmatrix} \qquad \Delta oQ(x) := \sum_{i=0}^{2} \sum_{j=0}^{2} C\Delta o_{i,j} \cdot x^i \cdot ylm(x)^j$$

$$CEg\Gamma := \begin{pmatrix} 1.31 & 0.73 & 0.70 \\ 1.974 & 0.79 & 0 \\ 0.6 & 0 & 0 \end{pmatrix} \qquad Eg\Gamma Q(x) := \sum_{i=0}^{2} \sum_{j=0}^{2} CEg\Gamma_{i,j} \cdot x^i \cdot ylm(x)^j$$

(Numbers for this matrix modified from Krijn's)

$EvQ(x) := EvavQ(x) + \frac{\Delta oQ(x)}{3}$

Check: EvavQ(xlmalinp) = -7.469 eV $Eg\Gamma Q(xlmalinp) = 2.489$ eV

$\Delta oQ(xlmalinp) = 0.089$ eV EvQ(xlmalinp) = 7.439 eV

AlAs/AlGaInP Band Offsets

Varying xQ for a constant xT=1.0

$xT := 1$

Band offset equations:

$test := 0.1$

$\Delta Eg(x) := EgXT(xT) - EgΓQ(x)$ $\quad \Delta Eg(test) = 0.197$ eV

$\Delta Ev(x) := EvQ(x) - EvT(xT)$ $\quad \Delta Ev(test) = 0.179$ eV

$\Delta Ec(x) := \Delta Eg(x) - \Delta Ev(x)$ $\quad \Delta Ec(test) = 0.018$ eV

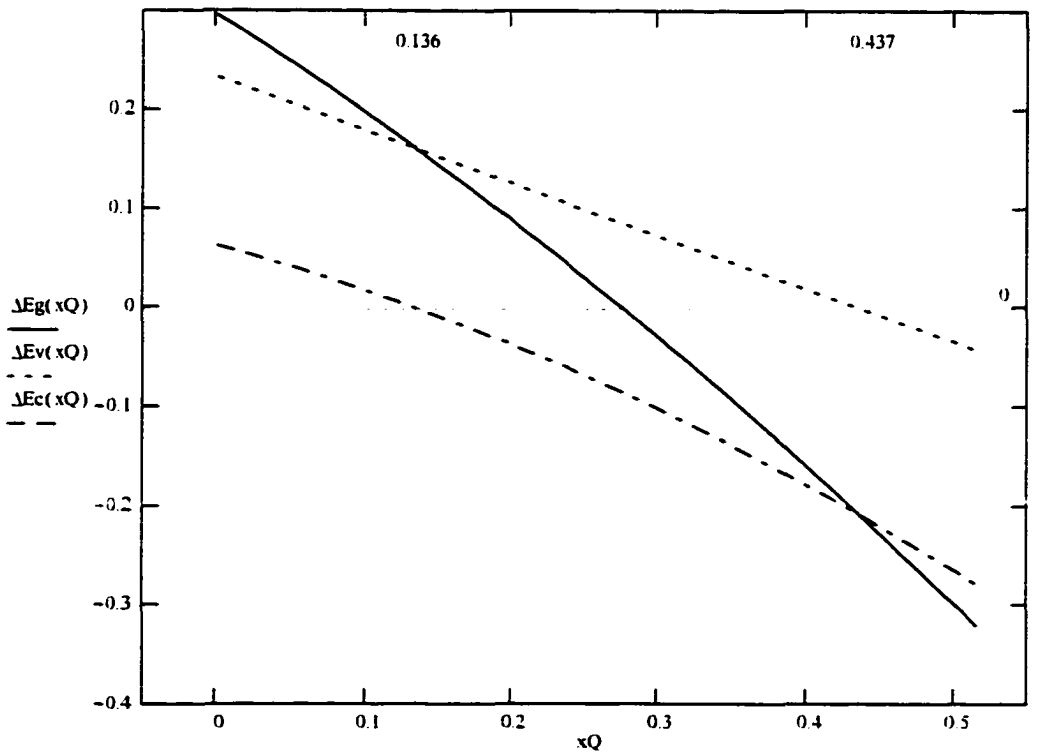

GaInP AlInP

$AlAs/Al_{xQ}Ga_{y(xQ)}In_{1-xQ-y(xQ)}P$ Band Offsets

Analysis

Conduction Band	Valence Band
Let: xoc := 0.1	Let: xov := 0.45
xΔEc0 := root ΔEc(xoc), xoc	xΔEv0 := root ΔEv(xov), xov
xΔEc0 = 0.136	xΔEv0 = 0.437
ΔEv xΔEc0 = 0.16 eV	ΔEc xΔEv0 = -0.208 eV
EgΓQ xΔEc0 = 2.009 eV	EgΓQ xΔEv0 = 2.376 eV
xΔEc100 := root ΔEc(xoc) + 0.1, xoc	xΔEv100 := root ΔEv(xov) − 0.1, xov
xΔEc100 = 0.296	xΔEv100 = 0.249

Summary: |ΔEc| < 100 meV for all xQ < 0.296

|ΔEv| < 100 meV for all xQ > 0.249

Critical Band Gap Offset Point (ΔEg=0)

Let: xog := 0.25

xΔEg0 := root ΔEg(xog), xog

xΔEg0 = 0.276

ΔEv xΔEg0 = 0.086 eV

ΔEc xΔEg0 = -0.086 eV

EgΓQ xΔEg0 = 2.168 eV

Visualization of the Heterojunction Band Lineups

$xp := -1, -0.99 .. 1$

$cbl(xp) := 1 - \Phi(xp) \cdot 0.05$ $cbg(xp) := 1 + \Phi(xp) \cdot 0.1$ $cbv(xp) := 1 + \Phi(xp) \cdot 0.25$

$vbl(xp) := -1 + \Phi(xp) \cdot 0.25$ $vbg(xp) := -1 + \Phi(xp) \cdot 0.1$ $vbv(xp) := -1 + \Phi(xp) \cdot 0$

$cbc(xp) := 1$ $cb3(xp) := 1 + \Phi(xp) \cdot 0.2$ $cb4(xp) := 1 + \Phi(xp) \cdot 0.3$

$vbc(xp) := -1 + \Phi(xp) \cdot 0.2$ $vb3(xp) := -1 + \Phi(xp) \cdot 0.05$ $vb4(xp) := -1 - \Phi(xp) \cdot 0.05$

$cb2(xp) := 1 + \Phi(xp) \cdot 0.05$

$vb2(xp) := -1 + \Phi(xp) \cdot 0.15$

Band Diagram Sketches: (note: all sketches have AlAs on the left and AlGaInP on the right)

xQ < 0.136	0.136 < xQ < 0.276	0.276 < xQ < 0.437	xQ > 0.437
Type I	Type II	Type II	Type I
Eg(AlAs) > Eg(Q)	Eg(AlAs) > Eg(Q)	Eg(AlAs) < Eg(Q)	Eg(AlAs) < Eg(Q)
	Ev(AlAs) < Eg(Q)	Ev(AlAs) < Eg(Q)	Ev(AlAs) > Eg(Q)

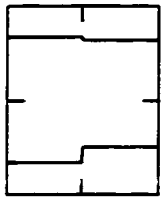
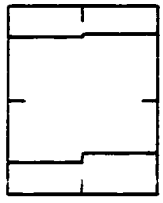
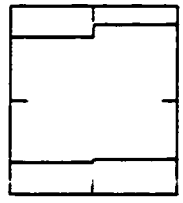
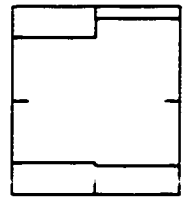

Critical Points:

xQ = 0.136	xQ = 0.276	xQ = 0.437
	Type II	
ΔEc = 0	ΔEg = 0	ΔEv = 0

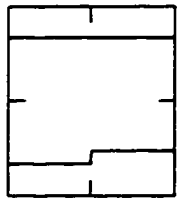
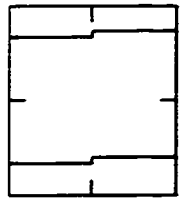
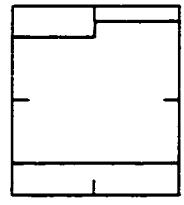

APPENDIX C

DBR RESISTANCE CALCULATIONS

This appendix presents the program file used in the Mathcad software package to calculate the theoretical series resistance of the distributed Bragg reflector (DBR) stacks studied in this project. The first section calculates the specific contact resistance due to the current flowing through the bulk DBR layers themselves. The remaining sections use the Schottky metal-semiconductor contact theory to determine the resistance contribution from the heterojunction barriers at each layer interface. An overview of the theory and a summary of the results are given in Chapter III.

C.1 Bulk Layer Resistance Calculations

Resistivity: $\rho = 1/\sigma = 1/(qN\mu)$ $\{ (C^*cm^{-3}*cm^2/V^*s)^{-1} = \Omega^*cm \}$

Assume: Nd = Na = $2x10^{18}$ cm^{-3} =====> $N := 2 \cdot 10^{18}$ cm^{-3}

$\rho(\mu) := \frac{1}{q \cdot N \cdot \mu}$ Ω^*cm $q := 1.6022 \cdot 10^{-19}$ C

Specific Contact Resistance: $R_c = \rho * t$ (Ω^*cm^2)

$Rc(t, \mu) := \rho(\mu) \cdot t \cdot 10^{-7}$ Ω^*cm^2 (t in nm)

Geometry:

When making contact to the top and bottom of the DBR stack, the resistance of the structure is dependent upon the total thickness (t), which is the sum of the quarter wavelength layer thicknesses, and the area (LxW) of the mesa, which is dependent upon the photolithography processing. In order to meaningfully compare physical measurements of various structures, the measured resistance is usually multiplied by the mesa area to get the specific contact resistance (R_c) in units of Ω^*cm^2.

For the calculations below, the specific contact resistance will be determined directly. Making theoretical to measurement comparisons will require knowledge of the actual mesa area. Also, note that the series resistance of the DBR (R/A in Ω) decreases linearly as both N and A increase, and it increases linearly with the number of mirror periods and the center mirror wavelength.

Target DBR wavelength: $\lambda o := 650\ nm$ ==> $Eo(\lambda) := \frac{1240}{\lambda}\ eV$ $Eo(\lambda o) = 1.908\ eV$

Number of DBR periods: $m := 40$

Semiconductor Material Properties:

AlGaInP (Assume a linear variation between endpoint binaries)

Mobilities: [Note: mobility data taken from text by Wolfe, Holonyak, and Stillman (1989)]

$\mu nAlP := 80$	cm^2/V^*s		$\mu pAlP := 0$	cm^2/V^*s
$\mu nGaP := 300$	cm^2/V^*s		$\mu pGaP := 150$	cm^2/V^*s
$\mu nInP := 4000$	cm^2/V^*s		$\mu pInP := 600$	cm^2/V^*s

Lattice Constants:

$aAlP := 5.4510$	A		$aInP := 5.86875$	A
$aGaP := 5.4505$	A		$aGaAs := 5.65315$	A

$aQ(x,y) := x \cdot aAlP + y \cdot aGaP + (1 - x - y) \cdot aInP$

Lattice Matching to GaAs: $ylm(x) := \frac{aGaAs - x \cdot aAlP - (1 - x) \cdot aInP}{aGaP - aInP}$

$(Al_xGa_yIn_{1-x-y}P)$

$aQlm(x) := x \cdot aAlP + ylm(x) \cdot aGaP + (1 - x - ylm(x)) \cdot aInP$

$xalinp := \frac{aGaAs - aInP}{aAlP - aInP}$ $ygainp := \frac{aGaAs - aInP}{aGaP - aInP}$ $xgainp := 0$

Check: $xalinp = 0.5161$ $ygainp = 0.51548$ $aQ(0, ygainp) = 5.6532$

$ylm(0) = 0.51548$ $aQlm(0) = 5.6532$

=====> $\mu nQ(x) := x \cdot \mu nAlP + ylm(x) \cdot \mu nGaP + (1 - x - ylm(x)) \cdot \mu nInP$

$\mu pQ(x) := x \cdot \mu pAlP + ylm(x) \cdot \mu pGaP + (1 - x - ylm(x)) \cdot \mu pInP$

Refractive Index: [From Tanaka, et al, *J. Appl. Phys.* **59**, 985 (1986); the second term in nQ(x) is a correction factor added by this author (see Ch V)]

$EdQ(xQ) := 28.07 - 3.373 \cdot xQ\ eV$ $EoQ(xQ) := 3.39 - 1.216 \cdot xQ\ eV$

$nQ(x) := \sqrt{1 - \frac{EoQ(x) \cdot EdQ(x)}{EoQ(x)^2 - Eo(\lambda o)^2}} + 0.18 - 0.03 \cdot \frac{x}{0.516}$

$nalinp := nQ(xalinp)$ $nalinp = 3.103$

$ngainp := nQ(xgainp)$ $ngainp = 3.442$

DBR quarter wavelength thickness:

$$dQ(x) := \frac{\lambda o}{4 \cdot nQ(x)} \qquad ====> \qquad dQ(xalinp) = 52.373 \text{ nm}$$

$dQ(xgainp) = 47.213$ nm

$dQ(0.1) = 48.391$ nm

$dQ(0.14) = 48.835$ nm

AlGaAs

Mobilities: $\mu nGaAs := 8500$ cm^2/V^*s $\mu nAlAs := 1000$ cm^2/V^*s

$\mu pGaAs := 400$ $\mu pAlAs := 180$

Note: The calculations below all use high Al content, and since a linear interpolation between the direct GaAs and indirect AlAs is meaningless for mobility in this region, it is assumed that the mobility does not change much for xT>0.8; thus the AlAs values are used for large xT.

Refractive Index: [From: S. Adachi, *J. Appl. Phys.* **58**, R1 (1985)]

$$EoA(x) := 1.425 + 1.155 \cdot x + 0.37 \cdot x^2 \qquad Eo\Delta o(x) := 1.765 + 1.115 \cdot x + 0.37 \cdot x^2$$

$$chi(x) := \frac{Eo \cdot \lambda o}{EoA(x)} \qquad chiso(x) := \frac{Eo \cdot \lambda o}{Eo\Delta o(x)}$$

$$Ao(x) := 6.3 + 19 \cdot x \qquad Bo(x) := 9.4 - 10.2 \cdot x$$

$$fchi(chi) := \frac{2 - (1 + chi)^{0.5} - (1 - chi)^{0.5}}{chi^2}$$

$$\varepsilon 1(x) := Ao(x) \cdot \left[fchi(chi(x)) + 0.5 \cdot \frac{EoA(x)}{Eo\Delta o(x)}^{1.5} \cdot fchi(chiso(x)) \right] + Bo(x)$$

$$nAs(x) := \sqrt{\varepsilon 1(x)}$$

DBR quarter wavelength thickness:

$$dAs(x) := \frac{\lambda o}{4 \cdot nAs(x)}$$

$xalas := 1$

$nalas := nAs(xalas)$

$nalas = 3.115$

$dalas := dAs(xalas)$

$dalas = 52.173$ nm

For xT = 0.9

$nAs(0.9) = 3.185$

$dAs(0.9) = 51.016$ nm

N-Type DBR Material Systems:

AlAs/AlGaInP xQ = 0.10 n-type: ΔEc = 20 meV 40.5 DBR periods

m := 40 xQ := 0.1

μnAlAs = 1000 cm²/V*s μnQ(xQ) = 2070.3 cm²/V*s

ρTn := ρ μnAlAs ·1000 ρQn := ρ μnQ(xQ) ·1000

ρTn = 3.121 mΩ*cm ρQn = 1.507 mΩ*cm

dalas = 52.173 nm dQ(xQ) = 48.391 nm

RcTn := Rc dalas, μnAlAs RcQn := Rc dQ(xQ), μnQ(xQ)

$RcTn = 1.628 \cdot 10^{-8}$ Ω*cm² $RcQn = 7.294 \cdot 10^{-9}$ Ω*cm²

=====> RcΔEcL := m·(RcTn + RcQn) + RcQn

$RcΔEcL = 9.503 \cdot 10^{-7}$ Ω*cm²

AlInP/AlGaInP xQ = 0.10 n-type: ΔEc = 208 meV 40.5 DBR periods
xT = 0.516 (large offset control sample)

(Note: xT is used in this case for the end-point ternary AlInP of the quaternary AlGaInP in order to differentiate it from the xQ=0.10 AlGaInP layer in the calculations below.)

xT := xalinp xT = 0.516 same as above:

μnQ(xT) = 1976.9 cm²/V*s m := 40

ρTnH := ρ μnQ(xT) ·1000 xQ = 0.1

ρTnH = 1.579 mΩ*cm ρQn = 1.507 mΩ*cm

dQ(xT) = 52.373 nm dQ(xQ) = 48.391 nm

RcTnH := Rc dQ(xT), μnQ(xT)

$RcTnH = 8.268 \cdot 10^{-9}$ Ω*cm² $RcQn = 7.294 \cdot 10^{-9}$ Ω*cm²

=====> RcΔEcH := m·(RcQn + RcTnH) + RcQn

$RcΔEcH = 6.298 \cdot 10^{-7}$ Ω*cm²

P-Type DBR Material Systems:

AlGaAs/AlGaInP xT = 0.90 xQ = 0.14 p-type: ΔEv = 100 meV (low offset) 40.5 DBR periods

$xT := 0.9$ $xQ := 0.14$ $m := 40$

$\mu pAlAs = 180$ $cm^2/V*s$ $\mu pQ(xQ) = 347$ $cm^2/V*s$

$\rho TpL := \rho\ \mu pAlAs \cdot 1000$ $\rho Qp := \rho\ \mu pQ(xQ) \cdot 1000$

$\rho TpL = 17.337$ $m\Omega*cm$ $\rho Qp = 8.994$ $m\Omega*cm$

$dAs(xT) = 51.016$ nm $dQ(xQ) = 48.835$ nm

$RcTpL := Rc\ dAs(xT), \mu pAlAs$ $RcQp := Rc\ dQ(xQ), \mu pQ(xQ)$

$RcTpL = 8.845 \cdot 10^{-8}$ $\Omega*cm^2$ $RcQp = 4.392 \cdot 10^{-8}$ $\Omega*cm^2$

=====> $RcΔEvL := m \cdot (RcTpL + RcQp) + RcQp$

$RcΔEvL = 5.339 \cdot 10^{-6}$ $\Omega*cm^2$

==========

AlInP/AlGaInP xQ = 0.14 xT = 0.516 p-type: ΔEc = 200 meV (large offset control sample) 40.5 DBR periods

(Note: xT is again used for the ternary AlInP)

$xT := xalinp$ $xT = 0.516$ same as above:

$\mu pQ(xT) = 290.3$ $cm^2/V*s$ $m := 40$

$\rho TpH := \rho\ \mu pQ(xT) \cdot 1000$ $xQ = 0.14$

$\rho TpH = 10.748$ $m\Omega*cm$ $\rho Qp = 8.994$ $m\Omega*cm$

$dQ(xT) = 52.373$ nm $dQ(xQ) = 48.835$ nm

$RcTpH := Rc\ dQ(xT), \mu pQ(xT)$

$RcTpH = 5.629 \cdot 10^{-8}$ $\Omega*cm^2$ $RcQp = 4.392 \cdot 10^{-8}$ $\Omega*cm^2$

=====> $RcΔEvH := m \cdot (RcQp + RcTpH) + RcQp$

$RcΔEvH = 4.053 \cdot 10^{-6}$ $\Omega*cm^2$

==========

C.2 Barrier Resistance Calculations

This section calculates the specific contact resistance at the heterojunctions of the DBRs using thermionic-field emission theory (following Robinson, 1983).

Physical Constants: $q := 1.6022 \cdot 10^{-19}$ C $\varepsilon_o := 8.8542 \cdot 10^{-12}$ F/m $\lambda o := 650$ nm

$k := 1.3807 \cdot 10^{-23}$ J/K $m_o := 9.1094 \cdot 10^{-31}$ kg $E(\lambda) := \frac{1240}{\lambda}$ eV

$h := 6.6261 \cdot 10^{-34}$ J*s $T := 300$ K

$\frac{k \cdot T}{q} = 0.02585$ eV

Dielectric Constants:

$Al_xGa_yIn_{1-x-y}P$ [From: H. Tanaka, et al (1986)]

Lattice matched to GaAs: 1-x-y = 0.49
y = 0.51 - x
0 < x < 0.51

$EoQ(xQ) := 3.39 + 1.216 \cdot xQ$ $EdQ(xQ) := 28.07 + 3.373 \cdot xQ$

$$nQ(xQ) := \sqrt{1 + \frac{EoQ(xQ) \cdot EdQ(xQ)}{EoQ(xQ)^2 - E\ \lambda o^2}} - \left[0.18 - 0.03 \cdot \frac{xQ}{0.516}\right]$$

$\varepsilon Q(xQ) := nQ(xQ)^2$ $\varepsilon Q(0.1) = 11.276$

$Al_xGa_{1-x}As$ {From: S. Adachi (1985)}

$xT := 1$ (aluminum mole fraction)

$EoA(x) := 1.425 + 1.155 \cdot x + 0.37 \cdot x^2$ $Eo\Delta o(x) := 1.765 + 1.115 \cdot x + 0.37 \cdot x^2$

$chi(x, \lambda) := \frac{E(\lambda)}{EoA(x)}$ $chiso(x, \lambda) := \frac{E(\lambda)}{Eo\Delta o(x)}$

$Ao(x) := 6.3 + 19 \cdot x$ $Bo(x) := 9.4 - 10.2 \cdot x$

$$fchi(chi) := \frac{2 - (1 + chi)^{0.5} - (1 - chi)^{0.5}}{chi^2}$$

$$\varepsilon As(x, \lambda) := Ao(x) \cdot \left[fchi(chi(x, \lambda)) + 0.5 \cdot \frac{EoA(x)}{Eo\Delta o(x)}^{1.5} \cdot fchi(chiso(x, \lambda))\right] + Bo(x)$$

$\varepsilon As(xT, \lambda o) = 9.701$

Semiconductor Lattice Constants (Å):

$aInAs := 6.05838$ $aGaAs := 5.65315$

$aInP := 5.86875$ $aAlP := 5.45100$

$aAlAs := 5.66220$ $aGaP := 5.45050$

Quaternary Composition:

a(Q) = x(a1) + y(a2) + (1-x-y)a3

Lattice matching: a(Q) = a(GaAs)

$$ylm(xQ) := \frac{aGaAs - xQ \cdot aAlP - (1 - xQ) \cdot aInP}{aGaP - aInP}$$

$zlm(xQ) := 1 - xQ - ylm(xQ)$

$Q(x, y, A, B, C) := x \cdot C + y \cdot B + (1 - x - y) \cdot A$

$aQlm(xQ) := Q(xQ, ylm(xQ), aInP, aGaP, aAlP)$

$aQlm(0.1) = 5.65315$ <== ok

Ternary Composition: $aT(xT) := aGaAs + xT \cdot (aAlAs - aGaAs)$

Effective masses:

$Al_xGa_yIn_{1-x-y}P$

$m_{eInP} := 0.077$ $m_{eGaP} := 0.14$ $m_{eAlP} := 0.33$

$m_{lhInP} := 0.12$ $m_{lhGaP} := 0.14$ $m_{lhAlP} := 0.211$

$m_{hhInP} := 0.56$ $m_{hhGaP} := 0.4$ $m_{hhAlP} := 0.2$

$m_{soInP} := 0.17$ $m_{soGaP} := 0.24$ $m_{soAlP} := 0.26$

$m_{eQ}(xQ) := Q(xQ, ylm(xQ), m_{eInP}, m_{eGaP}, m_{eAlP})$

$m_{lhQ}(xQ) := Q(xQ, ylm(xQ), m_{lhInP}, m_{lhGaP}, m_{lhAlP})$

$m_{hhQ}(xQ) := Q(xQ, ylm(xQ), m_{hhInP}, m_{hhGaP}, m_{hhAlP})$

$m_{soQ}(xQ) := Q(xQ, ylm(xQ), m_{soInP}, m_{soGaP}, m_{soAlP})$

$$m_{pdosQ}(x) := \left(m_{lhQ}(x)^{1.5} + m_{hhQ}(x)^{1.5}\right)^{\frac{2}{3}}$$

For X-band AlInP: $mn_{dos} := 0.4665$

$mn_{cond} := 0.3194$

$Al_xGa_{1-x}As$ [From: S. Adachi (1985)]

Conductivity effective mass

$m_{eT\Gamma}(x) := 0.067 + 0.083 \cdot x$

$m_{eTX}(x) := 0.32 - 0.06 \cdot x$

Density of states electron mass

$m_{nT\Gamma}(x) := 0.067 + 0.083 \cdot x$

$m_{nTX}(x) := 0.85 - 0.14 \cdot x$

Valence band effective mass

$m_{lhT}(x) := 0.087 + 0.063 \cdot x$

$m_{hhT}(x) := 0.62 + 0.14 \cdot x$

$m_{soT}(x) := 0.15 + 0.09 \cdot x$

$m_{pdosT}(x) := \left(m_{lhT}(x)^{1.5} + m_{hhT}(x)^{1.5} \right)^{\frac{2}{3}}$

Fermi Level Calculations:

Density of states: $Nc(me) := 2 \cdot \left(\frac{2 \cdot \pi \cdot me \cdot m_o \cdot k \cdot T}{h^2} \right)^{1.5} \cdot \frac{1}{10^6}$ $Nv(mp) := 2 \cdot \left(\frac{2 \cdot \pi \cdot mp \cdot m_o \cdot k \cdot T}{h^2} \right)^{1.5} \cdot \frac{1}{10^6}$

Fermi-Dirac: $Fhalf(\eta) := \frac{2}{\sqrt{\pi}} \cdot \int_0^{100} \frac{\sqrt{x}}{1 + \exp(x - \eta)} dx$ $Nc(0.71) = 1.501 \cdot 10^{19}$ cm^{-3}

Concentrations: $n(\xi, me) := Nc(me) \cdot Fhalf\left(\frac{q \cdot \xi}{k \cdot T}\right)$ $p(\xi, me) := Nv(me) \cdot Fhalf\left(\frac{q \cdot \xi}{k \cdot T}\right)$

Note: ξ is relative to the conduction ($E_F - E_c$) or valence ($E_v - E_F$) bands

Test: $\xi\_test := -0.05$ eV $n(\xi\_test, 0.71) = 2.066 \cdot 10^{18}$ cm^{-3}

Constants Used in Resistance Calculations:

Richardson constant (A*) ===> units: $A/(m^2 \cdot K^2)$

$A_R(m_{star}) := \frac{4 \cdot \pi \cdot q \cdot m_{star} \cdot m_o \cdot k^2}{h^3}$ $A_R(1) \cdot \frac{1}{100^2} = 120.182$ $A/(cm^2 \cdot K^2)$

==> check ok

$E_{00}(Nd, m_{star}, \varepsilon_s) := \frac{h \cdot q}{4 \cdot \pi} \cdot \sqrt{\frac{Nd \cdot 100^3}{m_{star} \cdot m_o \cdot \varepsilon_s \cdot \varepsilon_o}}$ J (note: Nd in cm^{-3})

$Cl(\phi_B, V, \xi, Nd, m_{star}, \varepsilon_s) := 2 \cdot E_{00}(Nd, m_{star}, \varepsilon_s)^{-1} \cdot \ln\left(-4 \cdot \frac{\phi_B - V}{\xi}\right)$ 1/J

Note: here, ξ is defined as $E_c - E_F$; opposite to Fermi-Dirac

Expressions for Specific Contact Resistance:

$R_c = (dV/dJ)_{V=0}$ (units: $\Omega*cm^2$)

$V := 0$

1. For Field emission ($E_{00} >> kT$)

$$termlf(A, Cl, Eoo, \phi) := \frac{A \cdot T \cdot \pi \cdot q}{k \cdot \sin(\pi \cdot Cl \cdot k \cdot T)} \cdot \exp\left(\frac{-q \cdot \phi}{Eoo}\right)$$

$$term2f(A, Cl, Eoo, \xi, \phi) := \frac{A \cdot q}{Cl \cdot k^2} \cdot \exp\left[-\frac{q \cdot \phi}{Eoo} + Cl \cdot q \cdot \xi\right]$$

$$Rc_f(A, Cl, Eoo, \xi, \phi) := termlf(A, Cl, Eoo, \phi) - term2f(A, Cl, Eoo, \xi, \phi)^{-1}$$

2. For Thermionic-Field emission ($E_{00} \sim kT$)

$$termltf(A, Eoo, \xi, \phi) := \frac{k^2 \cdot \cosh\left(\frac{Eoo}{k \cdot T}\right)}{q \cdot A \cdot \sqrt{\pi \cdot (q \cdot \phi - q \cdot \xi)} \cdot Eoo} \cdot \sqrt{\coth\left(\frac{Eoo}{k \cdot T}\right)}$$

$$term2tf(Eoo, \xi, \phi) := \exp\left[\frac{q \cdot (\phi - \xi)}{Eoo \cdot \coth\left(\frac{Eoo}{k \cdot T}\right)} + \frac{q \cdot \xi}{k \cdot T}\right]$$

$$Rc_{tf}(A, Eoo, \xi, \phi) := termltf(A, Eoo, \xi, \phi) \cdot term2tf(Eoo, \xi, \phi)$$

3. For Thermionic emission ($E_{00} << kT$)

$$Rc_t(A, \phi, T) := \frac{k}{q \cdot A \cdot T} \cdot \exp\left(\frac{q \cdot \phi}{k \cdot T}\right)$$

C.2.1 DBR Barrier Resistances: N-Type AlAs/AlGaInP (xQ = 0.1)

$\Delta Ec := 0.01$ eV (intrinsic band lineup)

$N_D := 2 \cdot 10^{18}$ cm^{-3}

AlAs: $xT := 1$

$\varepsilon_{sT} := \varepsilon As(xT, \lambda o)$

$\varepsilon_{sT} = 9.701$

$m_{ncT} := m_{eTX}(xT)$

$m_{ncT} = 0.26$

$m_{ndT} := m_{nTX}(xT)$

$m_{ndT} = 0.71$

$A_T := \frac{A_R \, m_{ncT}}{100^2}$

$A_T = 31.247$ $A/(cm^2 * K^2)$

$EooT := E_{00}(N_D, m_{ncT}, \varepsilon_{sT})$

$EooT = 2.649 \cdot 10^{-21}$ J

Guess: $\xi := -0.1$

Given

$n(\xi, m_{ndT}) - N_D = 0$

$EfnT := minerr(\xi)$

$EfnT = -0.051$ eV

Note: Efn = Ef - Ec

$CIT := CI(\Delta Ec, V, -EfnT, N_D, m_{ncT}, \varepsilon_{sT})$

$CIT = -4.54 \cdot 10^{19} + 5.93 \cdot 10^{20} i$ 1/J

AlGaInQ: $xQ := 0.1$ $ylm(xQ) = 0.416$

$\varepsilon_{sQ} := \varepsilon Q(xQ)$

$\varepsilon_{sQ} = 11.276$

$m_{nQ} := m_{eQ}(xQ)$

$m_{nQ} = 0.12848$

$A_Q := \frac{A_R \, m_{nQ}}{100^2}$

$A_Q = 15.441$ $A/(cm^2 * K^2)$

$EooQ := E_{00}(N_D, m_{nQ}, \varepsilon_{sQ})$

$EooQ = 3.495 \cdot 10^{-21}$ J

Note: $k T = 4.142 \cdot 10^{-21}$

Given

$n(\xi, m_{nQ}) - N_D = 0$

$EfnQ := minerr(\xi)$

$EfnQ = 0.03$ eV

$CIQ := CI(\Delta Ec, V, -EfnQ, N_D, m_{nQ}, \varepsilon_{sQ})$

$CIQ = 4.29 \cdot 10^{19}$ 1/J

DBR Barrier Resistances: N-type AlAs/AlGaInP (xQ = 0.1)

From SimWindows (b_Q_AlAs.dev), the n-n junction of AlAs/AlGaInP (xQ=0.1) does not actually have a "triangular" barrier and well due to depletion and accumulation, respectively. Instead, it is a step barrier from the conduction band in the AlGaInP to the conduction band in the AlAs, which from the previous page is 51 meV (E_{fnT}). The electron transport across the junction is thus governed by simple thermionic emission, the expression for which is valid regardless of the direction of current flow.

For the junction between the bottom quaternary layer of the DBR and the GaAs substrate, there is a triangular barrier in the quaternary material. The theoretical barrier height ϕ_B in the Schottky barrier equations is from the bottom of the semiconductor conduction band at the interface (i.e. the top of the triangle) to the energy level at which the electrons move in the metal (i.e. the Fermi level). For the AlGaInP/GaAs heterojunction, ϕ_B is from the peak of the conduction band triangle in the quaternary down to the degenerate Fermi level in the GaAs. From SimWindows, ϕ_B=130 meV. Electron transport for this type of junction can be modeled using thermionic-field emission, and the expression for Rc is valid regardless of the direction of current flow.

The calculations assume an m.5-period Q/T mirror on a GaAs substrate, so that the structure has 2m Q/T junctions and one Q/sub junction. Thus for this case the total contribution to the specific contact resistance due to the barriers in the stack is $2m*R_{cQT} + R_{cQs}$.

Thermionic emission: Q /T Interfaces

$$RcQT := Rc_t(A_Q, -EfnT, T)$$

$$RcQT = 1.33124 \cdot 10^{-7} \quad \Omega^*cm^2$$

Thermionic-field emission: Q/GaAs interface

$$\phi B := 0.130 \quad eV$$

$$RcQs := Rc_{tf}(A_Q, EooQ, -EfnQ, \phi B)$$

$$RcQs = 3.725 \cdot 10^{-7} \quad \Omega^*cm^2$$

For an m-period DBR: $Rctotal(m) := 2 \cdot m \cdot RcQT + RcQs$

$$Rctotal(1) = 6.3872 \cdot 10^{-7} \quad \Omega^*cm^2$$

$$Rctotal(40) = 1.1022 \cdot 10^{-5} \quad \Omega^*cm^2$$

==========

C.2.2 DBR Barrier Resistances: N-Type AlInP/AlGaInP (xQ = 0.52/0.1)

$\Delta Ec := 0.21$ eV (intrinsic band lineup from SimWindows)

$N_D := 2 \cdot 10^{18}$ cm^{-3}

$x := 0.5$

AlInP: $xT := root(ylm(x), x)$

$xT = 0.516$

$\varepsilon_{sT} := \varepsilon Q(xT)$

$\varepsilon_{sT} = 9.627$

$m_{ncT} := mn_{cond}$ $m_{ncT} = 0.319$

$m_{ndT} := mn_{dos}$ $m_{ndT} = 0.467$

$A_T := \frac{A_R \, m_{ncT}}{100^2}$

$A_T = 38.386$ $A/(cm^2 \cdot K^2)$

$EooT := E_{00}(N_D, m_{ncT}, \varepsilon_{sT})$

$EooT = 2.399 \cdot 10^{-21}$ J

Guess: $\xi := -0.1$

Given

$n(\xi, m_{ndT}) - N_D = 0$

$EfnT := minerr(\xi)$

$EfnT = -0.034$ eV

(not degenerate)

$C1T := C1(\Delta Ec, V, -EfnT, N_D, m_{ncT}, \varepsilon_{sT})$

$C1T = 6.713 \cdot 10^{20} + 6.547 \cdot 10^{20} i$ 1/J

AlGaInP: $xQ := 0.1$ $ylm(xQ) = 0.416$

$\varepsilon_{sQ} := \varepsilon Q(xQ)$

$\varepsilon_{sQ} = 11.276$

$m_{nQ} := m_{eQ}(xQ)$

$m_{nQ} = 0.12848$

$A_Q := \frac{A_R \, m_{nQ}}{100^2}$

$A_Q = 15.441$ $A/(cm^2 \cdot K^2)$

$EooQ := E_{00}(N_D, m_{nQ}, \varepsilon_{sQ})$

$EooQ = 3.495 \cdot 10^{-21}$ J

Note: $k \cdot T = 4.142 \cdot 10^{-21}$

Note: Efn = Ef - Ec

Given

$n(\xi, m_{nQ}) - N_D = 0$

$EfnQ := minerr(\xi)$

$EfnQ = 0.03$ eV (degenerate)

$C1Q := C1(\Delta Ec, V, -EfnQ, N_D, m_{nQ}, \varepsilon_{sQ})$

$C1Q = 4.785 \cdot 10^{20}$ 1/J

DBR Barrier Resistances: N-Type AlInP/AlGaInP (xQ = 0.52/0.1)

From SimWindows (bQ_AlInP.dev), the n-n junction of AlInP/AlGaInP (xQ=0.52/0.1) has a "triangular" barrier in the ternary and a well in the quaternary due to depletion and accumulation, respectively. Also, at the junction, the Fermi level is at a lower energy than the conduction band in both the ternary and the quaternary. The junction between the quaternary and the GaAs substrate also contains a triangular barrier in the quaternary, and on the degenerate GaAs side of the barrier the Fermi level is above the bulk conduction band.

For electron transport across the quaternary/ternary junction (RcTQ), the band lineup is exactly like a metal-semiconductor Schottky barrier, with the quaternary taking the place of the metal. Thus electron transport across the junction is governed by thermionic-field emission, and the specific contact resistance (determined at zero applied bias) is independent of any assumed direction of current flow. From SimWindows, the barrier height, ϕ_B, from the peak of the conduction band in the ternary to the Fermi level in the well of the quaternary is 151 meV.

Electron transport from the quaternary to the GaAs substrate can also be modeled using the thermionic field emission equations. This is exactly the same situation as found in the previous n-DBR, and from SimWindows the appropriate barrier height is 130 meV.

Assuming an m.5-period Q/T DBR on a GaAs substrate, there are 2*m T/Q junctions and one Q/sub junction. Thus the total specific contact resistance due to the barriers in the stack is $2m*R_{cTQ} + R_{cQs}$.

Thermionic-field emission:

T/Q interface:

$\phi B := 0.151$ eV

$RcTQ := Rc_{tf}(A_T, EooT, -EfnT, \phi B)$

$RcTQ = 9.282 \cdot 10^{-7}$ $\Omega*cm^2$

Q/GaAs interface:

$\phi Bts := 0.130$ eV

$RcQs := Rc_{tf}(A_Q, EooQ, -EfnQ, \phi Bts)$

$RcQs = 3.725 \cdot 10^{-7}$ $\Omega*cm^2$

Total DBR barrier contact resistance: (m = # of periods)

$Rtotal(m) := 2 \cdot m \cdot RcTQ + RcQs$

$Rtotal(1) = 2.229 \cdot 10^{-6}$ $\Omega*cm^2$

$Rtotal(40) = 7.4629 \cdot 10^{-5}$ $\Omega*cm^2$

==========

C.2.3 DBR Barrier Resistance: P-Type AlGaAs/AlGaInP (xT = 0.9/xQ = 0.14)

$N_A := 2 \cdot 10^{18}$ cm^{-3}

AlGaAs: $xT := 0.9$ AlGaInP: $xQ := 0.14$ $ylm(xQ) = 0.376$

$\varepsilon_{sT} := \varepsilon As(xT, \lambda o)$ $\varepsilon_{sQ} := \varepsilon Q(xQ)$

$\varepsilon_{sT} = 10.146$ $\varepsilon_{sQ} = 11.073$

$m_{pcT} := m_{lhT}(xT)$ $m_{pcT} = 0.144$ $m_{pdQ} := m_{pdosQ}(xQ)$ $m_{pdQ} = 0.5003$

$m_{pdT} := m_{pdosT}(xT)$ $m_{pdT} = 0.7875$ $m_{pcQ} := m_{lhQ}(xQ)$ $m_{pcQ} = 0.14025$

$A_T := \frac{A_R \, m_{pcT}}{100^2}$ $A_Q := \frac{A_R \, m_{pcQ}}{100^2}$

$A_T = 17.27$ $A/(cm^2 \cdot K^2)$ $A_Q = 16.856$ $A/(cm^2 \cdot K^2)$

$EooT := E_{00}(N_A, m_{pcT}, \varepsilon_{sT})$ $EooQ := E_{00}(N_A, m_{pcQ}, \varepsilon_{sQ})$

$EooT = 3.484 \cdot 10^{-21}$ J $EooQ = 3.376 \cdot 10^{-21}$ J

Note: $k \cdot T = 4.142 \cdot 10^{-21}$ ==> for both T & Q we have Eoo ~ kT and we should use thermionic-field emission

Guess: $\xi := -0.1$

Given

$p(\xi, m_{pdT}) - N_A = 0$

$EfpT := minerr(\xi)$

$EfpT = -0.055$ eV

(not degenerate)

Note: Efp = Ev - Ef
(Ef above Ev for non-degenerate)

Given

$p(\xi, m_{pdQ}) - N_A = 0$

$EfpQ := minerr(\xi)$

$EfpQ = -0.036$ eV (non degenerate)

$CIT := CI(\Delta Ec, V, -EfpT, N_A, m_{pcT}, \varepsilon_{sT})$ $CIQ := CI(\Delta Ec, V, -EfpQ, N_A, m_{pcQ}, \varepsilon_{sQ})$

$CIT = 3.91 \cdot 10^{20} + 4.508 \cdot 10^{20} i$ 1/J $CIQ = 4.646 \cdot 10^{20} + 4.653 \cdot 10^{20} i$ 1/J

DBR Barrier Resistances: P-Type AlGaAs/AlGaInP (xT = 0.9/xQ = 0.14)

From SimWindows (b_Q_AlAs.dev) the p-p heterojunction of AlGaAs (x=0.9)/AlGaInP (x=0.14) has a "triangular" barrier in the ternary and a well in the quaternary due to depletion and accumulation, respectively. Also, the Fermi level is at a higher energy than the valence band (i.e. in the band gap) in each material, including in the well. For the junction between the DBR and the GaAs substrate there is a triangular barrier in the quaternary and a well in the GaAs, and the Fermi level is above the bulk valence band (i.e. in the band gap) on both sides of the junction.

For hole transport across the ternary/quaternary interface (RcTQ), the band lineup is the same as that of the Schottky barrier theory. Thus the transport, and the specific contact resistance, should be governed by thermionic field emission. From SimWindows the height of the barrier, ϕ_B, is 105 meV.

Hole transport from the quaternary to the GaAs substrate can also be modeled using the thermionic field emission equations. This is exactly the same situation as found in the previous n-DBRs, except in this case the appropriate barrier height from SimWindows is ϕ_B=321 meV.

Assuming an m.5-period Q/T DBR mirror on a GaAs substrate, there are 2m T/Q junctions and one Q/sub junction. The total contribution to the specific contact resistance from the barriers in the stack is 2m*RcTQ + RcQsub.

Thermionic-field emission

T/Q interface: $\phi B := 0.105$ eV

$RcTQ := Rc_{tf}(A_T, EooT, -EfpT, \phi B)$

$RcTQ = 4.9733 \cdot 10^{-7}$ Ω^*cm^2

Q/GaAs interface: $\phi Bts := 0.321$ eV

$RcQs := Rc_{tf}(A_Q, EooQ, -EfpQ, \phi Bts)$

$RcQs = 1.9016 \cdot 10^{-4}$ Ω^*cm^2

Total DBR barrier contact resistance: (m = # of periods)

$Rtotal(m) := 2 \cdot m \cdot RcTQ + RcQs$

$Rtotal(1) = 1.9116 \cdot 10^{-4}$ Ω^*cm^2

$Rtotal(40) = 2.2995 \cdot 10^{-4}$ Ω^*cm^2

Note: The above value is dominated by the Q/GaAs interface

For just the DBR interfaces: $2 \cdot m \cdot RcTQ = 3.979 \cdot 10^{-5}$ Ω^*cm^2

C.2.4 DBR Barrier Resistances: P-Type AlInP/AlGaInP (xQ = 0.52/0.14)

$N_A := 2 \cdot 10^{18}\ cm^{-3}$

$x1 := 0.5$

AlInP: $xT := root(ylm(x1), x1)$ AlGaInP: $xQ := 0.14$

$xT = 0.516098$ $ylm(xQ) = 0.376$

$\varepsilon_{sT} := \varepsilon Q(xT)$ $\varepsilon_{sQ} := \varepsilon Q(xQ)$

$\varepsilon_{sT} = 9.627$ $\varepsilon_{sQ} = 11.073$

$m_{pcT} := m_{lhQ}(xT)$ $m_{pcT} = 0.167$ $m_{pdQ} := m_{pdosQ}(xQ)$ $m_{pdQ} = 0.5003$

$m_{pdT} := m_{pdosQ}(xT)$ $m_{pdT} = 0.4453$ $m_{pcQ} := m_{lhQ}(xQ)$ $m_{pcQ} = 0.14025$

$A_T := \frac{A_R\ m_{pcT}}{100^2}$ $A_Q := \frac{A_R\ m_{pcQ}}{100^2}$

$A_T = 20.066$ $A/(cm^2 \cdot K^2)$ $A_Q = 16.856$ $A/(cm^2 \cdot K^2)$

$EooT := E_{00}(N_A, m_{pcT}, \varepsilon_{sT})$ $EooQ := E_{00}(N_A, m_{pcQ}, \varepsilon_{sQ})$

$EooT = 3.318 \cdot 10^{-21}$ J $EooQ = 3.376 \cdot 10^{-21}$ J

Note: $k \cdot T = 4.142 \cdot 10^{-21}$ ==> for both T & Q we have Eoo ~ kT and we should use thermionic-field emission

Guess: $\xi := -0.1$

Given Note: Efp = Ev - Ef

$p(\xi, m_{pdT}) - N_A = 0$

$EfpT := minerr(\xi)$

$EfpT = -0.032$ eV

(not degenerate)

Given

$p(\xi, m_{pdQ}) - N_A = 0$

$EfpQ := minerr(\xi)$

$EfpQ = -0.036$ eV (non degenerate)

$C1T := C1(\Delta Ec, V, -EfpT, N_A, m_{pcT}, \varepsilon_{sT})$ $C1Q := C1(\Delta Ec, V, -EfpQ, N_A, m_{pcQ}, \varepsilon_{sQ})$

$C1T = 4.945 \cdot 10^{20} + 4.734 \cdot 10^{20} i$ 1/J $C1Q = 4.646 \cdot 10^{20} + 4.653 \cdot 10^{20} i$ 1/J

DBR Barrier Resistances: P-Type AlInP/AlGaInP (xQ = 0.52/0.14)

From SimWindows (bQ_AlInP.dev) the p-p heterojunction of AlInP/AlGaInP (x=0.52/0.14) has a "triangular" barrier in the ternary and a well in the quaternary due to depletion and accumulation, respectively. Also, the Fermi level is above the bulk valence band (in the band gap) in each material, however the Fermi level crosses the valence band the well. For the junction between the DBR and the GaAs substrate there is a triangular barrier in the quaternary and a well in the GaAs. In this case the Fermi level is also at a higher energy than the bulk valence band (i.e. in the band gap) on both sides of the junction and it also crosses the valence band in the well.

For hole transport across the ternary/quaternary interface (RcTQ), the band lineup is the same as that of the Schottky barrier theory. Thus the transport is governed by thermionic field emission. From SimWindows the height of the barrier, ϕ_B, is 179 meV.

Hole transport from the quaternary to the GaAs substrate can also be modeled using the thermionic field emission equations. This is exactly the same situation as found in the previous p-DBR, except in this case the appropriate barrier height from SimWindows is 321 meV.

Assuming an m.5-period Q/T DBR mirror on a GaAs substrate, there are 2m T/Q junctions and one Q/sub junction. The total contribution to the specific contact resistance by the barriers in the stack is then 2m*RcTQ + RcQsub.

Thermionic-field emission

T/Q interface: $\phi B := 0.179$ eV

$RcTQ := Rc_{tf}(A_T, EooT, -EfpT, \phi B)$

$RcTQ = 2.3864 \cdot 10^{-6}$ $\Omega \cdot cm^2$

Q/GaAs interface: $\phi Bts := 0.321$ eV

$RcQs := Rc_{tf}(A_Q, EooQ, -EfpQ, \phi Bts)$

$RcQs = 1.9016 \cdot 10^{-4}$ $\Omega \cdot cm^2$

Total DBR barrier contact resistance: (m = # of periods)

$Rtotal(m) := 2 \cdot m \cdot RcTQ + RcQs$

$Rtotal(1) = 1.94935 \cdot 10^{-4}$ $\Omega \cdot cm^2$

$Rtotal(40) = 3.8107 \cdot 10^{-4}$ $\Omega \cdot cm^2$

Note: The above value is dominated by the Q/GaAs interface

For just the DBR interfaces: $2 \cdot m \cdot RcTQ = 1.909 \cdot 10^{-4}$ $\Omega \cdot cm^2$

APPENDIX D

SIMWINDOWS MATERIAL DATA FILE

This appendix contains sections of the SimWindows material data file which describe the AlGaAs and AlGaInP semiconductor alloys used in this work. All of the material parameters used by SimWindows to calculate the band diagrams presented Chapter III are included here.

```
# ************************** GaAs ********************************
# from SimWin default file, 12/6/95.

Material=GaAs
Alloy=Default

BAND_GAP Model=Band_gap terms=1.424,0,0,-5.405e-4,204
ELECTRON_AFFINITY Model=Band_gap terms=4.07,0.0,2.702e-4,204
STATIC_PERMITIVITY Value=13.18
REFRACTIVE_INDEX Model=oscillator_refractive_index
ABSORPTION Segments=2
start_e=0 end_e=g+0.00087 model=exp_band_gap_absorption terms=1.71,0.104
start_e=g+0.00087 end_e=100 model=power_band_gap_absorption terms=3.5e4,0,0,0,0.5
THERMAL_CONDUCTIVITY Model=Thermal_Conduct terms=549.356,1,0,0,-1.25
DERIV_THERMAL_CONDUCT Model=Thermal_Conduct terms=-686.695,1,0,0,-2.25
ELECTRON_MOBILITY Value=8000
HOLE_MOBILITY Value=370
ELECTRON_DOS_MASS Value=0.067
HOLE_DOS_MASS Value=0.62
ELECTRON_COND_MASS Value=0.067
HOLE_COND_MASS Value=.62
ELECTRON_SHR_LIFETIME Value=1e-8
HOLE_SHR_LIFETIME Value=1e-8
```

```
RAD_RECOMB_CONST Value=1.5e-10
ELECTRON_ENERGY_LIFETIME Value=1.e-12
HOLE_ENERGY_LIFETIME Value=1.e-12
QW_RAD_RECOMB_CONST Value=1.54e-4
ELECTRON_COLLISION_FACTOR Value=0.5
HOLE_COLLISION_FACTOR Value=0.5


# ********** AlGaAs **********
# from SimWin default file, 12/6/95.

Alloy=Al

BAND_GAP Segments=2
Start_x=0.00 end_x=0.45 Model=Band_gap terms=1.424,1.247,0,-5.405e-4,204
Start_x=0.45 end_x=1.00 Model=Band_gap terms=1.9,0.125,0.143,-5.405e-4,204

ELECTRON_AFFINITY Segments=2
Start_x=0.0 end_x=0.45 Model=Band_gap terms=4.07,-0.7482,0,2.702e-4,204
Start_x=0.45 end_x=1.0 Model=Band_gap terms=3.594,0.3738,-0.143,2.702e-4,204

STATIC_PERMITIVITY Value=13.18,-3.12
REFRACTIVE_INDEX Model=oscillator_refractive_index
ABSORPTION Segments=2
start_e=0 end_e=g+0.00087 model=exp_band_gap_absorption terms=1,71,0.104
start_e=g+0.00087 end_e=100 model=power_band_gap_absorption terms=3.5e4,0,0,0,0.5
THERMAL_CONDUCTIVITY Model=Thermal_Conduct
 terms=549.356,1,12.7,13.22,-1.25
DERIV_THERMAL_CONDUCT Model=Thermal_Conduct
 terms=-686.695,1,12.7,13.22,-2.25
ELECTRON_MOBILITY Segments=2
Start_x=0.0 end_x=0.45 Value=8000,-22000,10000
Start_x=0.45 end_x=1.0 Value=-255,1160,-720
HOLE_MOBILITY Value=370,-970,740
ELECTRON_DOS_MASS Segments=2
Start_x=0.0 end_x=0.45 Value=0.067,0.083
Start_x=0.45 end_x=1.0 Value=0.85,-0.14
# X band segment added 12/13/96 by JF
HOLE_DOS_MASS Value=0.62,0.14
ELECTRON_COND_MASS Segments=2
Start_x=0.0 end_x=0.45 Value=0.067,0.083
Start_x=0.45 end_x=1.0 Value=0.32,-0.06
HOLE_COND_MASS Value=0.62,0.14
```

```
ELECTRON_SHR_LIFETIME Value=1e-8
HOLE_SHR_LIFETIME Value=1e-8
RAD_RECOMB_CONST Value=1.5e-10
ELECTRON_ENERGY_LIFETIME Value=1.e-12
HOLE_ENERGY_LIFETIME Value=1.e-12
QW_RAD_RECOMB_CONST Value=1.54e-4
ELECTRON_COLLISION_FACTOR Value=0.5
HOLE_COLLISION_FACTOR Value=0.5


#****************** AlGaInP lattice matched to GaAs ********************

Material=GaAs
Alloy=AlGaInP

# The composition x is equal to the Al content Al(x)Ga(y)In(1-x-y)P
# Material originally set up by GYR (Jan 1996)
# Modified by J. Fastenau (Dec 1996)

BAND_GAP Segments=2
Start_x=0.0 end_x=0.37 Model=Band_gap Terms=1.872,0.9313,0.5093,3.63e-4,162
# quadratic fit of Eg(gamma) data calculated using Krijn's formulism and
# used in band offset calculations (JF)
Start_x=0.37 end_x=1 Model=Band_gap Terms=2.3,0.194,0,3.63e-4,162
# X-band data
# data taken from Duggan's talk at CSU; also used in band offset calculations (JF)
# temperature dependance taken to be same as that of InP

ELECTRON_AFFINITY Segments=2
Start_x=0.0 end_x=0.37 value=3.8670,-0.31
#  JF 12/13/96 ==> gives dEc=0 for AlAs/AlGaInP(x=0.12)
#                  gives dEc=0.16 eV for InGaP/InAlP lattice matched to GaAs
#  Start_x=0.0 end_x=1 value=3.788,-0.309 (GYR)
Start_x=0.37 end_x=1 value=3.628,0
# JF 12/17/96 ==> gives dEc=208 meV for InAlP/AlGaInP (x=0.1)

STATIC_PERMITIVITY Segments=1
Start_x=0.0 end_x=1.0 value=12.418,1.499
REFRACTIVE_INDEX Segments=1
Start_x=0.0 end_x=1.0 value=3.30,0.21
#  this should depend on comp and wavelength!  incomplete!!!
ABSORPTION Segments=2
start_e=0 end_e=g+0.00087 model=exp_band_gap_absorption terms=1,71,0.104
```

```
start_e=g+0.00087 end_e=100 model=power_band_gap_absorption terms=3.5e4,0,0,0,0.5
# absorption coefficient similar to GaAs, with change in Eg
THERMAL_CONDUCTIVITY Segments=1
# Start_x=0.0 end_x=1.0 Model=Thermal_conduct terms=1,1.428,60.339,-40.768,0
DERIV_THERMAL_CONDUCT value=0
ELECTRON_MOBILITY Segments=1
Start_x=0.0 end_x=1.0 value=2684,-86.11
HOLE_MOBILITY Segments=1
Start_x=0.0 end_x=0.1 value=142.2,-75

# ** all mass data changed by JF, 12/17/96 **
ELECTRON_DOS_MASS Segments=2
Start_x=0.0 end_x=0.37 value=0.1095,0.1901
# calc. from data in GYR's band_d_2.mcd
Start_x=0.37 end_x=1 value=0.4665
# calculation from data in DST IV & III-V Semiconductor handbook
# X-band is interpolation between AlP & GaP for AlGaP (xAl=0.5)
HOLE_DOS_MASS Segments=1
Start_x=0.0 end_x=1.0 value=0.5219,0.1485
# calc. from data in GYR's band_d_2.mcd
# using mdos = (mlh^1.5 + mhh^1.5)^(2/3)
ELECTRON_COND_MASS Segments=2
Start_x=0.0 end_x=0.37 value=0.1095,0.1901
# calc. from data in GYR's band_d_2.mcd
Start_x=0.37 end_x=1 value=0.3194
# calculation from data in DST IV & III-V Semiconductor handbook
# X-band is interpolation between AlP & GaP for AlGaP (xAl=0.5)
HOLE_COND_MASS Segments=1
Start_x=0.0 end_x=1.0 value=0.1303,0.0710
# calc. from light hole data in GYR's band_d_2.mcd

ELECTRON_SHR_LIFETIME Segments=1
Start_x=0.0 end_x=1.0 value=2e-9,8e-9
HOLE_SHR_LIFETIME Segments=1
Start_x=0.0 end_x=1.0 value=2e-9,8e-9
RAD_RECOMB_CONST Segments=1
Start_x=0.0 end_x=1.0 value=14.91e-9,6.473e-9,-16.67e-9
# following are from GaAs:
ELECTRON_ENERGY_LIFETIME Value=1.e-12
HOLE_ENERGY_LIFETIME Value=1.e-12
QW_RAD_RECOMB_CONST Value=1.54e-4
ELECTRON_COLLISION_FACTOR Value=0.5
HOLE_COLLISION_FACTOR Value=0.5
```